

Novel Electromagnetic Responses in Topological Semimetals: Case Studies of Rare-Earth Monopnictides and RAlX Material Family

Hung-Yu Yang

A dissertation
submitted to the Faculty of
the department of Physics
in partial fulfillment
of the requirements
for the degree of
Doctor of Philosophy

Boston College
Morrissey College of Arts and Sciences
Graduate School

January 2021

Novel Electromagnetic Responses in Topological Semimetals: Case Studies of Rare-Earth Monopnictides and RAlX Material Family

Hung-Yu Yang

Advisor: Fazel Tafti, Ph.D.

Since the idea of topology was realized in real materials, the hunt is on for new candidates of topological semimetals with novel electromagnetic responses. For example, topological states can be highly conductive due to a topological protection, which can be destroyed in a magnetic field and lead to an extremely high magnetoresistance. In Weyl semimetals, a transverse current that would usually require a magnetic field to emerge, can be generated by intrinsic Berry curvature without a magnetic field – the celebrated anomalous Hall effect.

In this dissertation, both phenomena mentioned above are studied in rare-earth monopnictides and RAlX material family (R=rare-earths, X=Ge/Si), respectively. The monopnictides are ideal for the study of extreme magnetoresistance because of their topological transitions and abundant magnetic phases. In LaAs, we untied the connection between topological states and the extreme magnetoresistance, the origin of which is clarified. In HoBi, we found an unusual onset of extreme magnetoresistance controlled by a magnetic phase dome. On the other hand, RAlX material family is a new class of Weyl semimetals breaking both inversion and time-reversal symmetries. In particular, in $\text{PrAlGe}_x\text{Si}_{1-x}$ ($x = 0-1$), we unveiled the first transition from intrinsic to extrinsic anomalous Hall effect in ferromagnetic Weyl semimetals, and the role of topology is discussed. In CeAlSi, we found that the Fermi level can be tuned as close as 1 meV away from the Weyl nodes; moreover, a novel anomalous Hall response appears *only* when the Fermi level is tuned to be near the Weyl nodes. Thus, we established a new transport response solely induced by Weyl nodes.

To S.-C. S and K.-C. Y.

TABLE OF CONTENTS

ACKNOWLEDGEMENTS	vii
LIST OF FIGURES	ix
LIST OF TABLES	xi
LIST OF SYMBOLS	xi
LIST OF ABBREVIATIONS	xiv
CHAPTER	
I. Introduction	1
1.1 Topological Semimetals	2
1.2 Topological States and Extreme Magnetoresistance (XMR)	5
1.3 Anomalous Hall Effect (AHE) in Magnetic Weyl Semimetals	7
II. Methodology	11
2.1 Crystal Growth and Characterization	11
2.1.1 Flux Growth	11
2.1.2 Powder X-ray Diffraction and Rietveld Refinement	14
2.1.3 Energy Dispersive X-ray Spectroscopy	17
2.2 Measurement Techniques	17
2.2.1 Magnetization	19
2.2.2 Electrical Resistivity	20
2.2.3 Squeeze Test for Chiral Anomaly	24
2.3 First-principles Calculations and Extended Applications	29
2.3.1 Handling Correlations	30
2.3.2 Supercell K-space Extremal Area Finder (SKEAF)	32
2.4 Model Analysis	33
2.4.1 Semiclassical Multiband Model	33
2.4.2 Tian-Ye-Jin Scaling of Anomalous Hall Effect	37

2.4.3	Quantum Oscillation (QO)	40
2.4.4	E_F Determination by SKEAF and QO	42
III. Rare-Earth Monopnictides		46
3.1	LaAs: In Search of the Origin of XMR	46
3.1.1	Introduction	47
3.1.2	Methods	48
3.1.3	Magnetoresistance and Hall Effect	49
3.1.4	ARPES Results	52
3.1.5	Band Structure Calculation	54
3.1.6	Quantum Oscillation	55
3.1.7	Discussion	58
3.1.8	Conclusions	59
3.2	HoBi: Interplay between XMR and Magnetism	60
3.2.1	Introduction	61
3.2.2	Methods	62
3.2.3	Magnetization and Metamagnetic Transitions	63
3.2.4	Neutron Scattering	65
3.2.5	Magnetoresistance	68
3.2.6	Quantum Oscillation and DFT Calculations	70
3.2.7	Conclusions	72
IV. RAIX Material Family (R=Rare-Earths, X=Ge/Si)		74
4.1	PrAlGe _x Si _{1-x} : Transition from Intrinsic to Extrinsic AHE	74
4.1.1	Introduction	75
4.1.2	Methods	76
4.1.3	Crystal Structure	79
4.1.4	Magnetic Properties	80
4.1.5	Band Structure	82
4.1.6	Electronic Properties	84
4.1.7	Anomalous Hall Effect	88
4.1.8	Discussion and Conclusions	90
4.2	CeAlSi: Loop Hall Effect Purely Induced by Weyl Nodes	91
4.2.1	Introduction	92
4.2.2	Methods	93
4.2.3	Main Results	95
4.2.4	In-Plane Noncollinear FM Order and Domains	98
4.2.5	Band Structure, Shifted Weyl Nodes, and Intrinsic Anomalous Hall Conductivity	100
4.2.6	Anisotropic Anomalous Hall Effect	104
4.2.7	Outlook	106

APPENDICES	109
A. Supplementary Material for LaAs	110
A.1 XMR and Residual Resistivity Ratio	110
A.2 Multiband Fit	111
A.3 Calculations of Fermi Volumes	113
A.4 ARPES: k_z Dispersion	115
B. Supplementary Material for HoBi	116
B.1 Magnetoresistance with Different Field Directions	116
B.2 Magnetization Data with Different Field Directions	116
B.3 Resistivity Features and the AFM Order	118
B.4 Features in Transport, Magnetization and Neutron Data	118
B.5 Band Structures Calculated by Different U	119
B.6 Effective Mass	122
C. Supplementary Material for PrAlGe_xSi_{1-x}	123
C.1 EDX Results	123
C.2 Rietveld Refinement	123
C.3 Second Harmonic Generation	124
C.4 Curie-Weiss Analysis	127
C.5 Topological Electronic Structure of PrAlGe _{0.5} Si _{0.5}	127
C.6 The Analysis of R_0 and R_S	130
C.7 Quantum Oscillation and Anomalous Hall Conductivity	130
D. Supplementary Material for CeAlSi	132
D.1 Structural Analysis by X-ray and Neutron Diffraction	132
D.2 Second Harmonic Generation	135
D.3 Temperature Dependence of M v.s. H Curves	136
D.4 Neutron Scattering	136
D.5 Scanning SQUID Imaging	138
D.6 Weyl Points	140
D.7 ρ_{xx} Data	142
D.8 EDX Analysis	142
D.9 Quantum Oscillation	143
D.10 The Difference between ρ_{zy}^A and $R_S M$	147
BIBLIOGRAPHY	148

ACKNOWLEDGEMENTS

Throughout my PhD career, my advisor Prof. Fazel Tafti has constantly provided me with full support. As the first PhD student in his lab, I was lucky to receive the most hands-on training from him, and grow up together with Tafti Lab. With him, I have seen how a lab is built up from scratch, how versatile experimental problems are solved, how collaboration is established, and how questions of interest are answered. I appreciate how he gave me a clear research direction when I was a clueless junior graduate student to train my basic skills, and in my senior years gave me sheer freedom to explore new research topics. I will miss the day at late night when I clicked on submit for my first experimental paper in his office. His guidance has led me all these years and I am truly grateful to him.

My thesis committee has advised me to shape my dissertation constructively and given me important feedback. Prof. Ying Ran, who is my first-year advisor, brought me to the field of topological matter, and is always available for fruitful discussions about my research. Prof. Kenneth S. Burch, who can be both kind and sharp, has inspired me with great questions that refined the quality of my research. Prof. Arun Bansil, who is a knowledgeable collaborator and wise mentor, has greatly broadened my horizon through our collaboration in my senior years with his brilliant insight. I am indebted to them.

Collaboration plays an important role in my research; all of my works could not have been possible without valuable contributions by different collaborators with remarkable skills. Some of the key contributors include (in chronological or-

der): Dr. Thomas Nummy and Prof. Daniel S. Dessau (ARPES experiments); Prof. Peter Blaha (first-principles calculations); Dr. David E. Graf (high-field experiments); Dr. Jonathan Gaudet, Prof. Bruce D. Gaulin, and Prof. Collin L. Broholm (neutron scattering experiments); Faranak Bahrami (powder XRD refinement); Baozhu Lu and Prof. Darius H. Torchinsky (second harmonic generation experiments); Prof. Bahadur Singh, Dr. Cheng-Yi Huang, Dr. Wei-Chi Chiu, Prof. Hsin Lin, and Prof. Arun Bansil (first-principles calculations); Bochao Xu and Prof. Ilya Sochnikov (SQUID imaging experiments). Thank you for all the great work.

In Boston College, I have received lots of help and learned from the faculty and staff members, and fellow graduate students. Despite their long to-do lists, the faculty members always welcome me when I need to talk to them, and I either have my questions answered or get new ideas after our conversations. Whenever I have random issues, ranging from package delivery to check deposit, the staff members always get back to me with high efficiency. I also enjoyed a lot the time I spent with my colleagues talking about physics and random things. In particular, the group members of Tafti Lab have brought me lots of fun and taught me many things in a way I did not expect. For example, by mentoring junior students, I often got a chance to look at familiar things at a different angle, and the interactions with them honed my communication skills to develop smooth collaboration.

Last but not the least, I must thank my close companions and my family. They talk to me, listen to me, and always embrace me with warm hearts when I see them. Their long-lasting support during my studying abroad and the pandemic is one of the main reasons why I can survive my PhD career. I sincerely thank you and love you.

-Hung-Yu Yang

LIST OF FIGURES

Figure

1.1	Illustration of the characteristic bands in Dirac and Weyl semimetals.	3
2.1	Flow chart of a typical flux growth.	12
2.2	EDX spectrum of a LaAs crystal sample.	18
2.3	Configurations of four-probe resistivity measurements.	20
2.4	Squeeze test.	23
2.5	Attempt to homogenize current using area contacts.	28
2.6	Spurious orbit revealed by its RUC coordinates.	34
3.1	X-ray diffraction, magnetoresistance, and Hall effect of LaAs.	50
3.2	Results of the ARPES experiment conducted on a LaAs single crystal	52
3.3	Band structure of LaAs.	54
3.4	Quantum oscillations in LaAs and a multiband model fit.	56
3.5	XMR and Magnetism in HoBi.	64
3.6	Neutron results and phase diagram of HoBi.	66
3.7	Magnetoresistance, onset of XMR, and the complete phase diagram of HoBi.	69
3.8	Band structure and quantum oscillations of HoBi.	71
4.1	Crystal structure of $\text{PrAlGe}_{1-x}\text{Si}_x$	79
4.2	Magnetic properties of $\text{PrAlGe}_{1-x}\text{Si}_x$	81
4.3	Band structure, Fermi surface, and Weyl nodes of $\text{PrAlGe}_{1-x}\text{Si}_x$	83
4.4	Resistivity of $\text{PrAlGe}_{1-x}\text{Si}_x$ as a function of temperature.	84
4.5	Resistivity and Hall effect of $\text{PrAlGe}_{1-x}\text{Si}_x$ in a magnetic field.	86
4.6	Anomalous Hall effect in $\text{PrAlGe}_{1-x}\text{Si}_x$	87
4.7	Non-collinear order, non-centrosymmetric structure, and anomalous Hall effect in CeAlSi.	96
4.8	Magnetic structure of CeAlSi.	98
4.9	Band structure and Weyl nodes in CeAlSi.	101
4.10	Anisotropic AHE of CeAlSi and its E_F dependence revealed by QO.	103
A.1	Normalized resistivity of LaAs and LaBi.	111
A.2	k_z dispersion in LaAs.	115
B.1	Magnetoresistance of HoBi with $H \parallel [001]$ and $[110]$	117

B.2	Magnetization data of HoBi with $H \parallel [111]$, $[110]$, and $[001]$ directions	117
B.3	Resistivity features and the AFM order.	118
B.4	Features in transport, magnetization and neutron data.	119
B.5	Band structures calculated by different U in HoBi.	120
B.6	Extraction of effective masses in HoBi.	121
C.1	Rietveld refinement of powder XRD data for $\text{PrAlGe}_{1-x}\text{Si}_x$.	124
C.2	Second harmonic generation data of $\text{PrAlGe}_{1-x}\text{Si}_x$.	125
C.3	Curie-Weiss analysis for $\text{PrAlGe}_{1-x}\text{Si}_x$ for $x = 0, 0.5$, and 1 .	126
C.4	DFT calculations for $\text{PrAlGe}_{0.5}\text{Si}_{0.5}$.	127
C.5	Data used to extract R_0 and R_S in $\text{PrAlGe}_{1-x}\text{Si}_x$ compounds for $x \leq 0.5$.	128
C.6	Data used to extract R_0 and R_S in $\text{PrAlGe}_{1-x}\text{Si}_x$ compounds for $x > 0.5$.	129
C.7	Quantum oscillation and calculated anomalous hall conductivity of $\text{PrAlGe}_{1-x}\text{Si}_x$.	131
D.1	Rietveld refinement analysis of Powder XRD and neutron data for CeAlSi.	133
D.2	Second harmonic generation data of CeAlSi.	134
D.3	Temperature dependence of M v.s. H curves in CeAlSi.	136
D.4	Neutron diffraction data of CeAlSi.	137
D.5	Scanning SQUID Imaging of FM domains in CeAlSi.	139
D.6	Energy dispersion of the Weyl quasiparticles in CeAlSi.	141
D.7	ρ_{xx} Data.	142
D.8	Quantum oscillation data of CeAlSi.	144
D.9	ρ_{zy}^A and $R_S M$ data of CeAlSi.	146

LIST OF TABLES

Table

3.1	Quantum oscillation frequencies and effective masses in HoBi. . .	71
A.1	Carrier densities and mobilities of LaAs.	112
A.2	Calculations of Fermi volumes	113
C.1	EDX results for various $\text{PrAlGe}_{1-x}\text{Si}_x$ samples. The atomic weights derived from EDX spectra are normalized to Pr content. These results are subject to an error of ± 0.05	123
D.1	Rietveld refinement parameters for CeAlSi.	133
D.2	Momentum space locations and energies of the Weyl nodes in CeAlSi with [110] ferromagnetic order.	140
D.3	EDX results for CeAlSi crystals grown by several different methods.	143
D.4	Determination of E_F from quantum oscillations for CeAlSi	145
D.5	Effective masses of CeAlSi	146

LIST OF SYMBOLS

Vectors are represented by bold characters. Scalars and tensors are italicized. Magnitude of vectors and components of tensors are also italicized with proper subscripts.

Some notes on \mathbf{B} and \mathbf{H} fields: For nonmagnetic materials, $\mathbf{B} = \mu_0\mathbf{H}$ and \mathbf{B} and \mathbf{H} fields are basically interchangeable up to the constant μ_0 (permeability of free space). Since \mathbf{B} is the fundamental term linked to the Lorentz force, it is often used in theoretical derivations in this dissertation. On the other hand, \mathbf{H} is directly determined by the free current sent through a coil in experiments, so it is often adopted when presenting experimental data (in units of tesla with μ_0 omitted). For magnetic materials, especially ferromagnets, the relation between the two fields changes to $\mathbf{B} = \mu_0(\mathbf{H} + \mathbf{M})$. As a result, the external \mathbf{B} and \mathbf{H} fields will be different from the internal ones, which are influenced by demagnetizing fields. For the ferromagnetic materials studied in this dissertation, demagnetizing fields do not change the physics we are interested in significantly, so the corrections by demagnetizing fields will not be implemented explicitly.

χ	magnetic susceptibility
\mathbf{B}	magnetic field in the fundamental sense
\mathbf{E}	electric field
\mathbf{H}	magnetic field that is controlled in experiments
\mathbf{J}	current density
\mathbf{M}	magnetization
\mathcal{A}	Berry connection
\mathcal{B}	Berry curvature
ρ	resistivity tensor
ρ_{ij}	component of resistivity tensor
σ	conductivity tensor
σ_{ij}	component of conductivity tensor

E_F Fermi level
 I electrical current
 R electrical resistance

LIST OF ABBREVIATIONS

AHC anomalous Hall conductivity

AHE anomalous Hall effect

ARPES angle resolved photoemission spectroscopy

DFT density functional theory

DOS density of states

EDX energy dispersive X-ray

FT Fourier transform

FM ferromagnetic

GGA generalized gradient approximation

LDA local density approximation

mBJ modified Becke-Johnson

MR magnetoresistance

PBE Perdew-Burke-Ernzerhof

QO quantum oscillation

RUC reciprocal unit cell

SHG second harmonic generation

SKEAF supercell k-space extremal area finder

SOC spin-orbit coupling

STM scanning tunneling microscopy

WSM Weyl semimetal

XMR extreme magnetoresistance

XRD X-ray diffraction

CHAPTER I

Introduction

Since the discovery of quantum Hall effect [1, 2], the notion of topology has greatly reshaped the research direction in condensed matter physics, and the hunt is on for systems with nontrivial topology. A variety of topological phases has been identified and realized in real materials, including topological insulators [3–9], Dirac semimetals [10–14], and Weyl semimetals (WSMs) [15–17], etc. One of the reasons why these materials are interesting, is that their topological states can potentially host novel electromagnetic responses. To name a few, in a topological insulator, the unusual spin texture locked with momentum forbids backscattering and leads to high mobility of the Dirac state [7, 18, 19]; the quantum anomalous Hall effect in a doped topological insulator [20, 21] originates from a chiral edge mode that does not dissipate any energy as the electrical current flows [22, 23]. In topological semimetals [24], there have also been reports of novel responses, such as giant magnetoresistance [25–27] due to topological protection, negative magnetoresistance led by chiral anomaly [28–31], and giant anomalous Hall effect (AHE) contributed by the topological nodal points [32–34]. However, it is generally more difficult to establish the novel responses in topological semimetals, mainly because of the following two reasons: 1) the topological nodes are usually so far away from the Fermi level that they are not expected to dominate the Fermi

surface, and 2) there is no gap in a semimetal to easily exclude the topologically trivial states, which can play a significant role in experiments and cast doubt on the results being topological. In order to harness the power of topological states to make functional devices [35], it is important to search for new candidates and explore new phenomena that purely result from topological states. In light of this line of thought, in this dissertation, case studies of rare-earth monopnictides and RAlX material family are performed, different electromagnetic responses are studied in depth, and their topological aspects are revealed. In this chapter, I will first discuss the basics of topological semimetals, and then introduce relevant topological responses in the aforementioned two material systems.

1.1 Topological Semimetals

One defining signature in topological semimetals is their gapless, linearly dispersive bands, described by relativistic Dirac equations. Figure 1.1 shows such typical band structures for Dirac and Weyl semimetals, and an intuitive picture to go from one to the other. To generate a Weyl semimetal, one may start from a Dirac semimetal, where the bands are doubly degenerate. By breaking a symmetry in a crystal, usually inversion or/and time-reversal symmetry, the degeneracy is lifted and a pair of linear bands of opposite chiralities (+ or – in Fig. 1.1) emerges. Particles on this pair of bands are spin-momentum locked, meaning that they can only propagate in parallel or antiparallel to their spins depending on their chiralities, and the scattering events are largely limited [25–27]. In particular, the band touching points in these bands, termed *Weyl nodes*, are the key to the topological aspects and novel responses in WSMs.

Weyl nodes are intimately connected to the Berry connection \mathcal{A} , Berry curva-

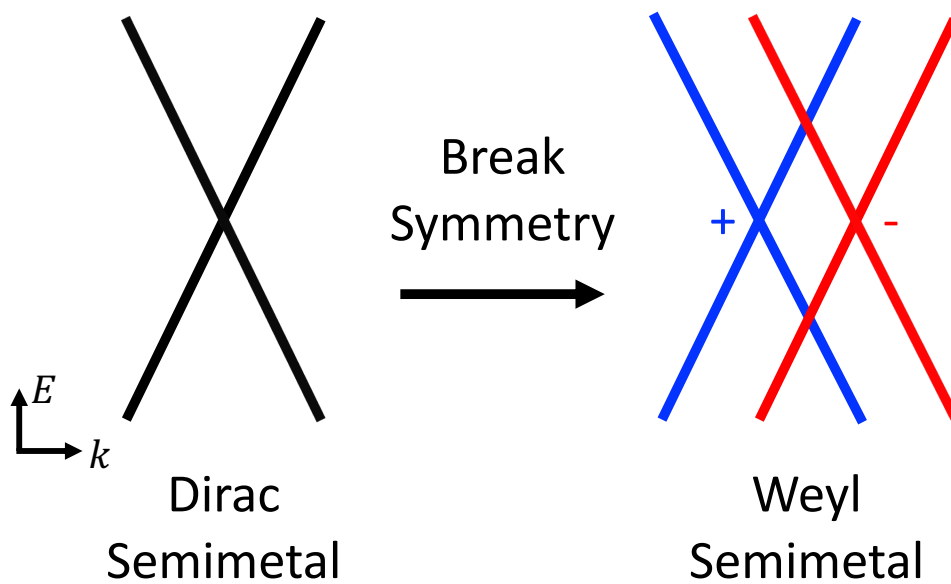


Figure 1.1: Illustration of the characteristic bands in Dirac and Weyl semimetals. The Dirac cone in a Dirac Semimetal splits into a pair of Weyl cones of opposite chiralities when one or more symmetries are broken.

ture \mathcal{B} , and Berry phase γ , which are defined as follows:

$$\mathcal{A}(\mathbf{k}) = -i \langle u(\mathbf{k}) | \nabla_{\mathbf{k}} | u(\mathbf{k}) \rangle, \quad (1.1)$$

$$\mathcal{B}(\mathbf{k}) = \nabla_{\mathbf{k}} \times \mathcal{A}(\mathbf{k}), \quad (1.2)$$

$$\gamma = \int_{\mathcal{S}} \mathcal{B}(\mathbf{k}) \cdot d\mathbf{S} \quad (1.3)$$

where \mathbf{k} is the crystal momentum, and \mathcal{S} is some area in the momentum space (band indices are omitted here for simplicity). From Eq. 1.1 and Eq. 1.2, we can see the relation between \mathcal{A} and \mathcal{B} is analogous to the relation between the vector potential \mathbf{A} and magnetic field \mathbf{B} ; \mathcal{B} can thus be imagined as a “fictitious magnetic field” that can deflect electrons like \mathbf{B} . However, one thing of \mathcal{B} that is in strong contrast to \mathbf{B} lies in Eq. 1.3. The integral in Eq. 1.3 over a closed surface reveals the number of monopole charges enclosed inside the surface, so it always returns zero for \mathbf{B} . The same integral for \mathcal{B} , though, returns a *quantized* 2π (-2π) Berry phase if the integrated surface encloses a Weyl node of positive (negative) chirality. In this regard, the quantized Berry phase corresponds to a nontrivial topological invariant Chern number ± 1 , and Weyl nodes can be interpreted as magnetic monopoles of Berry curvature. Since magnetic monopoles are yet to be found in high energy physics, their appearance in condensed matter physics is interesting and attracts lots of attention in recent years [24]. Besides, given an \mathbf{E} and a \mathbf{B} field with $\mathbf{E} \cdot \mathbf{B} \neq 0$, electrons residing on Weyl nodes of opposite chiralities lose balance and lead to the so-called chiral anomaly [28–31]. Weyl nodes can also generate significant Berry curvature that may drive a giant AHE [32–34]. These findings suggest that Weyl nodes can be the source of novel responses in WSMs, and more interesting phenomena may emerge as we continue to search for ideal candidates.

1.2 Topological States and Extreme Magnetoresistance (XMR)

In general, the Dirac states in topological insulators/semimetals may lead to high mobility and large magnetoresistance due to the prevention of backscattering [18, 25, 27, 36]. The linear dispersion of Dirac states comes directly from the Hamiltonian $\hat{H} \propto \hat{\mathbf{s}} \cdot \hat{\mathbf{p}}$, which also guarantees the spin (denoted by Pauli matrices $\hat{\mathbf{s}}$)-momentum ($\hat{\mathbf{p}}$) locking. As a consequence, 1) electrons moving forward can only carry unidirectional spins and generate a spin-polarized current [37], 2) electrons moving forward are protected from being scattered into states with arbitrary momenta and are highly mobile, 3) once the protection mechanism breaks down as the applied magnetic field breaks the time-reversal symmetry, scatterings start to kick in and enhance magnetoresistance greatly. In this spirit, rare-earth monpnictides are studied in depth to understand the extreme magnetoresistance (XMR).

The nontrivial topology of rare-earth monpnictides was first proposed by Zeng *et al.* in nonmagnetic LaX (X=N, P, As, Sb, Bi) [38]. Since these materials are of NaCl structure and preserve inversion symmetry, their topological properties (except for LaN, which has a different topological character and we omitted it for the rest of our discussion) can be characterized by the Fu-Kane formula [4]:

$$-1^\nu = \prod_i \delta_i, \quad (1.4)$$

where the RHS represents the product of parity eigenvalues at all time-reversal invariant momenta for all occupied bands. If the product gives $\nu = 1$, the material is a strong Z_2 topological insulator [3, 4]. Although LaX materials are not real insulators and there are trivial bands crossing E_F , there is a direct band gap that separates the valence band and conduction band and allows for the application of Fu-Kane formula; the Dirac surface states together with trivial bulk bands are confirmed by DFT calculations [38]. In short, LaX materials are topologi-

cal semimetals in the following sense: they are bulk semimetals with topological surface states.

The work by Zeng *et al.* inspires experimental investigations of XMR caused by nontrivial topology in LaX material family. [26, 27, 39, 40]. XMR features 1) a plateau-like $\rho(T)$ profile at high magnetic fields, and 2) an extremely large magnetoresistance, typically of $\sim 10^4 - 10^6\%$ at 9 tesla [26, 27]. Following our previous discussion, XMR in pinctides were sometimes attributed to their topological states [41–45]. However, because of these materials are bulk semimetals in nature, *electron-hole compensation* can well serve as an alternative explanation of XMR [46]. Such a mechanism is not related to topology, and can be understood in the following way: consider a compensated semimetal, with equal amount of electron and hole carriers flowing with the same mobility. As the magnetic field increases, both electrons and holes are subject to the Lorentz force and deflected towards the transverse direction. Since the transverse electrons and holes exactly cancel with each other, a Hall voltage can not be built up to counteract the Lorentz force, which effectively disrupt the forward motion of carriers and increase the magnetoresistance greatly.

Both LaBi and LaSb exhibit XMR [26, 27, 39, 40], while nontrivial topology [47–52] and electron-hole compensation [39, 51] seem to concur. The concurrence blurs the interpretation of the XMR in LaX materials, but it also opens up a natural route to clarify the origin of XMR: if either topology or compensation can be removed and an XMR is still observed, the origin of XMR will be unambiguous. As a result, we targeted and synthesized a new member in the LaX material family LaAs, where there is a lack of nontrivial topology but compensation and XMR remain, and the origin of XMR is resolved [53] (see Sec. 3.1 in Chapter III).

An interesting question that emerges from this study is the interplay between XMR and magnetism. For nonmagnetic XMR materials, the field dependence of

resistivity $\rho(H)$ follows a robust quadratic curve guaranteed by the electron-hole compensation [26, 27, 39, 40]. The reports of XMR in magnetic rare-earth mononictides show that their $\rho(H)$ profiles are surprisingly similar to their nonmagnetic analogs, despite their complicated magnetic phases in fields [54–58]. These findings seem to suggest that XMR is robust against magnetism. To explore such a possibility, we targeted HoBi with the most magnetic ion Ho^{3+} , and found that the XMR profile can be strongly modified under some circumstances (see Sec. 3.2 in Chapter III).

1.3 Anomalous Hall Effect (AHE) in Magnetic Weyl Semimetals

The discovery of AHE by Edwin Hall is an intriguing phenomenon [59]; when a forward electrical current is injected into a ferromagnetic material, an anomalous transverse current is generated spontaneously without applying a magnetic field [60, 61]. From then on, physicists have come up with possible mechanisms of AHE [62–64], but it is not until recently that Berry curvature is recognized as the key contribution to AHE [65–67]:

$$\sigma_{AH} = -\frac{e^2}{\hbar} \sum_n \int \frac{d\mathbf{k}}{(2\pi)^3} f_{n,\mathbf{k}} \mathcal{B}_z(n, \mathbf{k}), \quad (1.5)$$

where n is the band index including all occupied bands and f is the Fermi function in equilibrium. This idea was put to test in iron (bcc Fe), where the first-principles calculation of anomalous Hall conductivity (AHC) using Eq. 1.5 agrees with the experiments [68]. Since Weyl nodes are monopoles of Berry curvature (see Sec. 1.1), it seems natural to search for AHE in ferromagnetic (FM) WSMs [32, 33], and indeed a giant AHE was observed in several candidates [34, 69]. The separation between each pair of Weyl nodes determines the potentially large contribution to

AHE from Weyl nodes.

However, several key questions have been overlooked in the study of AHE in magnetic WSMs. First of all, although the intrinsic contribution from Berry curvature to AHE has been widely discussed in WSMs, extrinsic contributions due to impurity scatterings in these materials are often ignored [63, 64]. These contributions turn out to be significant; for example, in the FM Chern insulator candidate Fe_3Sn_2 , the extrinsic part of AHE is nearly five times larger than the intrinsic part of AHE caused by Berry curvature [70]. Furthermore, in most of the WSMs, the Weyl nodes are so far away from the Fermi level that they are not expected to contribute significantly to the transport properties (e.g. 60 meV away from the E_F in $\text{Co}_3\text{Sn}_2\text{S}_2$ [34]). The long distance between Weyl nodes and Fermi level also leads to a large Fermi surface, which favors scatterings and extrinsic AHE. These observations raise the following questions: in magnetic WSMs, what is the role of extrinsic contributions, and is the Berry curvature contribution to AHE always robust because of topological nodes?

Furthermore, although Weyl nodes can host a large Berry curvature in principle, they are not the only source; topologically trivial bands gapped out by Zeeman field and spin-orbit coupling (SOC) can also generate Berry curvature [71]. In other words, the giant AHE is not unique to magnetic WSMs, and may be largely irrelevant to Weyl nodes especially when they are away from the E_F and the Fermi surface is comprised of bands gapped out by SOC [34]. Hence, we ask the question: what is the smoking gun of Weyl nodes? Can we find a transport response, that can only be induced by Weyl nodes?

To answer these questions, we focus on the RAlX material family (R = rare-earths, X= Ge/Si) [72]; these materials generate WSM phase by breaking both inversion and time-reversal symmetries simultaneously, in stark contrast to the existing candidates that only break one of them [16, 17, 34]. The advantage of

breaking an additional symmetry is two-fold. Firstly, it provides a reliable way of creating magnetic WSMs. The WSM phase is established by breaking inversion symmetry, and the breaking of time-reversal symmetry shifts the Weyl nodes. The Weyl nodes do not easily annihilate in such a case, and a magnetic WSM is almost guaranteed to exist even if the magnetic structure is complicated. Secondly, since each symmetry-breaking can shift the Weyl nodes on its own, additional symmetry-breaking means additional degrees of freedom to tune the separation between Weyl nodes, which is the key to the electromagnetic responses of WSMs. By effectively tuning the distribution of Weyl nodes in the Brillouin zone, we may be better off finding interesting responses induced by Weyl nodes.

To understand the role of extrinsic contributions and the robustness of Berry curvature contribution to AHE in magnetic WSMs, we targeted $\text{PrAlGe}_x\text{Si}_{1-x}$ with $x = 0, 0.25, 0.5, 0.75, 0.85, 1$. In these materials, we keep the intrinsic contribution to AHE intact by keeping the magnetic and topological properties almost unchanged, but the extrinsic contribution is effectively tuned by changing the Fermi surface. When looking into the AHE of all these materials, we found that there is a rare transition from intrinsic AHE to extrinsic AHE when x goes from 0 to 1. Since only the Fermi surface is changing as x goes from 0 to 1, we were able to argue that the extrinsic contribution to AHE can indeed dominate even in magnetic WSMs with significant amount of Berry curvature (see Chapter IV Sec. 4.1).

To find a new smoking gun of Weyl nodes, we studied the Hall effect in CeAlSi . When the magnetic field is applied along the magnetic easy-axis, we observed a standard AHE as those observed in Fe and other FM WSMs. However, when the magnetic field is applied along the hard-axis, we observed a mysterious hysteresis in the Hall response which we call the Loop Hall effect. With a detailed study of the sample dependence of Loop Hall effect, we found that this effect *only* appears

in the samples where the Fermi level is near (< 1 meV) a group of Weyl nodes W_2 . The proximity between the Fermi level and Weyl nodes in CeAlSi is rare, and a new Hall response solely induced by Weyl nodes is established (see Chapter IV Sec. 4.2).

CHAPTER II

Methodology

2.1 Crystal Growth and Characterization

To investigate the electromagnetic responses in topological semimetals, it is important to grow single crystals. Compared to polycrystalline samples where many tiny crystals orient randomly and cluster together, single crystals orient uniformly and possess well-defined crystal geometry, which allows us to study how the response changes as the current and/or field directions vary with respect to crystal axes. For magnetic materials, it is particularly important to identify the easy axis of magnetic ordering during measurements, because transport responses (such as anomalous Hall effect) can be highly coupled to the direction of electrical current relative to the magnetic easy axis. Below I will briefly describe the way of making single crystals studied in this dissertation, and the ways of characterizing their crystal structures and chemical compositions.

2.1.1 Flux Growth

Flux growth method was first employed more than 100 years ago, and it has been used to grow intermetallic compounds extensively ever since [73, 74]. It is often used to grow single crystals of known compounds; exploratory synthesis is also possible with flux growth, while it is less common since intermetallic com-

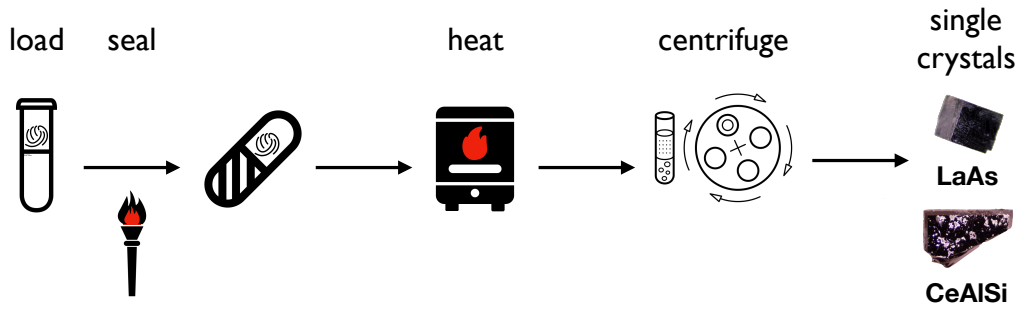


Figure 2.1: Flow chart of a typical flux growth. Graphical icons are obtained from the Noun Project (“Vial” by faisalover, “Wool” by yurr, “Torch” by Marco Livolsi, “Pill” by Bohdan Burmich, “furnace” by ProSymbols, “plasma and blood” by Olena Panasovska from thenounproject.com.).

pounds can have mixed ionic and covalent bond characters which are hard to predict. Compared to classical solid-state synthesis, which makes polycrystalline samples by firing starting materials in stoichiometric ratio at high temperatures, flux method has the following advantages: 1) the addition of flux reduces the melting temperature of starting materials and leads to high diffusion rates, which allow the target material to crystallize at much lower temperatures, 2) compounds other than the thermodynamically most stable one may be accessible because of the reduction of reaction temperatures. On the other hand, flux growth may suffer from several drawbacks, such as the inclusion of flux inside and/or on the surface of crystals, which may be removed by immersion in dilute acid or base, or mechanical sanding.

Fig. 2.1 shows the general procedure of growing single crystals by flux growth method. Each step is briefly explained as follows:

- **Load:** Typically, starting materials, such as lumps or ingots of each element in the target material, are loaded in a container and then put inside a silica tube. A common choice of the container is alumina (Al_2O_3) crucibles because they are inert and can resist high heat. It is also possible to put

the starting materials straight in the silica tube to increase the yield if they do not react with silica. Depending on the chemical properties of starting materials, different containers such as tantalum crucibles may be used. As for the outside tube, silica tubes do a good job for most materials and for temperatures below $\sim 1200^\circ\text{C}$ (above which the silica starts to soften), while tantalum or steel tubes may be more favorable in some occasions. Finally, silica wool is inserted into the tube to plug the space on top of the container sitting at the bottom. It serves as a strainer to separate the liquid flux and the crystals in the centrifuge step (see below).

- Seal: After the container and the silica wool are loaded, the silica tube is sealed under vacuum with a torch made of methane-oxygen flame. This way, the starting materials are prevented from oxidation and the reaction happens only among the ingredients.
- Heat: Once sealed, the silica tube is transferred to a box furnace, heated up to a high temperature (T_{high}) and dwell for a certain time to ensure that everything has melt and formed a homogeneous liquid mixture. The tube is then slowly cooled down to a lower temperature (T_{low}), at which single crystals form while the flux remains liquid. Changing T_{high} and T_{low} may result in different products even for the same starting materials, and the variation of the dwelling time may also affect the crystal growth. For example, for volatile element such as As at high temperatures, it is found that higher dwelling time is needed to dissolve more As in the liquid mixture and facilitate the crystal growth [53].
- Centrifuge: When the temperature cools down to T_{low} , solid crystals may have formed and be soaked in the bath of liquid flux. To separate them and extract the crystals mechanically, the tube is quickly transferred from the

furnace to a centrifuge with the tube being upside down. As the centrifuge spins, the liquid flux will be spun off through tiny gaps inside the silica wool, while the crystals remain on the crucible side. The crystals can be mechanically extracted after the tube cools down to room temperature.

- Single crystals: As-grown LaAs and CeAlSi crystals are shown here as examples of final products of flux growth. The morphology of these crystals reflects their microscopic unit cells and suggests that they host extended single phases; for example, LaAs has a cubic unit cell microscopically, and the morphology is also a cube with the sharp edges defining three orthogonal crystal axes.

After going through the above procedures and collecting the resultant crystals, it remains a question what are actually made until the crystals are characterized (it is clear though if nothing is left in the crucible). To make sure I have got the crystals I aim to grow, two powerful characterization tools are commonly used and they are introduced in two subsequent sections below.

2.1.2 Powder X-ray Diffraction and Rietveld Refinement

X-ray diffraction (XRD) is a very useful tool to determine crystal structures of numerous compounds. The main idea of XRD is described by Bragg's law:

$$2d \sin \theta = n\lambda, \tag{2.1}$$

where d is the distance between neighboring diffracting planes, θ is the incident angle of X-ray with respect to the diffracting planes, n is any integer, and λ is the wavelength of the incident X-ray. Once the condition in Eq. 2.1 is satisfied, the X-ray reflected by different layers of diffracting planes that are periodically aligned interfere with each other constructively; the detected X-ray intensity is then largely

enhanced at the angle θ , but is otherwise vanishingly small. As a consequence, as the incident X-ray sweeps from low to high angles, the X-ray intensity will peak at θ and vanishes at other angles. Such an XRD pattern reflects unique information of atomic positions and crystal structures of different compounds.

Eq. 2.1 works for a piece of single crystal which orients uniformly and there is no misalignment for any set of diffracting planes. Performing XRD on a single crystal of a new compound that has not been discovered before is necessary and important to solve its crystal structure. However, to gather complete information, XRD patterns have to be measured for different sets of diffracting planes, and that means a lot of re-orienting crystals and repeated sweeps of X-ray for different orientations. In addition, single crystals may not be easily available (see Sec. 2.1). For practical purposes, it is sometimes more favorable to perform XRD on powder samples (powder XRD), which can be finely ground from single crystals, or be made directly from solid-state synthesis. Since powders comprise tiny crystals of all possible orientations, all the information is gathered by one single X-ray sweep. It is also easier to acquire a mass of powders compared to a single crystal of the same mass, so the signal of powder XRD can be easily enhanced.

In the study of topological materials, it is not rare to rediscover a material and study its topological properties. In such a case, the target material may have been found and studied in the past, and its crystal structure may have been solved by XRD. However, a new characterization of its band structure may show that it hosts a nontrivial topological phase, an intriguing research problem that is worth further investigations. Thus, the main goal in studying this material is not to understand its crystal structure from scratch; researchers may simply want to make exactly the same thing as reported and study its newly proposed topological properties. Or, it could be that in the past only polycrystalline samples were synthesized, and now researchers would like to make single crystals of the same

material which may show exotic phenomena due to its nontrivial topology.

For these two cases, once the target material is synthesized, it is convenient to use powder XRD to quickly characterize the product and compare its XRD pattern to the literature. If the pattern reveals an impurity phase or a completely different compound, the synthesis steps need to be modified or a different method may be adopted to try to synthesize the target material. If the pattern shows a perfect match, the target material is successfully made and researchers can move on to study its topological properties. Such a procedure is often carried out in this dissertation.

Despite being a quick characterization tool, powder XRD can be used to solve complicated crystal structure through Rietveld refinement [75]. Rietveld refinement solves the crystal structure by modelling the X-ray pattern theoretically to match the experimental one. By changing the space group, atomic positions, vacancies, etc., the difference between the modelled XRD pattern and the experimental one may increase or decrease, and the crystal structure is solved once the difference achieves a minimum. This method is very powerful, while it also has some limitations. For example, the difference between two modelled patterns of two different space groups may not be large enough for one to say one is a better description of the experimental pattern than the other. This is exactly the case of RAlX material family [72]; the two space groups $I4_1amd$ and $I4_1md$ generate very close XRD patterns through Rietveld refinement and it is not possible to distinguish between them in this way [76–78]. However, $I4_1amd$ breaks the inversion symmetry while $I4_1md$ preserves it, so the topological properties changes drastically depending on which space group the material belongs to. In this situation, other methods such as second harmonic generation (SHG) is needed to complement the analysis of Rietveld refinement.

2.1.3 Energy Dispersive X-ray Spectroscopy

Energy dispersive X-ray (EDX) spectroscopy can be used to determine chemical compositions of materials, and is very useful in checking the stoichiometry, impurity phases, or doping level of a certain dopant. Generally speaking, EDX spectroscopy involves the following process: a high-energy electron beam or X-ray impinges on the sample surface to kick out core electrons, the energy level of which is subsequently occupied by electrons at higher levels; such occupations are accompanied by an emission of radiative X-ray, which is captured by a detector and analyzed. Since the core electron levels are deeply embedded in an atom and are not subject to chemical bonding, the X-ray induced by the transitions between these levels are basically unchanged from compound to compound and serve as unique fingerprints for each atom. Fig. 2.2 shows a typical EDX spectrum of a piece of LaAs sample. Different peaks represent different transmission lines characteristic of La and As atoms, as labeled in the figure. The relative weight of these lines are further analyzed to derive the chemical compositions of the measured specimen.

2.2 Measurement Techniques

To understand the electromagnetic responses of topological semimetals, several measurement techniques are utilized to probe these responses. Sections 2.2.1 and 2.2.2 are measurements applicable to general intermetallic compounds, while section 2.2.3 is developed specifically for detecting the negative longitudinal magnetoresistance induced by chiral anomaly in Weyl semimetals [31]. The basic principles are reviewed, and applications and examples are discussed.

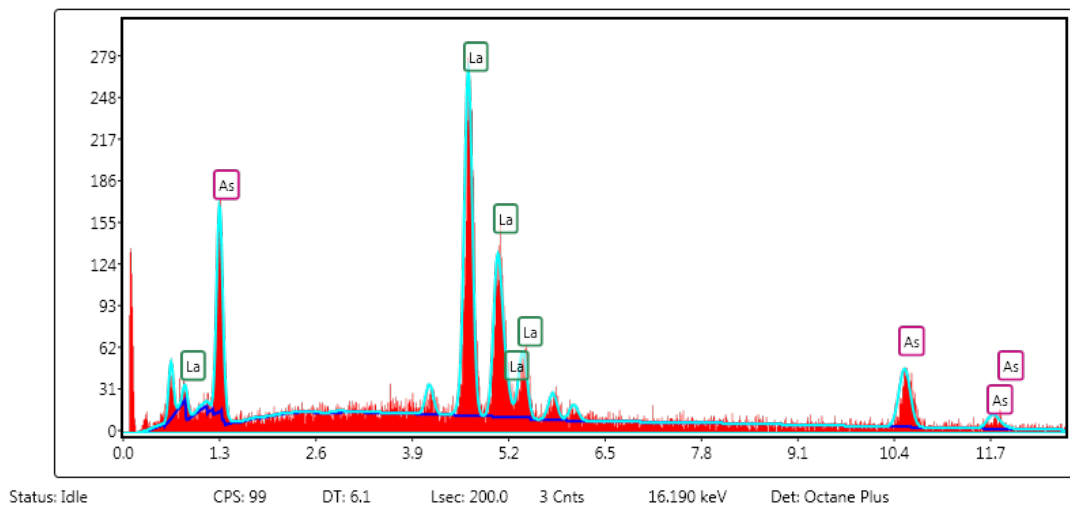


Figure 2.2: EDX spectrum of a LaAs crystal sample. The x-axis is the energy of the scattered X-ray in units of keV, and the y-axis is the count of the detector in units of count per second (CPS). The blue curve is the background, the cyan curve is the fitting to the EDX data. The low-energy peak is from the carbon tape used to fix the specimen and is ignored in the analysis.

2.2.1 Magnetization

The magnetization \mathbf{M} is measured by applying Faraday's law of induction. The idea is as follows: the sample is mounted on a rod, which translates through superconducting pickup coils and induces a current in the coils. The coils are coupled to a sensitive superconducting quantum interference device (SQUID) that converts current to voltage. The SQUID voltage is fitted to a response function as a function of sample position to extract the magnetization of a sample.

The magnetization is a macroscopic quantity that reveals a lot of important information of a material, including:

- Effective moment: Using the magnetic susceptibility ($\chi = |\mathbf{M}|/|\mathbf{H}|$) measured in a weak field \mathbf{H} , the effective moment can be extracted by fitting $\chi(T)$ to the Curie-Weiss law [79]. The effective moment helps us confirm the magnetic atom in a material, and its valence state may be important in realizing a specific model [80].
- Curie-Weiss temperature: The Curie-Weiss temperature, which is also derived from the Curie-Weiss law, tells us the dominating interaction in a magnetic material and its strength.
- Transition temperature: When a system goes through a transition from a paramagnetic state to a magnetically ordered state, its susceptibility typically shows an anomaly (discontinuity) marking the transition temperature. This number is sometimes combined with the Curie-Weiss temperature to get the so-called frustration index, which is useful in knowing the degree of frustration of spins in a certain material [81].

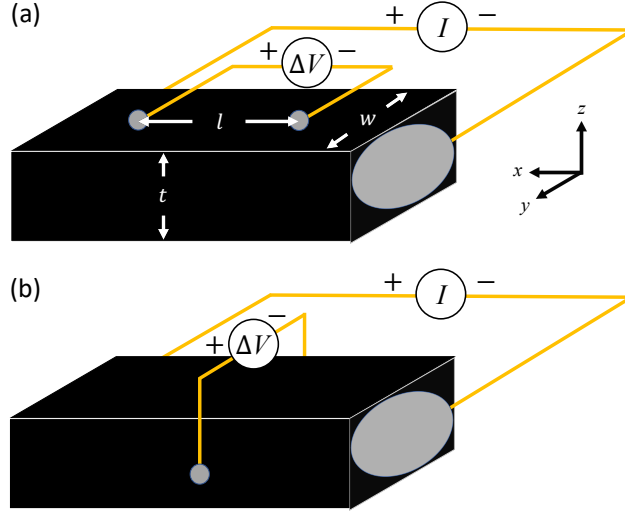


Figure 2.3: Configurations of four-probe resistivity measurements. (a) Configuration for measuring ρ_{xx} . (b) Configuration for measuring ρ_{yx} . Silver paint (Gray area) is applied as a conductive adhesive to connect the contact wires and the sample surface. The current leads (I) send electrical current through the sample, and the voltage leads (ΔV) measure the voltage drop between the two contact points defining l . l , w , and t determine the geometric factor of the data.

2.2.2 Electrical Resistivity

The electrical resistivity tensor ρ is the inverse of the conductivity tensor σ , which describes the current response \mathbf{J} driven by an electric field \mathbf{E} [82, 83]:

$$E_i = \rho_{ij} J_j, \quad J_i = \sigma_{ij} E_j. \quad (2.2)$$

In experiments, in order to measure the component ρ_{xx} , for example, we need to pass a current I and measure the voltage drop ΔV along the x -axis (Fig. 2.3(a)), and derive resistance R via Ohm's law:

$$\Delta V = IR, \quad (2.3)$$

where R is linked to ρ_{xx} as follows:

$$\rho_{xx} = \frac{E_x}{J_x} = \frac{E_x l w t}{J_x l w t} = \frac{\Delta V w t}{I l} = R \frac{w t}{l} = R \frac{A}{l}. \quad (2.4)$$

In Eq. 2.4, A is the cross section of the sample and is determined by the width w and the thickness t , while l is the length between the two voltage leads (Fig. 2.3(a)). For a four-probe measurement shown in Fig. 2.3, the pair of current leads and the pair of voltage leads are independent of each other and well separated. Compared to a two-point setup where the current is sent and the voltage is picked up through the same pair of contacts, a four-probe measurement only allows a negligible amount of current flows through the voltmeter. As a consequence, the resistance of wires and leads, and contact resistance are largely eliminated so that a four-probe measurement is able to give more accurate results of resistance of materials.

In the presence of an external magnetic field \mathbf{B} , say, along the z -axis, the charge carriers can move in the direction transverse to the current; this phenomenon is the renowned Hall effect [59, 84]. To measure such a transverse response, say, ρ_{yx} , the contact geometry should be changed accordingly, as shown in Fig. 2.3(b). ρ_{yx} can then be extracted via the relation below:

$$\rho_{yx} = \frac{E_y}{J_x} = \frac{E_y w t}{J_x w t} = \frac{\Delta V t}{I} = R t. \quad (2.5)$$

As a result, to get ρ_{yx} from R measured in Fig. 2.3(b), only the thickness t is needed to convert R to ρ_{yx} .

Ideally, the R measured in Fig. 2.3(a) and Fig. 2.3(b) are solely responsible for ρ_{xx} and ρ_{yx} , respectively. However, in reality, because of the inevitable misalignment of the voltage leads, the configuration shown in Fig. 2.3(a) can well pick up some signal contributed by ρ_{yx} ; the same thing also applies to the configuration

in Fig. 2.3(b) and some ρ_{xx} signal may be included although it aims to measure ρ_{yx} . As a result, to extract sheer ρ_{xx} and ρ_{yx} signals from the measurements, a symmetrization process is implemented, and it relies on the symmetry of ρ_{xx} and ρ_{yx} with respect to the applied field \mathbf{B} :

$$\rho_{xx}(|\mathbf{B}|) = \rho_{xx}(-|\mathbf{B}|), \quad \rho_{yx}(|\mathbf{B}|) = -\rho_{yx}(-|\mathbf{B}|), \quad (2.6)$$

where $+|\mathbf{B}|$ and $-|\mathbf{B}|$ correspond to the field applied along $+z$ and $-z$ directions, respectively. That is to say, if we denote the signal measured in Fig. 2.3(a) by ρ_{xx}^{raw} and the one in Fig. 2.3(b) by ρ_{yx}^{raw} , we can extract sheer ρ_{xx} and ρ_{yx} by the following procedure:

$$\begin{aligned} \rho_{xx}(|\mathbf{B}|) &= [\rho_{xx}^{raw}(|\mathbf{B}|) + \rho_{xx}^{raw}(-|\mathbf{B}|)]/2, \\ \rho_{yx}(|\mathbf{B}|) &= [\rho_{yx}^{raw}(|\mathbf{B}|) - \rho_{yx}^{raw}(-|\mathbf{B}|)]/2. \end{aligned} \quad (2.7)$$

Such a procedure is implemented to all of the data presented in this dissertation.

Finally, we briefly discuss the nomenclature of Hall resistivity. In general, in this dissertation, all of the signals measured with $\mathbf{H} \parallel \hat{\mathbf{z}}$ (c -axis) should be named ρ_{yx} following Eq. 2.5 defined in conventional Cartesian coordinates. In Sec. 3.1, the nomenclature ρ_{xy} is used, which would differ from ρ_{yx} by a minus sign if both would follow the definition of Eq. 2.5. However, for our purpose, ρ_{xy} in Sec. 3.1 was defined to reproduce the Hall coefficient $R_H = \rho_{xy}/H$ (whose sign convention is positive for hole carrier) and is equivalent to ρ_{yx} . As a result, despite the nomenclature is a bit confusing, the results of multiband fits in 3.1 are unchanged if we would have used the conventional nomenclature and write $R_H = \rho_{yx}/H$.

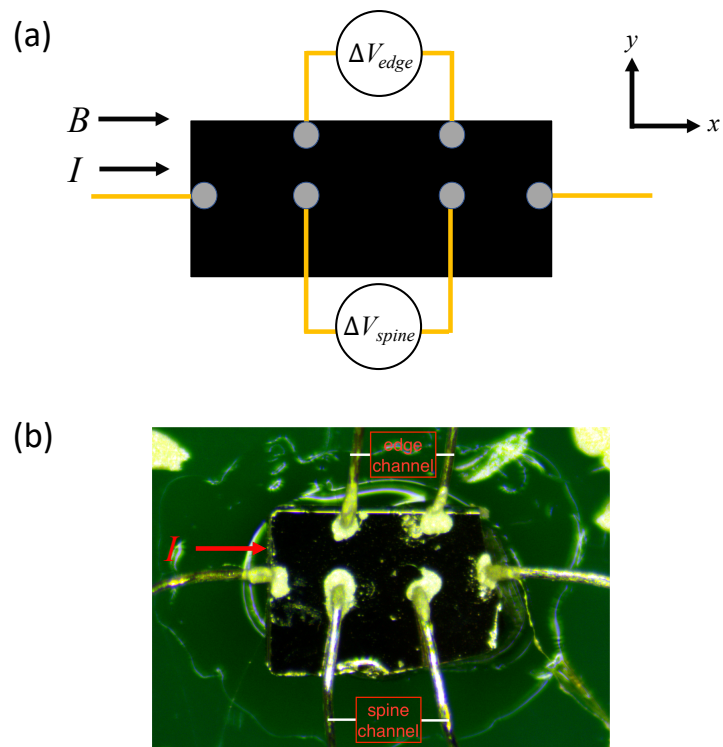


Figure 2.4: Squeeze test. (a) A schematic sketch of the contact geometry for squeeze test. (b) Squeeze test on a piece of CeAlSi sample.

2.2.3 Squeeze Test for Chiral Anomaly

Squeeze test [31] is an experimental method that aims to differentiate a current jetting effect [82] from a chiral anomaly effect [28–30, 85, 86]. Both effects lead to negative longitudinal magnetoresistance (MR) when $\mathbf{E} \parallel \mathbf{B}$; however, current jetting results from an inhomogeneous current distribution across the sample and is a classical electrodynamic effect, while chiral anomaly is induced by an imbalance between Weyl fermions of opposite chiralities and is a topological transport phenomenon. As the research on WSMs gains more and more attention, the experimental reports of WSMs are under close scrutiny, and more and more evidence shows that the reported negative MR may not be always of topological origins and could well be a result of current jetting. Squeeze test serves as an useful tool to provide insight into negative longitudinal MR in a WSM, and help us understand the effectiveness of chiral anomaly as a source of negative longitudinal MR. Below, I will introduce the basics of squeeze test, and discuss some reports of negative longitudinal MR in WSMs. This section does not intend to provide a complete treatment of negative longitudinal MR in WSMs; instead, it summarizes several key issues, and shows how we may gain more insights into this problem if squeeze tests are performed more frequently.

Figure 2.4(a) shows the contact geometry required for a squeeze test, which involves pairs of points contacts for the current $I \parallel \hat{x}$ sent along the “spine” (see figure), voltage on the spine (ΔV_{spine}), and voltage on the edge (ΔV_{edge}). As the field $\mathbf{B} \parallel \hat{x}$ is applied to the sample, the current starts to have a hard time getting to the edge, because any charge carrier that was scattered to the \hat{y} direction will suffer from the Lorentz force caused by $\mathbf{B} \parallel \hat{x}$. As a result, as the field increases, the current density J_x becomes more and more focused on the spine.

Now, let us consider the effect of such a current focusing (or equivalently, jetting) on ΔV_{spine} first. When $\mathbf{B} = 0$, the current jetting is not activated, and we

may express $\Delta V_{spine}(\mathbf{B} = 0)$ using Eq. 2.4 as

$$\Delta V_{spine}(\mathbf{B} = 0) = E_x l = \rho_{xx} J_{x,spine}(\mathbf{B} = 0) l, \quad (2.8)$$

where we drop the intrinsic field dependence of ρ_{xx} and only discuss the current jetting effect (J_x) for now¹. When $\mathbf{B} > 0$, $J_{x,spine}(\mathbf{B} > 0) > J_{x,spine}(\mathbf{B} = 0)$ because the current becomes more concentrated on the spine, and we have

$$\rho_{xx} J_{x,spine}(\mathbf{B} > 0) > \rho_{xx} J_{x,spine}(\mathbf{B} = 0) \quad (2.9)$$

$$\Rightarrow \Delta V_{spine}(\mathbf{B} > 0) > \Delta V_{spine}(\mathbf{B} = 0). \quad (2.10)$$

Without knowing the presence of current jetting, we would continue to derive the resistance using Ohm's law, $\Delta V_{spine}(\mathbf{B} > 0)$, and $\Delta V_{spine}(\mathbf{B} = 0)$:

$$\frac{\Delta V_{spine}(\mathbf{B} > 0)}{I} > \frac{\Delta V_{spine}(\mathbf{B} = 0)}{I} \quad (2.11)$$

$$\Rightarrow R_{spine}(\mathbf{B} > 0) > R_{spine}(\mathbf{B} = 0) \quad (2.12)$$

$$\Rightarrow \text{MR}_{spine} > 0, \quad (2.13)$$

where $\text{MR}_{spine} \equiv \frac{R_{spine}(\mathbf{B}>0) - R_{spine}(\mathbf{B}=0)}{R_{spine}(\mathbf{B}=0)}$. As a result, current jetting leads to a *positive* longitudinal MR on the spine channel.

On the contrary, on the edge channel, the current density decreases as the field increases ($J_{x,edge}(\mathbf{B} > 0) < J_{x,edge}(\mathbf{B} = 0)$), while the argument is otherwise the same as above. Thus, Eq. 2.10 and 2.12 become

$$\Delta V_{edge}(\mathbf{B} > 0) < \Delta V_{edge}(\mathbf{B} = 0), \quad (2.14)$$

$$R_{edge}(\mathbf{B} > 0) < R_{edge}(\mathbf{B} = 0), \quad (2.15)$$

¹For a complete treatment, Eq. 2.8 should involve a line integral across l , because J_x is not a constant. However, this subtlety does not change the qualitative behavior of current jetting and is left out for simplicity.

and lead to

$$\text{MR}_{edge} < 0, \quad (2.16)$$

where $\text{MR}_{edge} \equiv \frac{R_{edge}(\mathbf{B}>0) - R_{edge}(\mathbf{B}=0)}{R_{edge}(\mathbf{B}=0)}$. That is, current jetting leads to a *negative* longitudinal MR on the edge channel. It is this negative signal that may be falsely interpreted as an evidence of chiral anomaly, which also leads to a negative longitudinal MR.

When deriving Eq. 2.13 and 2.16, we ignored the field dependence of ρ_{xx} ($\rho_{xx}(\mathbf{B})$) as mentioned in the discussion following Eq. 2.8. If we consider the effect of chiral anomaly, however, the direction of the inequality in Eq. 2.13 may be reversed, because a chiral anomaly contributes a negative signal to longitudinal MR, but a current jetting contributes a positive signal to the same quantity on the spine channel. Whether Eq. 2.13 is reversed or not depends on the competition between chiral anomaly and current jetting. On the edge channel, Eq. 2.16 is not affected qualitatively with the presence of a chiral anomaly, because here chiral anomaly and current jetting conspire to produce negative longitudinal MR. Consequently, by considering both chiral anomaly and current jetting, two scenarios may appear:

- $\text{MR}_{spine} > 0$, while $\text{MR}_{edge} < 0$ (fail): This scenario is the same as the one when only current jetting is considered; it suggests that on both spine and edge channels, the effect of current jetting dominates, and the effect of chiral anomaly either contribute very little or does not exist. In other words, we may say the material that falls in this scenario could be 1) a WSM that fails to show a pronounced effect of chiral anomaly in its transport properties, or 2) simply not a WSM.
- $\text{MR}_{spine} < 0$, and $\text{MR}_{edge} < 0$ (pass): Here, on the spine channel, the negative longitudinal MR contributed by chiral anomaly overwhelm the positive

signal by current jetting. The edge channel usually shows a more negative signal because of the addition of both effects. If no other mechanisms are present, it can be argued that the material is a WSM showing a strong effect of chiral anomaly in its transport properties.

Now that we have understood how current jetting may lead to a negative longitudinal MR from the discussion of squeeze test, one natural solution to mitigate this effect emerges: since the difference between spine and edge channels comes from the inhomogeneous current distribution induced by point contacts of I , why not make this pair of contacts attach to the entire cross section on both sides? Presumably, such “area contacts” would allow the current to flow into the sample evenly across the cross section of the sample, and create a uniform $J(x)$ which would utterly eliminate the effect of current jetting. However, in practice, it is much more difficult to homogenize the current using area contacts than one would imagine, and the above hypothesis simply does not work without further considerations as discussed below.

To test the effectiveness of homogenizing current using area contacts, a squeeze test is performed on a piece of bismuth metal, which is not a WSM with potential chiral anomaly, and two consecutive measurements were conducted. Firstly, the contact geometry of a standard squeeze test is implemented and MR_{spine} and MR_{edge} are measured at 2 K (“point contacts” in Fig. 2.5(a) and (b), respectively). Then, on the same Bi sample, with the voltage leads on the edge and spine channels intact, we only cover both sides completely with silver paint with the hope to homogenize the current flowing into the sample, and measure MR_{spine} and MR_{edge} again (“area contacts” in Fig. 2.5(a) and (b)).

Ideally, once the point contacts of the current are changed to area contacts, the current distribution should become uniform even when a magnetic field is applied along the direction of the current. As a result, the difference between MR_{spine}

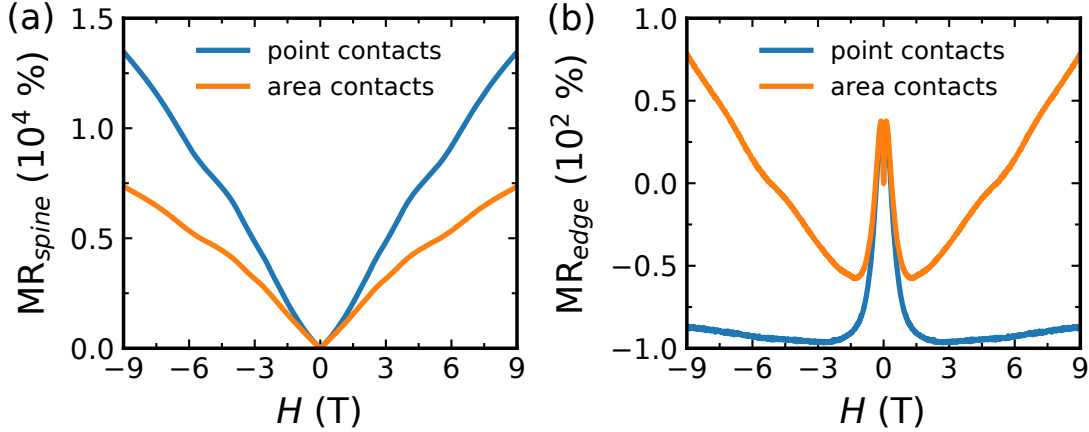


Figure 2.5: Attempt to homogenize current using area contacts. A piece of Bi was measured, and the contact geometry of a squeeze test (Fig. 2.4, point contacts) is adopted, and then changed to area contacts. The applied field is parallel to the current direction and the data are recorded at 2 K. (a) MR plotted as a function of the applied field H on the spine channel. (b) MR plotted as a function of the applied field on the edge channel. The data were recorded by Nikhil Chellam during his REU internship at Boston College, under the supervision of Hung-Yu Yang and Fazel Tafti.

and MR_{edge} should vanish and no negative longitudinal MR would be observed. Nevertheless, what we observed is something else. The first measurement with point contacts shows a typical behavior of current jetting (Fig. 2.5); positive MR_{spine} , and negative MR_{edge} . For the second measurement with area contacts, MR_{spine} becomes less positive, and MR_{edge} becomes less negative, so the effect of current jetting is indeed weakened, but not anywhere close to annihilation. In the reports of negative longitudinal MR in WSMS, it is often argued that as long as area contacts are applied to the current leads, current would flow uniformly and the effect of current jetting may be ruled out. The simple experiment shown in Fig. 2.5 and other literature [87] disproves this idea, which may be the most popular misconception in this research area.

In a squeeze test, since the current distribution is well controlled by the point contacts (there is no other place the current can flow in), the spine and edge channels individually represents the most positive and most negative signal that

can possibly be contributed by current jetting. Therefore, it is a very useful tool to quantify how much a particular sample suffers from current jetting. In addition, if a material passes the squeeze test, there must be an *intrinsic* negative longitudinal MR in this material, and it can serve as a solid evidence of chiral anomaly if other intrinsic mechanisms are ruled out. In the context of negative longitudinal MR, squeeze test can provide valuable information and should always be implemented whenever possible.

2.3 First-principles Calculations and Extended Applications

Experimental data do not teach us new physics without a proper interpretation, and theoretical calculations are always welcome in helping us understand the physics in a certain material. First-principles calculations via density functional theory (DFT) [88, 89] offer a unique access to band structures which often govern the electronic properties of materials. As more and more DFT codes are developed and made user friendly, some experimental groups have started to perform DFT calculations themselves. Apart from giving explanations after an experiment is done, DFT calculations also help us choose promising target materials before an experiment is conducted so that we may distribute our limited time and resources efficiently. In this dissertation, I use the WIEN2k code [90] to perform DFT calculations, while collaborations with DFT experts are also sought and lead to fruitful results. Below, from an experimentalist's point of view, I will briefly describe some general considerations of DFT calculations. Also, some methods used to tackle correlations, which are the key to a lot of interesting physics but hard to deal with, are discussed.

To calculate energies of bands of a certain material within a reasonable amount

of time, a 3D grid in k-space and finite basis sets are chosen. If the grid gets denser, more k-points are sampled to enhance the accuracy, but it takes more time to finish the calculations. Similarly, if bigger basis sets are chosen, we can model the wave functions better, but will need more time to deal with a larger matrix. As a result, there is always a trade-off between accuracy and feasibility; a reasonably dense grid and large basis sets are required to give a proper description of the system, while the calculation becomes unmanageable if the grid is too dense and the basis size is too large. These two parameters are controlled by the number of k-points and “RKmax” in WIEN2k, and they need to be taken care of in other DFT packages as well no matter it adopts a full-potential or a pseudopotential method. In practice, These two parameters should always be tested as the first step of the calculation before other complications such as SOC or U is implemented. Reasonable choices of k-points and RKmax are usually determined when the quantities of interest stop changing with higher k-points and RKmax, and we can use this set of parameters for more in-depth calculations.

2.3.1 Handling Correlations

The difficulty of getting the calculation under control increases as the system gets more and more complicated (and more interesting), especially when strong correlations are present. To treat the exchange-correlation energy, local density approximation (LDA) [89] and Perdew-Burke-Ernzerhof (PBE) energy functional based on generalized gradient approximation (GGA) [91] are widely used and have achieved a huge success. However, there are occasions where these two methods fail to give satisfactory descriptions of some key properties, such as band gaps in semiconductor/insulator [92, 93] or sizes of Fermi surfaces [53]. For our purposes, two ways of handling correlations are briefly introduced below.

- +U method [94–98]: For d-electron and f-electron systems, because the lo-

calized nature of electrons in d and f orbitals, they feel strong Coulomb interactions which are not sufficiently accounted for by LDA or PBE. To solve this problem, an on-site Hubbard U term is added to these localized orbitals. In this way, the strong correlations are included, but now we have a tuning parameter in a first-principle calculation. Typically, a proper U may be chosen by comparing DFT results and experiments. For example, for a certain insulator or semiconductor, the U may be determined when the calculation returns the band gap measured by the experiment. For an f-electron metal, the U may be chosen by pushing the flat f bands away from E_F until it does not move further. In the above cases, the resultant U is usually large (> 5 eV). For a semimetal, the Fermi surface may be quite sensitive and can be completely eliminated if U is too large, and a moderate U may be selected by fitting the sizes of Fermi pockets calculated by DFT to quantum oscillation (QO) experiments [53, 99] (see also Sec. 2.3.2). Although the +U method is often criticized by the fact that the results can be tuned by changing U , such calculations serve as computationally cheap solutions and provide valuable insights.

- Modified Becke-Johnson (mBJ) exchange-correlation potential [92, 93]: mBJ potential aims to provide a better description of the exchange-correlation energy globally, not just locally on a specific orbital of an atom in a material. In principle, mBJ potential can also be tuned, but it has been optimized by fitting the band gaps of a list of materials [92]; it turns out that the optimized mBJ potential is able to suitably describe lots of materials, in strong contrast to the +U method which requires different U 's for different materials. As a computationally cheap method, it is surprising that it can give accurate results comparable to the more expensive method like GW or hybrid functional. It has been shown that mBJ functional can describe insu-

lators and semiconductors very decently; it may be suitable for semimetals, but extra care needs to be taken [53].

2.3.2 Supercell K-space Extremal Area Finder (SKEAF)

The band structures calculated by DFT should always be treated with care because of inevitable approximations used in the calculations. To make sure the calculated band structures correctly describe the material of interest, a confirmation from experiments is needed. One of such experiments capable of probing band structures is to measure QOs, which detect the extremal areas of closed Fermi pockets in a material via oscillations in electrical resistance, magnetic torque, etc. (see Sec. 2.4.3). Therefore, the DFT results can be substantiated if the extremal areas calculated from the band structures by DFT match the ones obtained from QO experiments. Supercell k-space extremal area finder (SKEAF), a code developed by Patrick Rourke *et al.* [100], is for this purpose. SKEAF processes the so-called “bxsf” files, which store the energies of all bands calculated by DFT on a 3D grid in k-space². From these files, SKEAF identifies the bands crossing the E_F , and calculates band characters (electron or hole), extremal areas, effective masses, and coordinates in k-space for all Fermi pockets.

The basic idea of SKEAF is explained as follows. Based on the input bxsf files, the program generates a supercell comprising many replicas of Fermi pockets in the material of interest. A magnetic field with its direction consistent with the experiment is assumed. All replicas of Fermi pockets are cut into slices normal to the field direction, and their areas are calculated. For each pocket, the slice of extremal (either minimum or maximum) area is singled out and converted to oscillation frequency through the Onsager relation. Besides, its character, effective mass, and coordinate are calculated. The results are then compared with the QO

²See here for more information: <http://www.xcrysden.org/doc/XSF.html>.

experiment; if they agree with each other, the DFT calculation can be argued to be accurate and gives a proper description of the material.

Like all the other calculations, the results of SKEAF need to be checked with care before they may be compared with the experimental results. Firstly, for a certain extremal area identified by SKEAF, there should at least be tens of or even hundreds of copies found, because the calculation is done on a supercell and a pocket should repeat itself in the supercell for many times. If an extremal area is only found several times (< 10) by SKEAF, most likely it is a fluke and can be removed from the final results. Secondly, to further confirm the presence of a certain extremal area, it is favorable to look into its reciprocal unit cell (RUC) coordinates and try to visualize it. Fig. 2.6 shows the Fermi surface of a band of NbGe₂ as an example, and the green dot marks the average RUC coordinates of an extremal area found only several times in the supercell created by SKEAF. The rare occurrence of this area is already a sign that it is spurious, while this conjecture is confirmed by the position of the green dot; it does not seem to sit in the middle of any closed orbit. As a result, in this case, this orbit may be safely removed. Whenever possible, it is always a good idea to check the RUC coordinates of the extremal areas found by SKEAF, and try to understand their shapes and positions in the Brillouin zone.

2.4 Model Analysis

2.4.1 Semiclassical Multiband Model

For systems perturbed by a weak external field, the semiclassical Boltzmann transport equation [83] provides general descriptions of the resultant responses. Under a finite magnetic field \mathbf{B} , the charge carriers respond to an electrical current I through resistivity tensor, the expressions of which are given by Boltzmann

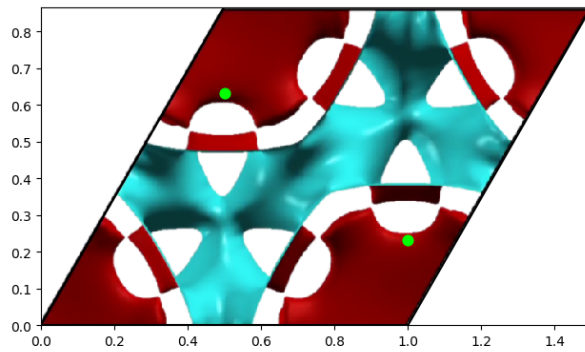


Figure 2.6: Spurious orbit revealed by its RUC coordinates. The brown and cyan surfaces show the exterior and interior of the Fermi surface of a band in NbGe_2 . The boundaries are normalized to one by the reciprocal lattice vectors. The green dot marks the center of a spurious orbit identified by SKEAF, which does not correspond to any closed orbit once visualized. The figure is reproduced in courtesy of Xiaohan Yao.

equation³:

$$\rho_{xx} = \frac{\sum_i^N \frac{\sigma_i}{1+\mu_i^2 B^2}}{\left(\sum_i^N \frac{\sigma_i}{1+\mu_i^2 B^2}\right)^2 + \left(\sum_i^N \frac{\sigma_i \mu_i}{1+\mu_i^2 B^2}\right)^2} B^2 \quad (2.17)$$

$$R_H = \rho_{yx}/B = \frac{\left(\sum_i^N \frac{\sigma_i \mu_i}{1+\mu_i^2 B^2}\right)}{\left(\sum_i^N \frac{\sigma_i}{1+\mu_i^2 B^2}\right)^2 + \left(\sum_i^N \frac{\sigma_i \mu_i}{1+\mu_i^2 B^2}\right)^2} B^2, \quad (2.18)$$

where N is the total number of bands in the system, i is the band index, μ_i is the mobility of the i -th band, $\sigma_i = n_i e_i \mu_i$ is the conductivity, e_i is of the magnitude of the elementary charge e , n_i is the carrier concentration. Here, the sign convention of the Hall coefficient R_H is positive for hole carriers, e_i is positive for holes and negative for electrons, and $\mu_i = |e_i| \tau_i / m_i^*$ (τ_i is the relaxation time and m_i^* is the effective mass) is always positive. By measuring both ρ_{xx} and ρ_{yx} and fit to the expressions Eq. 2.17 and 2.18 simultaneously, we may get information of carrier concentration and mobility of each band. As for how many electron and hole bands should be present in Eqs. 2.17 and 2.18, we may look into band structures calculated by DFT and identify distinct Fermi pockets crossing E_F , each of which represents a band in the multiband model. Nevertheless, if a material consists of many pockets, it may not be feasible to put all the bands in the model. There will be many parameters and the fit could give ambiguous results sensitive to initial conditions. In this case, simply assuming the material is described by a general electron band and a general hole band may provide more useful information.

Two illuminating special cases are discussed below:

- One-band system: Let us consider a system that has only one electron band.

³Here I referred to ρ_{xx} and ρ_{yx} to give a specific example, but Eqs. 2.17 and 2.18 apply to other components of the resistivity tensor as well.

Eq. 2.17 reduces to:

$$\begin{aligned}
\rho_{xx} &= \frac{\frac{\sigma_1}{1+\mu_1^2 B^2}}{\left(\frac{\sigma_1}{1+\mu_1^2 B^2}\right)^2 + \left(\frac{\sigma_1 \mu_1}{1+\mu_1^2 B^2}\right)^2 B^2} \\
&= \frac{1}{\sigma_1} \frac{1}{\left(\frac{1+\mu_1^2 B^2}{1+\mu_1^2 B^2}\right)} \\
&= \frac{1}{\sigma_1}.
\end{aligned} \tag{2.19}$$

That is, the MR of a one-band system is zero. On the other hand, Eq. 2.18 reduces to:

$$\begin{aligned}
R_H = \rho_{yx}/B &= \frac{\left(\frac{\sigma_1 \mu_1}{1+\mu_1^2 B^2}\right)}{\left(\frac{\sigma_1}{1+\mu_1^2 B^2}\right)^2 + \left(\frac{\sigma_1 \mu_1}{1+\mu_1^2 B^2}\right)^2 B^2} \\
&= \frac{\mu_1}{\sigma_1} = \frac{1}{n_1 e_1}.
\end{aligned} \tag{2.20}$$

The Hall coefficient is determined by the carrier concentration and the sign depends on the type of carrier e_1 .

- Two-band system: Let us consider a two-band system with the bands labelled as 1 and 2. In such a case, R_H and MR can be derived from Eqs. 2.17 and 2.18: [83, 101]

$$\begin{aligned}
\text{MR} &= \frac{\rho_{xx}(B) - \rho_{xx}(0)}{\rho_{xx}(0)} \\
&= \frac{\sigma_1 \sigma_2 (\text{sgn}(e_1) \mu_1 - \text{sgn}(e_2) \mu_2)^2 B^2}{(\sigma_1 + \sigma_2)^2 + (\sigma_1 \mu_2 + \sigma_2 \mu_1)^2 B^2}
\end{aligned} \tag{2.21}$$

$$R_H = \frac{\sigma_1 \mu_1 (1 + \mu_2^2 B^2) + \sigma_2 \mu_2 (1 + \mu_1^2 B^2)}{(\sigma_1 + \sigma_2)^2 + (\sigma_1 \mu_2 + \sigma_2 \mu_1)^2 B^2}, \tag{2.22}$$

where $\rho_{xx}(0) = 1/\sigma_1 + 1/\sigma_2$. It is interesting to see the behavior of a two-system that has compensated electrons and holes; if we let $e_1 = +e$, $e_2 = -e$,

and $n_1 = n_2 = n$, Eqs. 2.21 and 2.22 can be simplified to

$$\text{MR} = \mu_1 \mu_2 B^2 \quad (2.23)$$

$$R_H = \frac{1}{ne} \frac{\mu_1 - \mu_2}{\mu_1 + \mu_2}. \quad (2.24)$$

Eqs. 2.23 and 2.24 show several interesting general features for electron-hole compensated systems. Firstly, MR is non-saturating and follows a quadratic field dependence, in sharp contrast to the one-band case. Secondly, the sign of R_H now reflects the relative strengths of mobilities of electron and hole bands, rather than the type of carrier directly as in the one-band system (Eq. 2.20). Typically, the sign of R_H is viewed as an indication of the dominant carrier in the system; for example, a positive R_H usually means there are more holes than electrons in a system. However, an alternative interpretation is revealed by Eq. 2.24, where a finite Hall effect could mean a system of equal amount of electrons and holes while one carrier is more mobile than the other. To choose between these two interpretations, we may examine MR since a two-band system of different carrier concentrations often show a saturation in its MR. This observation shows the importance of looking into MR and R_H together to get the comprehensive picture.

2.4.2 Tian-Ye-Jin Scaling of Anomalous Hall Effect

Discovered more than a hundred years ago, AHE recently regains much attention in the study of topological semimetals; topological nodes in these materials serve as sources and drains of intrinsic Berry curvature, potentially giving rise to a gigantic AHC [33]. However, the intrinsic contribution to AHE is often mixed with the extrinsic ones by side-jump [64] and skew scattering [63], and is difficult to extract. To tackle this problem, Tian, Ye, and Jin proposed an empirical scal-

ing relation that aims to reliably extract the intrinsic contribution to AHE [102]. The scaling relation was later justified by separate theoretical works [103, 104] and has achieved success in explaining intrinsic AHE in several magnetic topological semimetals [70, 77, 78, 105]. Below, I will briefly introduce the basic idea of the scaling relation, and discuss its limitation and application in FM WSMs.

In general, considering skew scattering ($\propto \rho_{xx}$, characterized by α) [63], side-jump ($\propto \rho_{xx}^2$, characterized by β) [64], and Berry curvature ($\propto \rho_{xx}^2$, characterized by b) [62] contributions, we may write the anomalous part of the Hall resistivity ρ_{xy}^A as

$$\rho_{xy}^A = \alpha\rho_{xx} + \beta\rho_{xx}^2 + b\rho_{xx}^2, \quad (2.25)$$

In contrast to this general form, Tian *et al.* proposed the following empirical scaling law:

$$\rho_{xy}^A = \alpha\rho_{xx0} + \beta\rho_{xx0}^2 + b\rho_{xx}^2, \quad (2.26)$$

where ρ_{xx0} stands for the residual value of ρ_{xx} at 0 K. This expression presumably excludes the phonon contributions of both extrinsic mechanisms. Next, assuming $\rho_{xy}^A \ll \rho_{xx}$, we note that AHC can be written as $\sigma_{xy}^A \sim -\rho_{xy}^A/\rho_{xx}^2$, and we may invert Eq. 2.26 to get the scaling relation for AHC by multiplying both sides with $1/\rho_{xx}^2$:

$$\sigma_{xy}^A = -(\alpha\sigma_{xx0}^{-1} + \beta\sigma_{xx0}^{-2})\sigma_{xx}^2 - b, \quad (2.27)$$

where $\sigma_{xx0} = 1/\rho_{xx0}$. Eq. 2.27 reveals a convenient way to derive the intrinsic contribution b ; by plotting σ_{xy}^A against σ_{xx}^2 and fitting the data to Eq. 2.27, one can extract the parameter b from the y-intercept of the fitting line, which simply represents the intrinsic Berry curvature contribution to AHC. Tian *et al.* demonstrated such a scaling by plotting σ_{xy}^A vs. σ_{xx}^2 in Fig. 4(b) of Ref. [102], where the data taken from Fe thin films of different thickness are fitted to Eq. 2.27. Interestingly, the data of each thickness do scale linearly according to Eq.

2.27. Besides, all of the fitting lines extrapolate to the same y-intercept and give the same magnitude of intrinsic AHC. The universal convergence of fitting lines suggests a robust intrinsic AHC shared by all Fe thin films regardless of their thickness and extrinsic parts of AHC being different. The extracted AHC was compared to the value calculated by DFT [68, 106] and shows a decent agreement.

Despite the success of Eq. 2.27 demonstrated in Ref. [102], the scaling relation needs to be used with care. In a follow-up study [104] of Ref. [102], the authors revisited Eq. 2.27 with Fe thin films of much higher conductivity used in the previous study [102], and found that the scaling relation breaks down in samples of higher conductivity. Furthermore, a general scaling relation is derived as follows:

$$\sigma_{xy}^A = -[\alpha\sigma_{xx0}^{-1} + (\beta_0 - \beta_1)\sigma_{xx0}^{-2}]\sigma_{xx}^2 - \beta_1 - (\gamma - 2\beta_1)(\sigma_{xx0}^{-1}\sigma_{xx} - \sigma_{xx0}^{-2}\sigma_{xx}^2), \quad (2.28)$$

where β_0 , β_1 , and γ are contributed by different scattering terms, and b in Eq. 2.27 is now embedded in β_1 . By comparing Eq. 2.27 and Eq. 2.28, we may find that 1) the linear scaling relation between σ_{xy}^A and σ_{xx}^2 breaks down if the last term in Eq. 2.28 becomes significant, and 2) even if the last term may be ignored, the y-intercept of σ_{xy}^A vs. σ_{xx}^2 plot now gives β_1 , which consists of not only the intrinsic contribution to AHC (b), but also the extrinsic side-jump contribution [104]. As a result, without a proper understanding of the side-jump contribution, it may be difficult to quantitatively argue the AHC contributed by intrinsic Berry curvature in a material, especially in materials of high conductivity.

The dependence of scaling relation on the longitudinal conductivity σ_{xx} was also discussed in previous works [107, 108]. It was pointed out that as σ_{xx} increases, three different regimes can be identified: dirty ($\sigma_{xx} \lesssim 10^4 \Omega^{-1}\text{cm}^{-1}$), intermediate ($10^4 \Omega^{-1}\text{cm}^{-1} \lesssim \sigma_{xx} \lesssim 10^6 \Omega^{-1}\text{cm}^{-1}$), and clean regimes ($10^6 \Omega^{-1}\text{cm}^{-1} \lesssim \sigma_{xx}$), and the intermediate and clean regimes are argued to be dominated by intrinsic

Berry curvature and extrinsic skew scattering, respectively [107]. This work may partly explain why Eq. 2.27 works for quite a few topological semimetals [70, 77, 78, 105] and Fe films grown on GaAs substrate [102], the conductivity of which does fall in the intermediate regime. However, the crossover between different regimes makes it difficult to argue that, if the value of σ_{xx} alone is enough to tell the AHE of a material is dominated by intrinsic mechanism. To better understand AHE and differentiate contributions from different mechanism, the calculations and developments of extrinsic AHE are highly desired [106].

2.4.3 Quantum Oscillation (QO)

The term QO represents oscillatory phenomena originated from Landau quantization, which happens when a magnetic field is applied and all electronic states collapse into discrete Landau levels [109]. In principle, QOs can be observed in metals via ultrasonic attenuation, magnetic susceptibility (de Haas-van Alphen effect), and electrical resistivity (Shubnikov-de Haas effect), etc. Particularly, the frequencies of these oscillations provide important information about the Fermi surface geometry of a material through the Onsager relation [110]:

$$F = \frac{\hbar}{2\pi e} A_{ext}, \quad (2.29)$$

where F is the oscillation frequency, A_{ext} is the extremal area of a closed Fermi surface (sometimes called a Fermi pocket) normal to the field direction. By changing the direction of the applied field, we can map out different extremal areas and get the angular dependence of observed frequencies, from which the Fermi surface geometry can be inferred (see also Sec. 2.4.4).

Apart from the geometry, the effective mass m^* of a Fermi surface can also be extracted by observing the peaks in the oscillatory profile and fitting them to the

Lifshitz-Kosevich formula [82, 111–113]:

$$R_L = \frac{X}{\sinh(X)}, \quad X = \frac{\alpha T m^*}{H} \quad (2.30)$$

where R_L is the damping factor and $\alpha = 2\pi^2 k_B m_e / e\hbar$ is a constant comprised of Boltzmann factor k_B , bare electron mass m_e , electron charge e , and reduced Planck constant \hbar . The effective mass m^* in Eq. 2.30 is calculated in units of m_e .

In practice, more than one Fermi pocket may exist in the band structure of a material, and produce multiple frequencies (and potentially their harmonics) in QO experiments. In this situation, the oscillatory profile can be fairly complicated and difficult to interpret. A great tool to analyze complicated patterns is Fourier transform (FT), which turns them into frequency spectra and reveal the frequencies corresponding to different Fermi pockets as peaks in the spectra. Therefore, Eq. 2.30 is often fitted to the peak FT amplitudes of a certain frequency as a function of temperature (as an approximation, H is replaced by \bar{H} , the average of the FT window), rather than to peaks in the oscillatory profile at a certain field. Either way, the effective mass m^* can be derived from the fitting coefficient. To make sure the analyses of F and m^* are reliable, we may try to reconstruct the original oscillatory profile by adding another damping factor (the Dingle term) [113]. The reconstruction not only gives us information about transport lifetime through the Dingle temperature, but also gives credibility of frequencies and effective masses identified via FT.

Recently, QO has gained new attention in the study of topological materials because it can detect non-trivial Berry phase [114]. Despite the success detection of Berry phase in QOs in graphene [115], its confirmation in topological insulators and semimetals is still challenging [18, 116]. In particular, the fact that trivial bands and non-trivial bands need to be treated differently [117], the effect of

spin damping factor [118], and potential corrections to the integer Berry phase in topological materials [119, 120], are sometimes overlooked. Experimentally, there are also technical issues to acquire a consistent phase for a material and the phase extrapolated from its Landau fan diagram may vary when the fitting range is changed [121]. Despite these complications, QO experiment remains one of the most powerful tools for studying topological materials, with questions to be answered by further investigations.

2.4.4 E_F Determination by SKEAF and QO

In a DFT calculation of a material, electrons are filled up to the neutrality point, which determines the Fermi level E_F (E_F^{DFT}). Ideally, we expect the E_F in every sample of this material to be E_F^{DFT} ; however, due to a potential inclusion of impurities and vacancies, a sample may be slightly doped and its E_F may deviate from E_F^{DFT} accordingly. One immediate consequence of different E_F is different Hall effect; by measuring Hall resistivity, say $\rho_{yx}(H)$, of different samples, the curves may not fall on top of each other and may show very different field dependence [78, 122]. In particular, semimetals are susceptible to the shift of E_F because of their small density of states (DOS). In the context of WSMs, exotic transport phenomena such as chiral anomaly and AHE are usually sensitive to the energies of Weyl nodes relative to E_F in a WSM [28, 33]. Thus, A WSM with tunable E_F provides a unique platform to study topological transport properties by looking into samples of different E_F [78].

To determine E_F of different samples, $\rho_{yx}(H)$ alone may not be adequate in some cases. For a simple one-band system, we may extract the carrier concentration of the band from $\rho_{yx}(H)$ (see Sec. 2.4.1), and compare it to a DFT calculation. E_F is tuned in the band structure calculated by DFT until the resultant carrier concentration of the band matches the experimental one, and the E_F is settled

at this point. A similar procedure may be pursued for a two-band system with one electron pocket and one hole pocket, but it becomes difficult to get the fitting process under control. For example, a large Hall effect could mean that the carrier concentrations of the electron and hole band are drastically different, or their concentrations are actually the same and it is their mobilities that are different (see Sec. 2.4.1). As the number of bands grows, the fitting parameters in a multiband model increase, and it is likely to get a decent fit to the data with two sets of parameters very different from each other. Besides, a typical multiband model assumes a spherical geometry for each Fermi pocket, so the results may not be reliable if the pockets have funky shapes like bananas [86], stars [53], etc. In topological semimetals, since the Fermi surface usually contains many pockets of non-spherical shapes, an alternative way to determine E_F of different samples is desired.

In this dissertation, a combination of SKEAF and QO experiments is used to determine E_F of different samples [78, 123]. First of all, for the material of interest, several samples are characterized and the Hall effect ($\rho_{yx}(H)$) is measured. If $\rho_{yx}(H)$ shows a sample dependence, which is a sign of a shift of E_F among different samples, several representative samples of different $\rho_{yx}(H)$ will be selected for QO experiments. QOs of each representative sample are measured and analyzed to extract oscillation frequencies (F_{QO}) corresponding to different Fermi pockets in the system. Then, we perform a DFT calculation, from which SKEAF can calculate all the oscillation frequencies (F_{DFT}) that may possibly be detected in QO experiments. The frequencies F_{DFT} calculated by SKEAF change as we manually put E_F away from E_F^{DFT} in a SKEAF calculation, and the true E_F , at which the calculated frequencies F_{DFT} match with F_{QO} measured from a particular sample, is determined to be the correct E_F of that sample.

Since an oscillation frequency must correspond to an extremal area of a real

Fermi pocket, the information given by QOs is more specific and robust than a multiband fit. As mentioned earlier, by changing the initial conditions or constraints slightly, a multiband fit could return different sets of parameters, all of which describe the material decently while give very different interpretations of carrier concentrations and mobilities of the system. Occasionally, the QO method may have some limitations. If the applied magnetic field is not high enough for the material to reach its quantum limit, it may fail to show observable QOs for all Fermi pockets of the material. In such cases, we may not resolve all the frequencies that could appear in principle, and need to determine E_F with limited information from the observed frequencies. The E_F determination process described previously can still be done, but additional considerations may be needed.

Let us consider a material, where a DFT calculation shows that there should be five observable oscillation frequencies (labelled as F_1 to F_5), while in a QO experiment only two frequencies are observed. It is possible that these two frequencies match with F_1 and F_3 when the Fermi level is set to be at some value $E_F^{(1)}$ in the calculation, but at some other Fermi level $E_F^{(2)}$, the frequencies F_1 to F_5 change accordingly and now the experimental frequencies match with F_4 and F_5 . Now that both $E_F^{(1)}$ and $E_F^{(2)}$ can explain the QO experiment, which Fermi level shall we adopt? One solution may come from the measurement of Hall effect. For example, if the Hall effect suggests that the dominant carrier type is electron, and $E_F^{(1)}$ results in a Fermi surface dominated by electrons (the Fermi volume is largely composed by electron pockets), while $E_F^{(2)}$ has a hole-dominant Fermi surface, we may argue $E_F^{(1)}$ to be the more reasonable choice of Fermi level for this material.

For the purpose of studying the E_F dependence of some topological properties, QO experiments have another edge: QO can be measured on exactly the same pieces from which the transport properties are measured, without destroying them. Other techniques used to detect band structures, such as angle resolved

photoemission spectroscopy (ARPES) or scanning tunneling microscopy (STM), usually involve a cleaving process, which basically cuts off part of the sample to get a clean surface for measurements. However, the cleaved sample is not guaranteed to have the same E_F as the original one, so a proper E_F dependence can not be obtained. On the other hand, if the property of interest depends on E_F and has a proposed theoretical expression that can be fitted to the data, it might be possible to determine E_F from such a fit. This method should be avoided, though, before it is made clear that the experimental signal is governed by the proposed theory. If the experimental signal is elusive and heavily affected by other effects, E_F determined by such a fit may not be reliable [31, 86]. In short, E_F determination by SKEAF and QO provides valuable information for the study of E_F dependence of various physical phenomena.

CHAPTER III

Rare-Earth Monopnictides

3.1 LaAs: In Search of the Origin of XMR

The family of binary Lanthanum monopnictides, LaBi and LaSb, have attracted a great deal of attention as they display an unusual extreme magnetoresistance (XMR) that is not well understood. Two classes of explanations have been raised for this: the presence of non-trivial topology, and the compensation between electron and hole densities. Here, by synthesizing a new member of the family, LaAs, and performing transport measurements, angle resolved photoemission spectroscopy (ARPES), and density functional theory (DFT) calculations, we show that (a) LaAs retains all qualitative features characteristic of the XMR effect but with a significant reduction in magnitude compared to LaSb and LaBi, (b) the absence of a band inversion or a Dirac cone in LaAs indicates that topology is insignificant to XMR, (c) the equal number of electron and hole carriers indicates that compensation is necessary for XMR but does not explain its magnitude, and (d) the ratio of electron and hole mobilities is much different in LaAs compared to LaSb and LaBi. We argue that the compensation is responsible for the XMR profile and the mobility mismatch constrains the magnitude of XMR.

3.1.1 Introduction

Semimetals are characterized by small and often compensated electron and hole carrier densities ($n_e/n_h \approx 1$) [124]. In elemental semimetals, such as bismuth, compensation between high mobility electron and hole carriers reduces the Hall field and produces a large magnetoresistance $\text{MR}(\%) = 100 \times [\rho(H) - \rho(0)] / \rho(0)$ [125–129]. A reduced Hall field fails to counteract the Lorentz force that bends the trajectory of charge carriers in a magnetic field, therefore results in a large MR [124].

An extremely large and non-saturating MR with magnitude $\sim 10^{4-6}\%$ has been recently reported in several topological semimetals including WTe_2 [46, 130], Cd_3As_2 [25], PtSn_4 [131, 132], NbSb_2 [41], NbAs [44], NbAs_2 [133], NbP [134], TaSb_2 [42], TaAs [135], TaAs_2 [133, 136], and TaP [137]. Topological semimetals are extensions of topological insulators where degenerate crossings between several bulk bands are protected by a fundamental symmetry of the material [138]. The $\rho(T)$ profile of the XMR in topological semimetals looks similar to the $\rho(T)$ profile of topological insulators where by decreasing temperature, resistivity shows an *upturn* followed by a *plateau* [139, 140]. In topological insulators, the upturn is assigned to a metal-insulator transition and the plateau is assigned to topological surface states. The similarity between the XMR profile and the profile of topological insulators caused confusion and opened a debate over the possibility of XMR profile being rooted in the topological properties of topological semimetals [25, 46, 134, 137]. Here, we try to settle this debate by making a new material which is topologically trivial but shows the typical XMR profile.

Lanthanum mononictides (LaSb and LaBi) [26, 27, 39, 40] have attracted special attention among XMR semimetals due to their simple cubic structure [27]. It has been shown that both LaSb and LaBi are compensated [39, 51] but Dirac cones have also been observed clearly in LaBi [47–50] and less clearly in LaSb [47,

51, 52] by ARPES. Therefore, it is challenging to disentangle compensation from topology in relation to XMR by focusing on LaSb and LaBi. The disagreement on the presence of Dirac cones in LaSb from ARPES results suggests a topological transition within the lanthanum monpnictide family by decreasing the pnictogen size. This observation motivated us to grow single crystals of LaAs with the hope of observing XMR in the absence of topological features.

Our detailed transport measurements, DFT calculations, and ARPES experiments reveal two important findings: First, LaAs lacks a Dirac cone unambiguously, yet it exhibits the typical XMR transport profile. Therefore, XMR is independent of topological character. Second, LaAs is as compensated as LaSb and LaBi, but the magnitude of XMR in LaAs is orders of magnitude smaller. Therefore, compensation is necessary to explain the presence of XMR but not sufficient to determine its magnitude. Our results suggest that the relative mobilities of electrons and holes determine the magnitude of XMR in compensated semimetals.

Previous reports on the synthesis of LaAs are limited to polycrystalline samples [141, 142], thin films [143], or mixed phases of LaAs₂/LaAs [144]. This is the first comprehensive report on the growth and characterization of pure LaAs single crystals.

3.1.2 Methods

Crystal growth and characterization— LaAs crystals were grown using a flux method. The constituent elements with the mole ratio La:As:Sb = 1:1:20 were placed in an alumina crucible, sealed in an evacuated quartz tube, and transferred to a muffle furnace. The mixture was heated at 3 °C/min to 1000 °C, kept at that temperature for 72 h, then slowly cooled to 850 °C at 0.1 °C/min, annealed for 24 h, and finally centrifuged to decant the Sb flux. The 1:1 composition of LaAs was confirmed by EDX spectroscopy using a JOEL field emission electron microscope

quipped with an EDAX detector. Powder XRD was performed using a Bruker D8 ECO instrument. FullProf suite was used for the Rietveld refinement¹ of the Powder XRD data [75].

Resistivity measurements– Resistivity and the Hall effect were measured with a standard four probe technique in a Quantum Design Dynacool in both positive and negative field directions. The data were symmetrized for transverse magnetoresistance (MR) and anti-symmetrized for the Hall effect.

Calculations– DFT calculations with full-potential linearized augmented plane-wave (LAPW) method were implemented in the WIEN2k code [90] with the basis-size controlling parameter $RK_{\max} = 8.5$ and 10000 k-points. Both the Perdew-Burke-Ernzerhof (PBE) [91] and the modified Becke-Johnson (mBJ) exchange-correlation potentials [92] were used in the calculations with spin-orbit coupling (SOC).

*ARPES experiments*²– ARPES measurements were performed at the high resolution branch of the i-05 beamline at Diamond Light Source. Single crystals of LaAs were cleaved in an ultrahigh vacuum environment of 10^{-10} torr and measured at both 7 K and 220 K. A Scienta R4000 electron analyzer was used with total energy and angular resolutions of 10 meV and 0.3° .

3.1.3 Magnetoresistance and Hall Effect

Fig. 3.1(a) shows the face-centered cubic (fcc) structure of LaAs. The high quality of crystals is confirmed by the absence of impurity phases in the x-ray pattern and the low χ^2 in the Rietveld refinement. Fig. 3.1(b) shows $\rho(T)$ in LaAs measured at different magnetic fields. At $B = 9$ T, with decreasing temperature, $\rho(T)$ decreases initially, then shows a minimum followed by an upturn, and eventually plateaus. With decreasing magnetic field, the resistivity upturn

¹The Rietveld refinement was performed by S. Jaszewski [53].

²ARPES experiments were conducted by T. Nummy, H. Li, and D. S. Dessau [53].

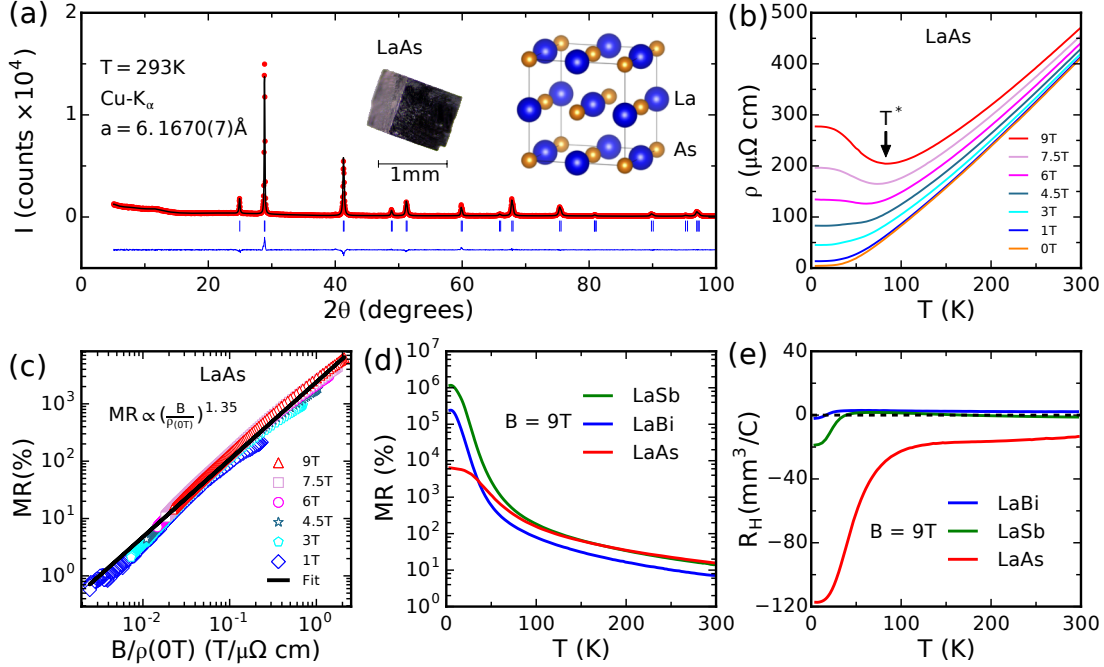


Figure 3.1: X-ray diffraction, magnetoresistance, and Hall effect of LaAs. (a) Rietveld refinement on the powder x-ray data from LaAs in the space group $Fm\bar{3}m$ with $R_{wp} = 7.71$, $R_{exp} = 6.05$, and $\chi^2 = 1.63$. Inset shows a picture of the single crystal and a drawing of the LaAs unit cell. (b) Resistivity as a function of temperature at different fields in LaAs. (c) Kohler scaling analysis on the resistivity data. (d) Magnetoresistance as a function of temperature in LaAs, LaSb, and LaBi on a logarithmic scale. (e) Hall coefficient as a function of temperature in LaAs, LaSb, and LaBi.

gradually disappears. Such behavior is a generic XMR profile [26, 46]. The resistivity minimum at fields above 5 T in Fig. 3.1(b) can be understood by comparing the energy scale of cyclotron frequency $\hbar\omega_c = \hbar eB/m^*$ to the thermal energy $k_B T$. As shown later, from quantum oscillations, the average effective mass on the small Fermi surfaces of LaAs is $m^* \approx 0.15 m_e$. Therefore, MR appears below $T^* = \hbar eB/m^* k_B \approx 80$ K (at $B = 9$ T).

If cyclotron motion is the main source of resistivity upturn, MR at all temperatures and fields must follow the Kohler's scaling rule:

$$\text{MR}(\%) = \frac{\rho(T, B) - \rho(T, 0)}{\rho(T, 0)} \times 100 \propto \left(\frac{B}{\rho(T, 0)} \right)^\nu \quad (3.1)$$

Fig. 3.1(c) shows the Kohler's law is obeyed in LaAs, ruling out a field-induced metal-insulator transition or a temperature-induced Lifshitz transition [145, 146]. The presence of an XMR profile in the absence of a Lifshitz transition in LaAs is similar to LaSb [51] and LaBi [40]. However, XMR is orders of magnitude smaller in LaAs compared to LaSb and LaBi as shown in Fig. 3.1(d). It is shown in prior work [26] that the XMR magnitude correlates with the residual resistivity ratio (RRR). Figure A.1 in Appendix A.1 compares a LaAs and a LaBi crystal with similar RRR where the XMR is an order of magnitude smaller in LaAs. At $B = 9$ T, the low temperature resistivity is smaller than the room temperature resistivity $\rho(2\text{K}) < \rho(300\text{K})$ in LaAs whereas $\rho(2\text{K}) > \rho(300\text{K})$ in LaBi/LaSb (see Fig. A.1). Since the large magnitude of XMR in LaSb and LaBi is attributed to perfect compensation between electrons and holes [39, 51], we measured the Hall effect to examine the compensation in LaAs. Fig. 3.1(e) shows the Hall coefficient (R_H) in LaAs acquires a much larger negative magnitude without sign change, different from LaSb and LaBi. At first glance, this may suggest that LaAs is not compensated. However, our detailed analyses below show that LaAs

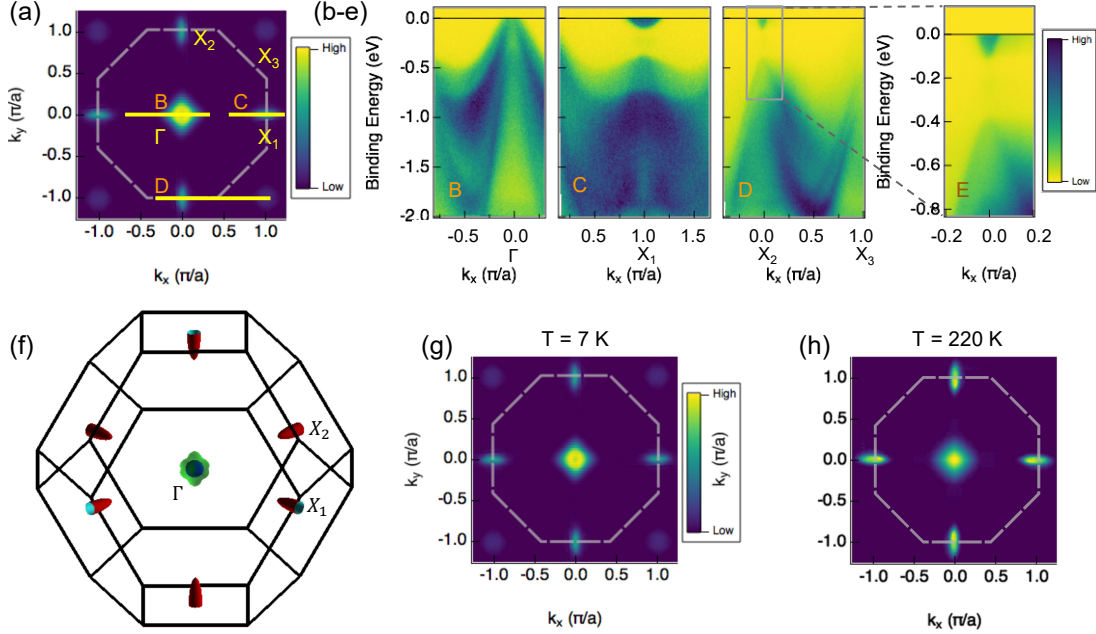


Figure 3.2: Results of the ARPES experiment conducted on a LaAs single crystal. (a) Constant energy surfaces of LaAs taken at E_F in the $k_x - k_y$ plane. The dashed overlay is the first Brillouin zone, the solid lines indicate the respective locations of the dispersion cuts in (B),(C), and (D). Cross-sections of the ellipsoidal electron pockets (α) are visible at X_1, X_2 , and X_3 . Cross-sections of the the hole pockets (β and γ) are visible at Γ . (b) Dispersion along $\Gamma - X_1$, centered on the hole bands. (c) Dispersion along $\Gamma - X_1$ centered on the electron pocket along the major axis of the ellipsoid. There is no band crossing along this direction. (d) Momentum dispersive cuts along the minor axis of the ellipsoid electron pocket ($X_2 - X_3$ direction). (e) Zoomed-in dispersion along $X_2 - X_3$ at $T = 7$ K conforming the absence of a Dirac cone. (f) The Fermi surface of LaAs from DFT calculations in agreement with the ARPES picture. (g) Symmetrized constant energy surfaces taken at E_F of LaAs at $T = 7$ K. (h) The same view at $T = 220$ K.

is as compensated as LaSb/LaBi, and the difference in R_H comes from an order of magnitude difference in the relative mobilities of electrons and holes (*mobility mismatch*) instead of their concentrations. Next, we turn to ARPES to map the Fermi surfaces of LaAs and to investigate signatures of topological band structure.

3.1.4 ARPES Results

Prior ARPES studies suggest a progression from topological to non-topological band structure in lanthanum monopnictides with decreasing pnictogen size. LaBi

has topological band inversion with Dirac cones [47, 49, 50]. LaSb appears to be on the verge of a transition from topological to trivial band structure [47, 51, 52]. Here, we investigate the case for LaAs.

Fig. 3.2(a) is a 2D constant energy surface at E_F , symmetrized to fill the entire Brillouin zone. LaAs has ellipsoidal pockets at the faces of the fcc Brillouin zone (X points) and two concentric spheroidal pockets at the center of the zone (Γ point), similar to the Fermi surfaces of LaSb and LaBi [49, 51]. Figs. 3.2(b-e) show the measured dispersions along three paths (B), (C), and (D) as indicated on Fig. 3.2(a). Path (B) is along $\Gamma - X_1$, centered around Γ , showing that the two concentric pockets at Γ come from two hole bands. Path (C) is also along $\Gamma - X_1$, but centered around X_1 , showing the major axis of the ellipsoidal pocket which clearly comes from an electron band. Path (D) is along $X_2 - X_3$, showing the minor axis of the ellipsoidal electron pocket. The clear lack of a band crossing in all cuts precludes the existence of topological states in LaAs. Fig. 3.2(e) zooms in the dispersion along the $X_2 - X_3$ direction to highlight the clear gap beneath the α pocket with no evidence for a band crossing or a Dirac cone. These results demonstrate a transition in the lanthanum monopnictide family, from LaBi with topological band structure where Dirac cones are present, to LaAs with trivial band structure where Dirac cones are absent. In Appendix A.4, we present the dispersion of the electronic states at X along the sample normal direction (k_z) to confirm their periodicity and the absence of surface states. Fig. 3.2(f) renders the three dimensional Brillouin zone of LaAs with the electron pockets (α) at X and the hole pockets (inner β and outer γ) at Γ from DFT calculations.

Figs. 3.2(g) and (h) show a comparison of the Fermi surfaces measured in LaAs at $T = 9$ K and $T = 220$ K. The largely unchanged Fermi surfaces observed by ARPES rule out a Lifshitz transition in LaAs as a function of temperature, consistent with the Kohler scaling of the resistivity data in Fig. 3.1(c). Next, we

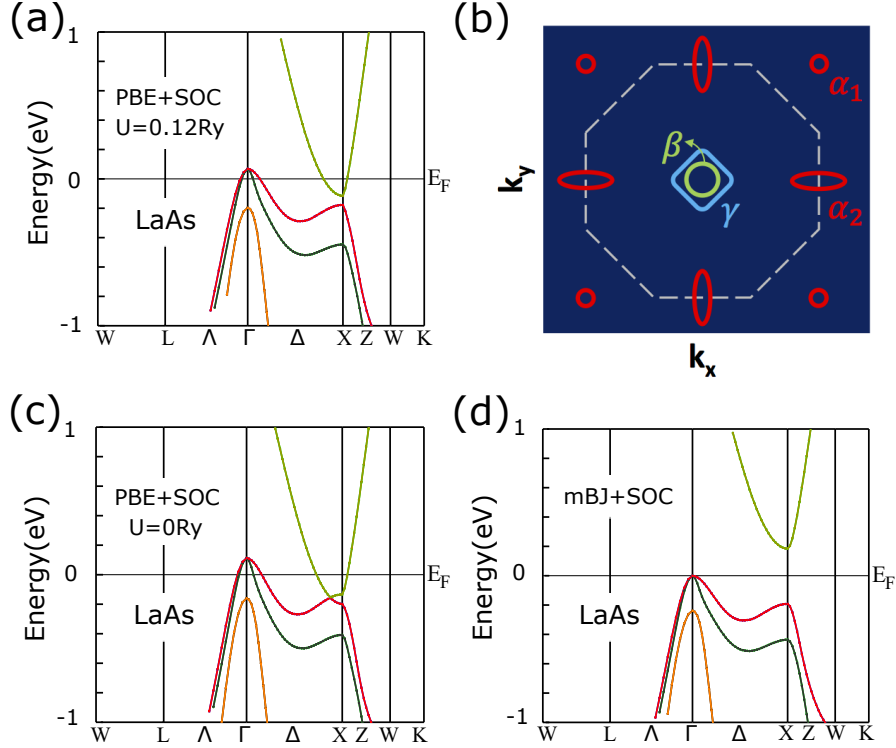


Figure 3.3: Band structure of LaAs. (a) The correct band structure of LaAs (consistent with ARPES and quantum oscillations) from a PBE+SOC+U calculation with $U = 0.12$ Ry. (b) Schematic 2D map of the Brillouin zone with ellipsoidal electron pockets (α) at the X points and concentric hole pockets (inner β and outer γ) at the Γ point. (c) Band structure of LaAs calculated by PBE+SOC showing a band crossing near X. (d) Band structure of LaAs calculated by mBJ+SOC showing a large gap that lifts the electron pocket from E_F .

discuss the DFT calculations that lead to Fig. 3.2(f).

3.1.5 Band Structure Calculation

As presented in the previous section, ARPES measurements along $\Gamma - X$, shown in Fig. 3.2, revealed two hole bands at Γ and one small electron pocket without band crossing at X. To capture these features, we performed a PBE+SOC+U calculation to open a gap at X while maintaining the position of the electron band bottom below E_F as shown in Fig. 3.3(a). The sizes of the gap and the electron pocket are tuned by varying U . Our choice of $U = 0.12$ Ry is justified by the size of the Fermi pockets determined by quantum oscillations as described in the next

section. Fig. 3.3(b) is a schematic illustration of the fcc Brillouin zone of LaAs in the $k_x - k_y$ plane. The larger (α_1) and the smaller (α_2) cross sections of the electron pockets appear at the X points. The smaller (β) and the larger (γ) hole pockets appear at the Γ point.

Due to the small sizes of LaAs Fermi surfaces, DFT calculations could easily produce misleading results. For example, Fig. 3.3(c) shows the outcome of a PBE+SOC calculation on LaAs. This calculation correctly captures the band structure of LaBi [40, 47]. However, in LaAs, it overestimates the α pocket size and incorrectly predicts a band crossing at X . Fig. 3.3(d) shows the outcome of a mBJ+SOC calculation on LaAs. This calculation accurately describes LaSb according to ARPES and transport experiments [27, 51]. However, in LaAs, it predicts that the electron pocket at X is lifted from the Fermi level, contradicting both the existence of the electron α pockets in Fig. 3.2(a) and the observed negative Hall effect in Fig. 3.1(e). Despite the simple rock-salt structure of lanthanum monopnictides, it is challenging to correctly predict their band structures without experimental guidance. Indeed, a prior theoretical DFT study incorrectly predicted LaAs to be a semiconductor with 0.1 eV gap [147].

3.1.6 Quantum Oscillation

For a precise measurement of the sizes of electron and hole pockets in LaAs, we studied quantum oscillations in the resistivity channel known as the Shubnikov-de Haas effect. Due to the small size of the Fermi surfaces in semimetals such as LaAs, it is challenging to reliably extract the Fermi volumes from the ARPES spectra as can be seen in Fig. 3.2. For example, the electron to hole carrier concentration in YSb is estimated to be $n_e/n_h = 0.81$ (moderate compensation) from ARPES [148] whereas $n_e/n_h = 0.95$ (almost perfect compensation) from quantum oscillations [149]. Fig. 3.4(a) shows the oscillatory part of resistivity

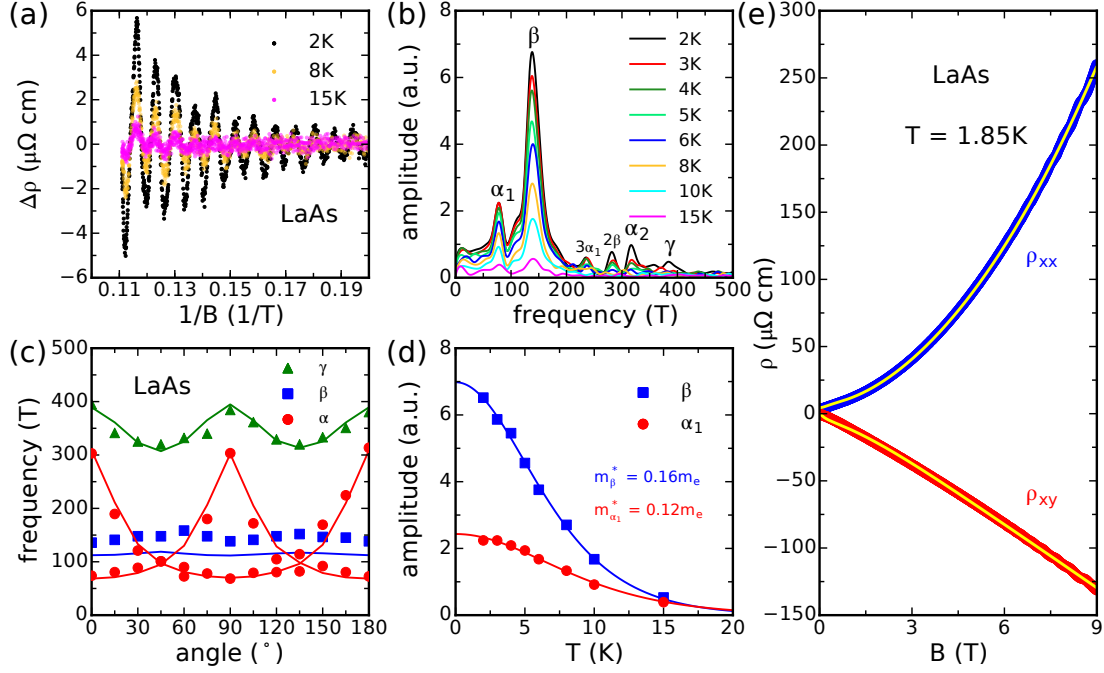


Figure 3.4: Quantum oscillations in LaAs and a multiband model fit. (a) The oscillatory part of resistivity $\Delta\rho$ plotted as a function of $1/B$ at three representative temperatures. (b) Fast Fourier Transform (FFT) of $\Delta\rho$ data at different temperatures. Four main frequencies (α_1 , α_2 , β , γ) and their harmonics ($3\alpha_1$, 2β) are identified. (c) The observed angular dependence of the main frequencies (solid symbols) agrees with the calculated results from DFT (solid lines). (d) Lifshitz-Kosevich fit to the temperature dependence of the FFT amplitudes. The effective masses of α_1 and β are extracted reliably within the resolution of our data. (e) Multiband fit implemented simultaneously to the resistivity (ρ_{xx}) and the Hall effect (ρ_{xy}) as a function of field. Here, the sign convention of ρ_{xy} is defined in such a way that the Hall coefficient $R_H = \rho_{xy}/B$ is positive for hole bands and negative for electron bands.

$\Delta\rho$ after removing a smooth background from the resistivity data at different temperatures. Oscillations are periodic in $1/B$ and their amplitudes decrease with increasing temperature. Fig. 3.4(b) shows the Fast Fourier Transform (FFT) spectrum of the oscillations at different temperatures. FFT peaks at $\alpha_1 = 76$ T and $\alpha_2 = 315$ T correspond to the smaller and the larger areas of the ellipsoidal electron pocket (α). The peaks at $\beta = 140$ T and $\gamma = 382.5$ T correspond to the smaller (β) and the larger (γ) hole pockets. These frequencies were used to tune the U in PBE+SOC+ U calculation (Fig. 3.3(a)) until the calculated frequencies from DFT matched the experimental frequencies (See Appendix A.3).

Angular dependence of the FFT peaks is used to assign the frequencies to α , β , and γ pockets. Fig. 3.4(c) shows a strong angle dependence for the α frequencies as expected from the minor (α_1) and the major (α_2) extremal areas of the ellipsoidal pocket [100]. The β frequency is angle independent as expected from a spherical pocket [100]. The γ frequency with a mild angle dependence corresponds to a jack-shaped pocket as illustrated in Fig. 3.2(f). Solid lines on Fig. 3.4(c) represent calculated frequencies for LaAs from DFT using the SKEAF program [100]. The agreement between calculated and observed frequencies at different angles confirms the Fermi surface geometry.

Using the Onsager relation $F = \frac{\phi_0}{2\pi^2} A_{ext}$, where ϕ_0 is the quantum of flux, we extracted the extremal orbit areas A_{ext} for α , β , and γ , then calculated their volumes to find the number of carriers in each pocket (see Appendix A.3. As a result, $n_\alpha = 1.55 \times 10^{19}$, $n_\beta = 0.94 \times 10^{19}$, and $n_\gamma = 3.66 \times 10^{19} \text{ cm}^{-3}$, corresponding to $n_e/n_h = 1.01$. A similar analysis on LaSb yields $n_e/n_h = 0.99$ [51]. Therefore, LaAs is as compensated as LaSb. The effective masses of the carriers on α_1 and β surfaces are estimated by fitting the FFT amplitudes to the Lifshitz-Kosevich formula [112, 113] in Fig. 3.4(d). The average mass, $m^* \approx 0.15 m_e$, used earlier to estimate T^* in Fig. 3.1(b), came from this analysis.

3.1.7 Discussion

The most striking difference between LaAs and the other members of its chemical family, LaSb and LaBi, is the significant reduction in the XMR magnitude of LaAs (Fig. 3.1(d)). Our goal is to understand this dramatic reduction of XMR magnitude in LaAs through the lens of the various probes presented thus far.

The Hall effect data in Fig. 3.1(e) showed that $R_H(T)$ had a much larger amplitude in LaAs with no change of sign, different from LaSb/LaBi. This could suggest a lack of compensation in LaAs, a proposed prerequisite for XMR [51]. However, ARPES (Fig. 3.2) qualitatively showed comparable electron and hole pockets, and quantum oscillations (Fig. 3.4) quantitatively confirmed their compensated densities in LaAs similar to LaSb/LaBi [39, 51, 150].

To further investigate this, we implemented a multiband fit to the field dependence of ρ_{xx} and ρ_{xy} simultaneously, as shown in Fig. 3.4(e) and elaborated in Appendix A.2. Our model assumed three electron pockets and two hole pockets, analogous to LaSb/LaBi, and supported by both our ARPES and quantum oscillations measurements. This multiband fit predicted $n_e/n_h = 1.005$ in LaAs, strengthening the consensus around compensation.

To explain the large discrepancies between $R_H(T)$ in the three compounds, we appeal to the mobility mismatch between electron and hole carriers. From the multiband fits in Fig. 3.4(e), the average electron to hole mobility ratio $\mu_e/\mu_h \approx 13$ in LaAs. This is an order of magnitude different from $\mu_e/\mu_h \approx 1$ in LaSb/LaBi [40, 51]. For a more intuitive understanding of the impact of such mobility mismatch on R_H , we turn to the two-band model expression for the Hall resistivity [151]:

$$R_H = \rho_{xy}/B = \frac{(R_h\rho_e^2 + R_e\rho_h^2) + (R_hR_e^2 + R_eR_h^2)B^2}{(\rho_h + \rho_e)^2 + (R_h + R_e)^2B^2} \quad (3.2)$$

where $R_{h(e)}$ and $\rho_{h(e)}$ stand for the Hall coefficient and the resistivity of an isolated

hole (electron) band. In the limit of compensation, where $n_e/n_h = 1$, Eq. 3.2 reduces to a simple form for the Hall coefficient ($R_H = \rho_{xy}/B$):

$$R_H = \frac{1}{ne} \frac{\mu_h - \mu_e}{\mu_h + \mu_e} \quad (3.3)$$

From here, we attribute the larger magnitude of R_H in LaAs (Fig. 3.1(e)) to the smaller Fermi surfaces i.e. smaller n , and we attribute the lack of sign change in LaAs to the mobility mismatch i.e. $\mu_e \neq \mu_h$.

LaAs, LaSb, and LaBi are all nearly compensated semimetals which exhibit XMR, albeit to varying magnitudes. Therefore, electron-hole compensation cannot be the cause for the significant reduction of XMR magnitude in LaAs when compared to its siblings. We argue instead that one key quantity for determining XMR magnitude in these compensated materials is the matching of electron and hole mobilities. A mobility mismatch allows for a larger Hall field to develop under applied magnetic fields. This larger Hall field in LaAs counteracts the Lorentz force more effectively and disrupts the field induced cyclotron motion, therefore reduces the XMR magnitude.

3.1.8 Conclusions

By growing and characterizing single crystals of LaAs, we confirmed the qualitative existence of XMR in this material although the magnitude is quantitatively much reduced. Quantum oscillations, multiband fit, and ARPES measurements confirm that LaAs is almost perfectly compensated, similar to LaSb/LaBi. The multiband fit shows that the larger Hall field and the smaller MR in LaAs are due to the electron-hole mobility mismatch instead of a lack of compensation. The challenges of band structure calculations for semimetals with small Fermi surfaces are highlighted by presenting three different DFT calculations on LaAs

with three different results. The correct calculation comes from a PBE+SOC+U scheme by tuning U until the calculated Fermi surfaces match the experimental observations. The ARPES measurements resolve a non-topological band structure in LaAs, placing it on the other side of a topological transition from LaBi. This is the first presentation of a transition from topological to non-topological band structure in the lanthanum monopnictide family. The existence of the XMR resistivity profile in all three materials must therefore result from compensation and independent of topology. Alternative explanations for XMR such as a field induced metal-insulator transition are also ruled out by confirming the Kohler scaling on the resistivity data and by showing nearly identical ARPES maps at $T = 7$ and 220 K³.

3.2 HoBi: Interplay between XMR and Magnetism

We report the observation of an extreme magnetoresistance (XMR) in HoBi with a large magnetic moment from Ho f -electrons. Neutron scattering is used to determine the magnetic wave vectors across several metamagnetic transitions on the phase diagram of HoBi. Unlike other magnetic rare-earth monopnictides, the field dependence of resistivity in HoBi is non-monotonic and reveals clear signatures of every metamagnetic transition in the low-temperature and low-field regime, at $T < 2$ K and $H < 2.3$ T. The XMR appears at $H > 2.3$ T after all the metamagnetic transitions are complete and the system is spin-polarized by the external magnetic field. The existence of an onset field for XMR and the

³This section is largely based on the publication “*Extreme magnetoresistance in the topologically trivial lanthanum monopnictide LaAs*” in Physical Review B [53]. F.T. is grateful to P. Rourke from NRC for discussions of SKEAF. T.N. would like to thank the NSF Graduate Research Fellowship Program for support during this work. The work at Boston College is funded by the NSF Grant No. DMR-5104811. The work at the University of Colorado is funded by the US Department of Energy Office of Basic Energy Sciences under Grant No. DE-FG02-03ER46066. The Diamond Light Source is funded as a joint venture by the UK Government through the Science and Technology Facilities Council (STFC) in partnership with the Wellcome Trust.

intimate connection between magnetism and transport in HoBi are unprecedented among the magnetic rare-earth monopnictides. Therefore, HoBi provides a unique opportunity to understand the electrical transport in magnetic XMR semimetals.

3.2.1 Introduction

Non-magnetic rare-earth monopnictides with a chemical formula RX where $R = Y$ or La and $X = As, Sb,$ and Bi have attracted attention because they exhibit a non-saturating and extremely large magnetoresistance (XMR) [26, 27, 39, 40, 47, 50, 51, 53, 148, 149, 152–154]. A topological to trivial transition is reported in the LaX family, from $LaBi$ to $LaAs$, with XMR being present on either side of the transition confirming that XMR originates from an electron-hole compensation instead of a topological band structure [53, 155]. Recently, XMR has been reported in a few magnetic rare-earth monopnictides including $CeSb$ [54, 55], $NdSb$ [56–58], $GdSb$ and $GdBi$ [55, 156, 157] where f -electrons provide localized moments. In these magnetic semimetals, the itinerant d/p -electrons couple to the localized f -electrons through the Ruderman-Kittel-Kasuya-Yosida (RKKY) interaction [158, 159] giving rise to antiferromagnetic (AFM) order, field induced metamagnetic (MM) transitions, and rich magnetic phase diagrams [160–166]. Despite complex magnetization curves $M(H)$ with multiple MM transitions, the magnetic monopnictides exhibit plain quadratic resistivity curves $\rho(H)$ and an XMR behavior similar to their non-magnetic analogues in the low-temperature regime ($T < 2$ K) [54, 55]. From $LaSb/LaBi$ to $CeSb$, $NdSb$, and then $GdSb/GdBi$, the lanthanide becomes progressively more magnetic, but intriguingly no strong response of transport and XMR to magnetism has been observed so far.

In search of such connection between magnetism and transport properties in a magnetic XMR material, we decided to study HoBi where Ho^{3+} ions provide the largest total angular momentum $\mathbf{J} = \mathbf{L} + \mathbf{S}$ among the R^{3+} ions. Through a combi-

nation of magnetization, neutron scattering, and transport experiments, we unveil an intimate relation between the electronic transport and the magnetism of HoBi unlike any previously studied magnetic RX system. Using neutron diffraction, we reveal a new $(1/6, 1/6, 1/6)$ ordered state at intermediate fields which strongly affects the resistivity behavior. The XMR in HoBi no longer follows a plain quadratic curve and appears only after the magnetic field is strong enough to drive the system out of this $(1/6, 1/6, 1/6)$ phase and into a $(0, 0, 0)$ spin polarized state.

3.2.2 Methods

Crystal growth and characterization– HoBi single crystals were grown using a self-flux method from Ho pieces (99.90%, Alfa Aesar) and Bi chunks (99.99%, Alfa Aesar). The starting materials were weighed in an Argon-filled glovebox (H_2O and O_2 contents < 1 ppm) in the mole ratio Ho:Bi = 5:95 with 4 grams total mass. The elements were placed in an alumina crucible inside an evacuated quartz tube and transferred to a box furnace. The furnace was set to 1000 °C at 3 °C/min, held at that temperature for 12 hours, and then cooled to 400 °C at 0.1 °C/min. Samples were annealed at 400 °C for 12 hours. Temperature was then increased to 600 °C at 3 °C/min and quartz tubes were centrifuged at 600 °C to empty the excess Bi flux and extract single crystals of HoBi. The high quality of crystals were confirmed by XRD, EDX, and a high residual resistivity ratio (RRR).

Resistivity and magnetization measurements– Resistivity was measured using a standard four probe technique and heat capacity was measured with a relaxation time method inside a Quantum Design PPMS Dynacool. DC magnetization measurements were performed using a vibrating sample magnetometer inside a Quantum Design MPMS3.

*Neutron diffraction*⁴– Single crystal neutron diffraction was performed on the

⁴Neutron diffraction experiments were conducted by J. Gaudet, A. A. Aczel, and B. D. Gaulin [99].

HB-1A triple-axis spectrometer at the High Flux Isotope Reactor (HFIR) at the Oak Ridge National Laboratory (ORNL). The fixed-energy incident neutron beam with $\lambda = 2.36 \text{ \AA}$ was selected by a double pyrolytic graphite monochromator. Energy analysis of the scattered beam employed a pyrolytic graphite analyzer crystal, giving an elastic energy resolution of approximately 1 meV.

*Calculations*⁵– DFT calculations with full-potential linearized augmented plane-wave (LAPW) method were implemented in the WIEN2k code [90] using the Perdew-Burke-Ernzerhof (PBE) exchange-correlation potential [91], spin-orbit coupling (SOC), and on-site Coulomb repulsion (Hubbard U) in a PBE+SOC+ U calculation [94] for the correlated $4f$ -electrons. Effective U values between 0.5 and 0.55 Ry were examined to find the correct band structure that matches the quantum oscillation results.

*High-field experiments*⁶– High-field experiments were performed in a 35 T DC magnet at the MagLab in Tallahassee inside a ^3He fridge with a base temperature of 0.3 K.

3.2.3 Magnetization and Metamagnetic Transitions

Prior studies of HoBi are limited to the magnetization measurements with $H \parallel [001]$ and $[111]$ directions [167, 168] as well as neutron scattering in zero-field showing type-II AFM order at $T_N = 5.7 \text{ K}$ [169]. A sketch of the fcc crystal structure of HoBi with the type-II AFM order at $H = 0$ is presented in Fig. 3.5(a). Local f -moments on Ho-atoms are parallel within each $[111]$ plane and antiparallel between alternate planes. From the heat capacity measurements in Fig. 3.5(b), we confirm the AFM phase transition with a peak at $T_N = 5.75 \text{ K}$. From the resistivity measurements in Fig. 3.5(c), we reveal a characteristic XMR profile with a large increase of $\rho(T)$ at low temperatures and a resistivity plateau. The magnitude of

⁵P. Blaha provided valuable suggestions for DFT calculations [99].

⁶D. E. Graf provided valuable help for high-field experiments [99].

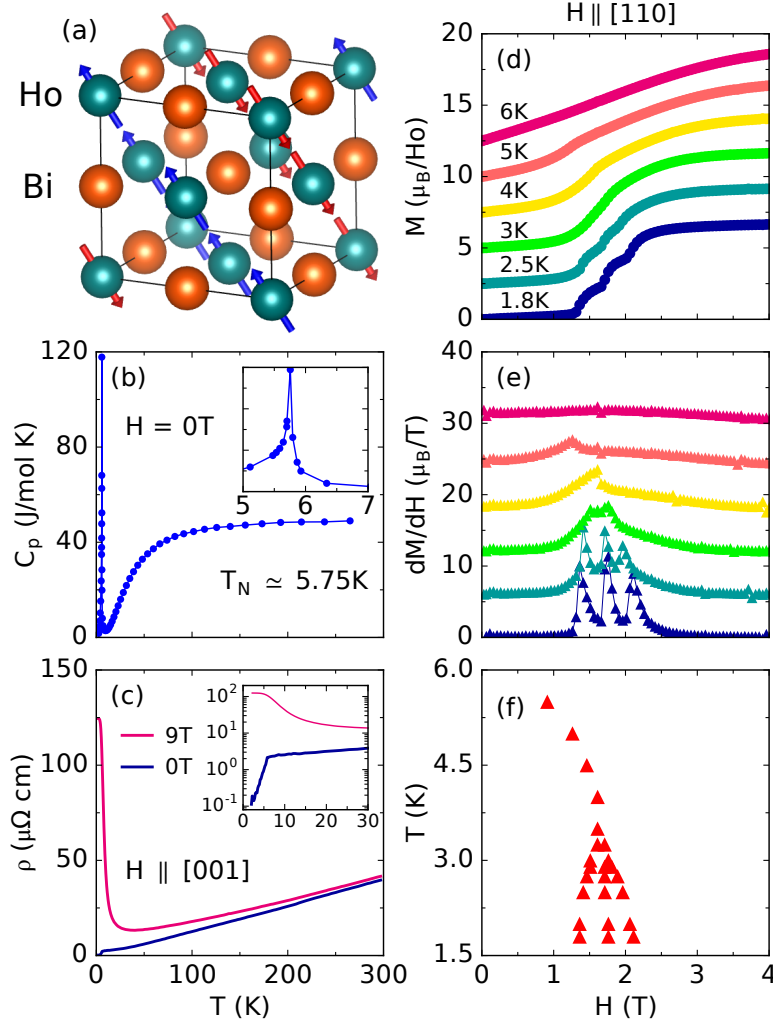


Figure 3.5: XMR and Magnetism in HoBi. (a) The rock-salt fcc structure of HoBi ($a = 6.23\text{\AA}$) with a type-II AFM order. (b) Heat capacity as a function of temperature at $H = 0$ T showing a peak at $T_N = 5.75$ K. (c) Resistivity as a function of temperature at $H = 0$ and 9 T showing XMR in a HoBi sample with $\text{RRR}(\rho(300\text{K})/\rho(0\text{K})) = 300$. (d) Magnetization, in units of μ_B per Ho-atom, as a function of magnetic field ($H \parallel [110]$) at several representative temperatures. Curves are shifted for visibility. (e) dM/dH as a function of field where $H \parallel [110]$. Each peak corresponds to a metamagnetic transition. (f) Magnetic phase diagram for $H \parallel [110]$ from the peaks in dM/dH data.

XMR is of the order $10^4\%$ when the field is oriented along either $[001]$ or $[110]$ directions (see Appendix B.1). In this letter, we first extend the magnetic phase diagram of HoBi to the $H\parallel[110]$ direction, which has not been studied before. Then, we use neutron scattering to determine the magnetic ordering wave vector in each sector of the phase diagram. Finally, we use the resistivity measurements to show the remarkable connection between the electrical and the magnetic properties of HoBi.

Figure 3.5(d) shows the magnetization curves at several representative temperatures with $H\parallel[110]$. The steps in the magnetization curves in Fig. 3.5(d) correspond to field-induced metamagnetic (MM) transitions which appear as peaks in the dM/dH curves in Fig. 3.5(e). There is only one peak in these data at $3.3\text{ K} < T < T_N$ that marks the boundary of the type-II AFM order. This single peak splits into three peaks below 3.3 K corresponding to three MM transitions. A phase diagram is produced in Fig. 3.5(f) from the evolution of dM/dH peaks measured at 12 different temperatures between 1.85 and 6 K. As shown in Appendix B.2, the phase diagram with $H\parallel[110]$ and $[111]$ have three MM transitions whereas the phase diagram with $H\parallel[001]$ has six MM transitions. Here, we focus on the $H\parallel[110]$ direction because it has a simpler phase diagram compared to the $[001]$ direction and is more accessible to both transport and neutron experiments compared to the $[111]$ direction.

3.2.4 Neutron Scattering

To determine the magnetic ordering vector of HoBi in each sector of its phase diagram (Fig. 3.5(f)), we turned to neutron scattering. We performed a broad survey of the neutron diffraction intensity for the momentum transfer \mathbf{Q} that covers the $[\text{HHL}]$ plane, perpendicular to the field direction $H\parallel[1-10]$. This is equivalent to $H\parallel[110]$ used in the magnetization and transport experiments. Figures 3.6(a–d)

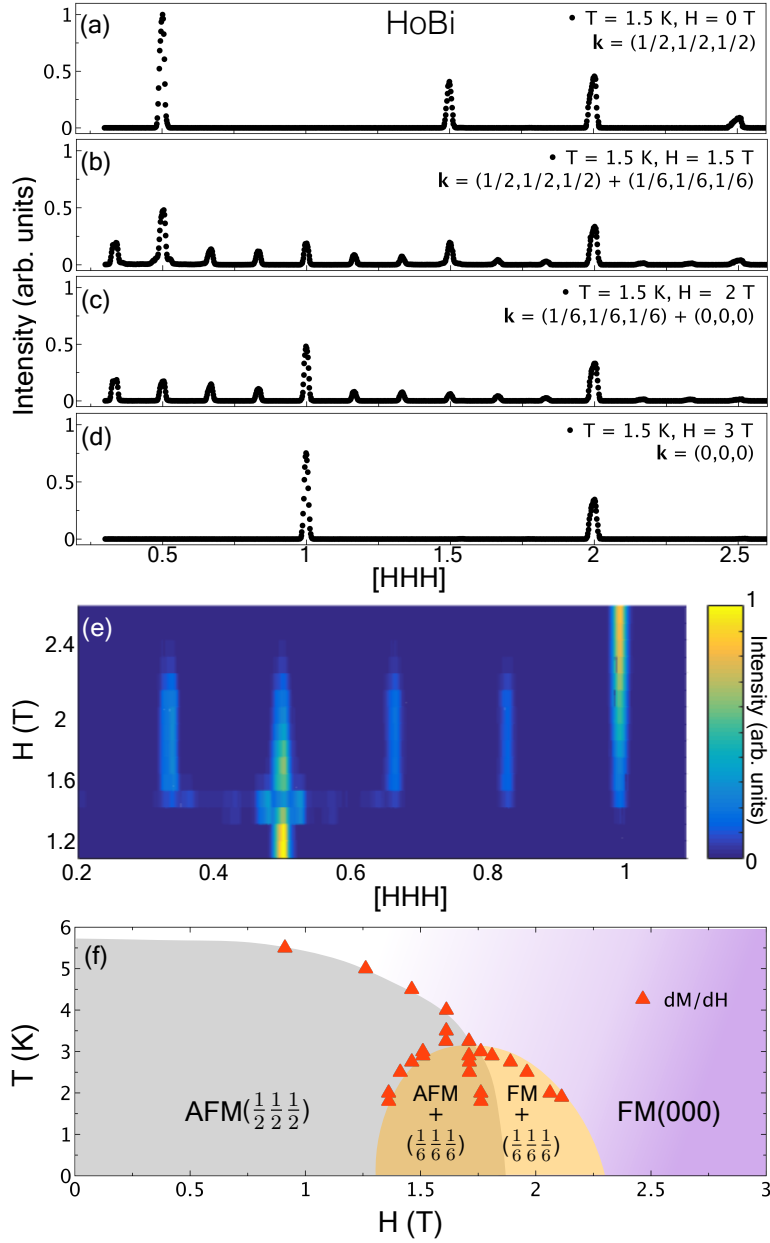


Figure 3.6: Neutron results and phase diagram of HoBi. (a–d) Neutron diffraction intensity along the $[HHH]$ direction at $H = 0, 1.5, 2,$ and 3 T measured at $T = 1.5$ K. Ordering wave vectors (\mathbf{k}) corresponding to each field are listed at the upper-right corner of each panel. (e) Color map of the neutron diffraction intensity as a function of field and momentum transfer \mathbf{Q} along the $[HHH]$ direction revealing the various metamagnetic transitions in HoBi. (f) Phase diagram of HoBi according to magnetization and neutron scattering.

show representative diffraction patterns along the [HHH] direction at $T = 1.5$ K and $H = 0, 1.5, 2,$ and 3 T covering all the MM phase transitions. At each field, structural Bragg peaks appear at $\mathbf{Q} = \mathbf{G}_{hkl}$ with fcc-type Miller indices. Within each magnetic phase, the Bragg peaks appear at $\mathbf{Q} = \mathbf{G}_{hkl} \pm \mathbf{k}$ where \mathbf{k} is the ordering wave vector. At $H = 0$, Fig. 3.6(a) shows magnetic Bragg peaks corresponding to $\mathbf{k} = (1/2, 1/2, 1/2)$ which specifies the zero-field type-II AFM order below T_N . At $H = 1.5$ T, after the first MM transition, new magnetic Bragg peaks appear corresponding to both first and higher order harmonics with $\mathbf{k} = (1/6, 1/6, 1/6)$. At $H = 2$ T, after the second MM transition, the peak intensities associated with $(1/6, 1/6, 1/6)$ remain unchanged, the $(1/2, 1/2, 1/2)$ peak intensities decrease, and a set of $(0, 0, 0)$ peaks emerge. The ordering vector $\mathbf{k} = (0, 0, 0)$ corresponds to a ferromagnetic (FM) alignment of the Ho spins. At $H = 3$ T, above the third MM transition, the $\mathbf{k} = (1/6, 1/6, 1/6)$ peaks disappear and the $\mathbf{k} = (0, 0, 0)$ remains as the only ordering wave vector.

Figure 3.6(e) summarizes the results of our measurements at intermediate fields by plotting a color map of the diffraction intensity at different [HHH] vectors. It shows the appearance of the $(1/6, 1/6, 1/6)$ order at $1.3 < H < 2.3$ T, the disappearance of the $(1/2, 1/2, 1/2)$ AFM order at $H > 1.8$ T, and the appearance of $(0, 0, 0)$ FM order at $H > 1.8$ T. In Fig. 3.6(f), a phase diagram of HoBi is constructed based on the magnetization and neutron scattering experiments. At $T = 0$, four distinct phases appear from low to high fields with the ordering wave vectors $\mathbf{k} = (1/2, 1/2, 1/2)$ (AFM) at $H < 1.3$ T, $\mathbf{k} = (1/2, 1/2, 1/2)$ and $(1/6, 1/6, 1/6)$ coexisting at $1.3 < H < 1.8$ T, $\mathbf{k} = (1/6, 1/6, 1/6)$ and $(0, 0, 0)$ coexisting at $1.8 < H < 2.3$ T, and $\mathbf{k} = (0, 0, 0)$ (FM) at $H > 2.3$ T. At finite temperatures, the $(1/6, 1/6, 1/6)$ order forms a dome-like boundary at $T < 3.3$ K. The dome is centered around a quantum critical point (QCP) where the AFM $(1/2, 1/2, 1/2)$ order ends at approximately $H_c = 1.8$ T.

3.2.5 Magnetoresistance

Having established the magnetic phase diagram, we now present the electrical transport data and study the XMR behavior. HoBi shows a typical temperature profile of XMR in Fig. 3.5(c) and a large magnitude of MR (%) = $100 \times (\rho(H) - \rho(0))/\rho(0)$ in Fig. 3.7(a). What makes HoBi unique among the magnetic monopnictides is an intimate connection between the magnetism and transport that modifies the XMR behavior in two ways.

First, each MM transition is marked with a clear feature in the resistivity of HoBi. Figure 3.7(a) shows two distinct regions in the field dependence of the magnetoresistance MR(H). The blue region at $H < 2.3$ T is the realm of AFM order and MM transitions. Figure 3.7(b) compares a representative $\rho(H)$ curve at 1.85 K, a dM/dH curve at 1.8 K, and the intensity of the $(1/6, 1/6, 1/6)$ neutron diffraction peak at 1.5 K in this region. With increasing field from zero, $\rho(H)$ shows peaks at the first and second MM transitions, and a steep increase at the third one (see arrows in Fig. 3.7(b)). These features evolve with temperature as shown in the inset of Fig. 3.7(c). Similar features appear in the $\rho(H)$ data at $3.3 < T < T_N$ and correspond to the AFM transitions (see Appendix B.3). The black circles on the phase diagram in Fig. 3.7(d) correspond to the AFM and MM transitions derived from the $\rho(H)$ curves. Without measuring magnetization, one can accurately map the magnetic phase diagram of HoBi using the resistivity data alone. Such complete correspondence between magnetization and resistivity data is not observed in other magnetic XMR materials with complex MM transitions [54]. In this regard, HoBi is an ideal platform of studying the interplay between magnetism and transport in XMR materials.

Second, an onset of XMR is observed in HoBi. The XMR only starts at $H > 2.3$ T in the yellow region of Fig. 3.7(a) and (c). At $T = 1.85$ K, a steep increase of MR is observed immediately above the onset field 2.3 T followed by a

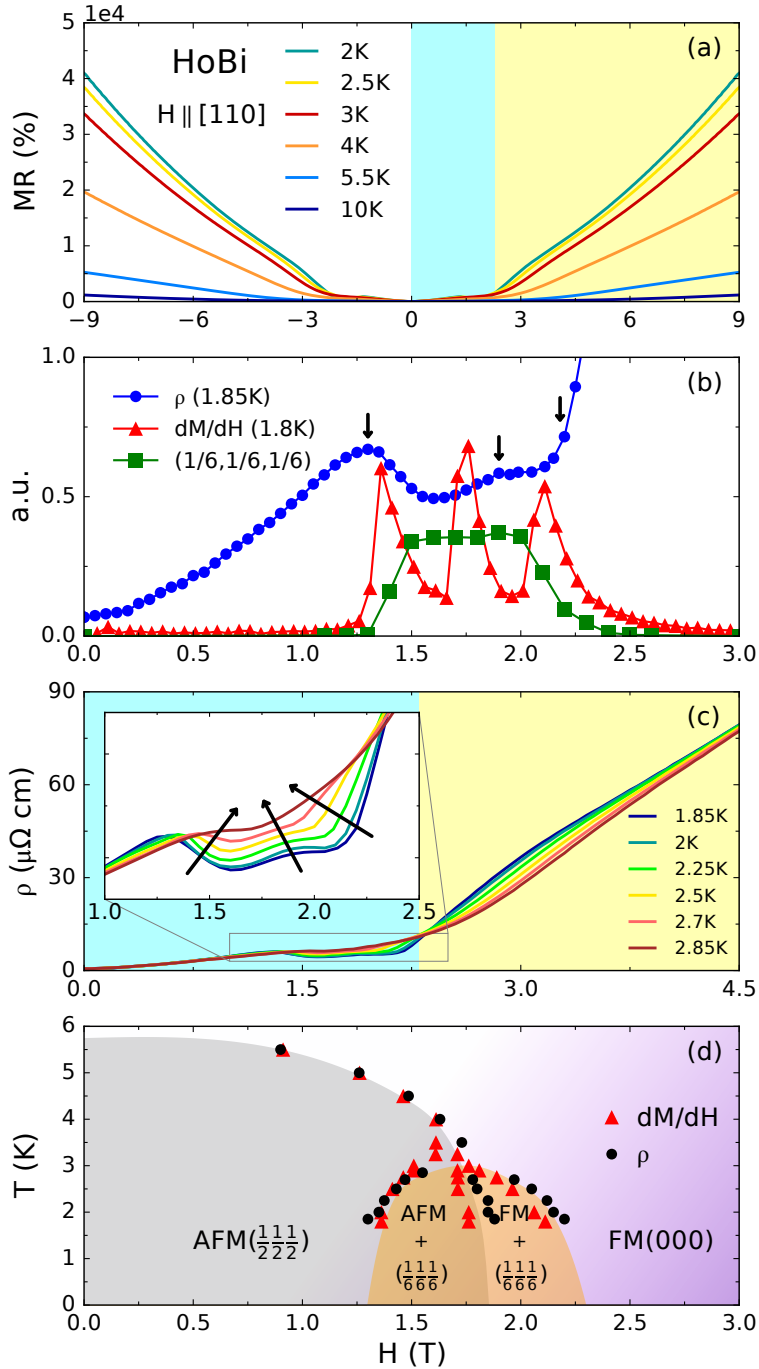


Figure 3.7: Magnetoresistance, onset of XMR, and the complete phase diagram of HoBi. (a) Magnetoresistance (MR) as a function of field ($H \parallel [110]$, $I \parallel [001]$) in a HoBi sample with $RRR = 127$ at several temperatures. The region of AFM order and MM transitions is highlighted by blue whereas the region of XMR is yellow. (b) Resistivity data (blue), dM/dH (red), and the $(1/6, 1/6, 1/6)$ neutron peak intensity (green) compared at comparable temperatures. Arrows mark the transport features associated with the MM transitions in $\rho(H)$. (c) Evolution of $\rho(H)$ with temperature. Note the onset of XMR (yellow region) at $H = 2.3$ T. (d) Phase diagram of HoBi from the transport, magnetization, and neutron scattering data.

less steep power law behavior at higher fields. The difference between these two behaviors is better resolved in $d\rho/dH$ curves (see Appendix B.4). The initial steep MR starts after the $(1/6, 1/6, 1/6)$ ordering wave vector has disappeared and when the Ho-spins are gradually polarizing with the field to adopt a FM $(0, 0, 0)$ state. This is in agreement with the magnetization curve at 1.85 K in Fig. 3.5(d) that does not fully saturate until about 3.5 T. Similarly, the FM $(0, 0, 0)$ neutron peak intensity keeps increasing with the field until 3.5 T (see Appendix B.4). Therefore, the disappearance of MM transitions and the gradual polarization of the Ho-spins with field are responsible for the onset of XMR.

The onset of XMR in HoBi is a unique feature among XMR materials studied so far. In non-magnetic XMR materials, $\rho(H)$ shows a quadratic behavior from zero to high fields. In magnetic XMR materials such as CeSb and NdSb, the overall $\rho(H)$ curve is quadratic, similar to non-magnetic systems [54, 55, 57, 58]. However, in HoBi, the quadratic $\rho(H)$ behavior is disrupted under the influence of AFM order and MM transitions in the blue region of Fig. 3.7. The XMR with a quadratic $\rho(H)$ dependence appears only at $H > 2.3$ T in the yellow region. Figure 3.7(b) provides compelling evidence that the $(1/6, 1/6, 1/6)$ ordering wave vector is responsible for this onset behavior that distinguishes HoBi from other magnetic XMR materials.

3.2.6 Quantum Oscillation and DFT Calculations

Prior studies of non-magnetic monpnictides including LaAs, LaSb, and LaBi have shown a characteristic compensated band structure for XMR with hole pockets at Γ and electron pockets at X in the fcc Brillouin zone [39, 53]. We used a combination of DFT calculations and Shubnikov-de Haas (SdH) oscillations to search for such Fermi surfaces in HoBi. Figure 3.8(a) shows the calculated band structure of HoBi in the XMR (FM) region, which resembles that of non-magnetic

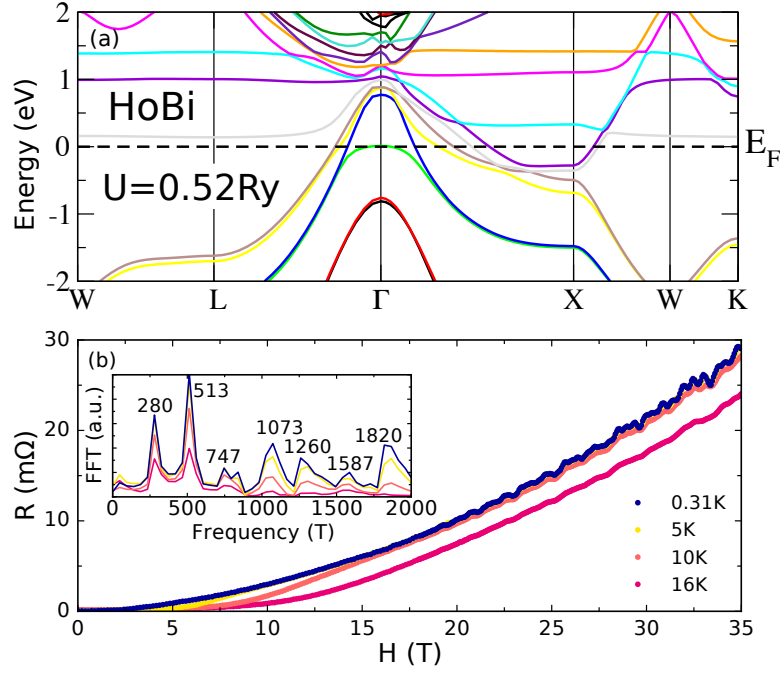


Figure 3.8: Band structure and quantum oscillations of HoBi. (a) Band structure of HoBi from a spin-polarized PBE+SOC+U calculation with 10,000 k -points, basis-size control parameter $RK_{max} = 9$, and $U = 0.52$ Ry (7.075 eV). HoBi has four hole bands at Γ and two electron bands at X similar to non-magnetic XMR semimetals. (b) SdH oscillations in electrical resistance at $20 < H < 35$ T. Inset shows the Fourier transform of SdH oscillations at several temperatures.

Table 3.1: QO frequencies and effective masses in HoBi. Calculated frequencies and effective masses from the PBE+SOC+U calculations compared to the SdH experimental results in HoBi. Four hole bands (h_{1-4}) and two electron bands ($e_{1,2}$) are observed. The frequencies F and the effective masses m^* are reported in units of T and m_e . DFT calculations suggest a maximum and a minimum frequency in h_4 , e_1 , and e_2 .

band	h_1 F, m^*	h_2 F, m^*	h_3 F, m^*	h_4 F, m^*
DFT	243, 1.14	1003, 0.20	1558, 0.45	1975/1986, 0.4/0.42
SdH	280, 0.27	1073, 0.50	1587, 0.38	1820, 0.58

band	e_1 F, m^*	e_2 F, m^*
DFT	838/1290, 0.47/0.82	489/835, 0.54/0.46
SdH	747/1260, 0.29/0.50	513/747, 0.29/0.29

XMR materials mentioned above. There are four hole bands at Γ and two electron bands at X . In particular, notice the smallest hole-pocket that barely touches the Fermi level at Γ . The size of this pocket is extremely sensitive to the choice of U and serves as a stringent test of the calculation (see Appendix B.5). We use the SKEAF program [100] to calculate the extremal orbit area and the effective mass of carriers on each calculated Fermi surface. The results are then compared to the frequencies of SdH oscillations in Fig. 3.8(b). Fourier transform of the oscillations is shown in the inset with a low-frequency peak at 280 T corresponding to the smallest hole-pocket in Fig. 3.8(a) with a calculated frequency of 243 T. Furthermore, we measured the mass of carriers on each pocket using a standard Lifshitz-Kosevich analysis [112, 113] as elaborated in Appendix B.6. Table 3.1 shows a good agreement between the frequencies and effective masses from DFT calculations and SdH oscillations. Our analysis of Fermi surfaces confirms that the non-saturating XMR in HoBi at high magnetic fields originates from a compensated band structure with hole pockets at Γ and electron pockets at X , similar to the non-magnetic analogue LaBi [26, 39, 53].

3.2.7 Conclusions

In conclusion, HoBi is the only magnetic rare-earth monopnictide with XMR where the transport behavior, especially XMR, is strongly affected by changes in the magnetic wave vector. Metamagnetic transitions are resolved in the $\rho(H)$ data clearly so the magnetic phase diagram of HoBi can be accurately mapped from the transport data. The $(1/6, 1/6, 1/6)$ dome is intriguing; it affects the XMR behavior drastically and drives its field dependence away from a plain quadratic curve. It is likely that the $(1/6, 1/6, 1/6)$ order is produced by a reconstruction of the Fermi surface at the QCP as a result of special nesting conditions. It would be interesting to confirm this idea and to search for its consequences such as charge

ordering in HoBi⁷.

⁷This section is largely based on the paper “*Interplay of Magnetism and Transport in HoBi*” published in Physical Review B [99]. The work at Boston College was funded by the National Science Foundation, Award No. DMR-1708929. The work at McMaster University was funded by NSERC of Canada. The National High Magnetic Field Laboratory is supported by National Science Foundation through NSF/DMR-1644779 and the State of Florida. A portion of this work used resources at the High Flux Isotope Reactor, a DOE Office of Science User Facility operated by Oak Ridge National Laboratory.

CHAPTER IV

RAIX Material Family (R=Rare-Earths, X=Ge/Si)

4.1 PrAlGe_xSi_{1-x}: Transition from Intrinsic to Extrinsic AHE

Recent reports of a large anomalous Hall effect (AHE) in ferromagnetic Weyl semimetals (FM WSMs) have led to a resurgence of interest in this enigmatic phenomenon. However, due to a lack of tunable materials, the interplay between the intrinsic mechanism caused by Berry curvature and extrinsic mechanisms due to scattering remains unclear in FM WSMs. In this contribution, we present a thorough investigation of both the extrinsic and intrinsic AHE in a new family of FM WSMs, PrAlGe_{1-x}Si_x, where x can be tuned continuously. Based on the first-principles calculations, we show that the two end members, PrAlGe and PrAlSi, have different Fermi surfaces but similar Weyl node structures. Experimentally, we observe moderate changes in the anomalous Hall coefficient (R_S) but significant changes in the ordinary Hall coefficient (R_0) in PrAlGe_{1-x}Si_x as a function of x . By comparing the magnitude of R_0 and R_S , we identify two regimes; $|R_0| < |R_S|$ for $x \leq 0.5$ and $|R_0| > |R_S|$ for $x > 0.5$. Through a detailed scaling analysis, we uncover a universal anomalous Hall conductivity (AHC) from intrinsic contribu-

tion when $x \leq 0.5$. Such a universal AHC is absent for $x > 0.5$. Our study thus reveals the significance of extrinsic mechanisms in FM WSMs and reports the first observation of the transition from intrinsic to extrinsic AHE in $\text{PrAlGe}_{1-x}\text{Si}_x$.

4.1.1 Introduction

The Hall effect in ferromagnets is commonly characterized by the following empirical formula for the Hall resistivity ρ_{xy} [60, 61]:

$$\rho_{xy} = \rho_{xy}^O + \rho_{xy}^A = R_0 H_z + R_s M_z, \quad (4.1)$$

where R_0 and R_s are ordinary and anomalous Hall coefficients, respectively. The ordinary Hall effect (ρ_{xy}^O) is linearly proportional to the applied magnetic field (H_z) through R_0 which is simply related to carrier concentration in a single-band metal. The anomalous Hall effect (AHE) ρ_{xy}^A , however, is proportional to the ferromagnetic moment M_z through R_s which involves a complicated combination of extrinsic and intrinsic mechanisms. The main extrinsic mechanisms are skew-scattering [63] and side-jump [64], both of which are related to the scattering between electrons and impurities with spin-orbit coupling. In contrast, the intrinsic (Karplus-Luttinger) mechanism originates from an anomalous velocity resulting from a phase shift in the electronic wave-packet which is independent of impurities [62, 65]. Since the reformulation of the intrinsic mechanism in terms of Berry curvature [65, 66], this concept has been invoked to explain the AHE in the canonical AHE material, bcc iron [68]. The intrinsic mechanism is gaining increasing attention because it is also applicable to the AHE in WSMs where the Weyl nodes, monopoles of the Berry curvature, can potentially generate a large AHE[33]. Recently, several WSMs have been found to exhibit such large AHE, including pyrochlore iridates ($\text{Nd}_2\text{Ir}_2\text{O}_7$) [170, 171], Heusler and half-Heusler com-

pounds (Co₂MnGa, GdPtBi) [105, 172, 173], and FM WSMs such as shandite structures (Co₃Sn₂S₂) [34]. All these discoveries have been interpreted as intrinsic AHE, and the extrinsic contributions have been overlooked. For example, in the topological ferromagnet Fe₃Sn₂, the intrinsic contribution to AHE is confirmed via a scaling analysis, but the extrinsic contribution could be five times larger than the intrinsic one [70, 102]. Also, most studies of AHE are based on the analysis of a single compound and are, therefore, quite limited in their ability to distinguish between extrinsic and intrinsic contributions. One experimental approach to address this issue would be to maintain the structure of the Weyl nodes but change the Fermi surface (or vice versa) across a series of compositions and tune the relative magnitude of extrinsic and intrinsic AHE contributions. This is precisely the subject of the present article where we explored this possibility in the FM WSMs PrAlGe_{1-x}Si_x. We study the AHE in PrAlGe_{1-x}Si_x alloys with $x = 0, 0.25, 0.5, 0.7, 0.85$ and 1 to investigate both intrinsic and extrinsic contributions to the AHE in this tunable FM WSM family. Although the end members, PrAlGe and PrAlSi, are both FM WSMs with the same number of Weyl nodes, we reveal a transition of the AHE from an intrinsic ($x \leq 0.5$) to an extrinsic regime ($x > 0.5$). The significance of our results is two fold. First, we demonstrate the importance of extrinsic contributions to AHE even in a FM WSM with robust Weyl nodes. Second, we reveal a transition from intrinsic to extrinsic AHE in the same family of FM WSMs and show the possibility of tuning AHE in topological semimetals.

4.1.2 Methods

Crystal growth— Single crystals of PrAlGe_{1-x}Si_x were grown using a self-flux method from Pr ingots (99.00%, Alfa Aesar), Al lumps (99.5%, Alfa Aesar) Ge pieces (99.999%+, Alfa Aesar) and Si lumps (99.999%+, Alfa Aesar). The starting

chemicals were mixed with the mole ratio Pr:Al:Ge:Si = 1:10:1 - $y:y$, placed in a crucible inside an evacuated quartz tube, heated to 1000 °C at 180 °C/hour, stayed at 1000 °C for 12 hours, cooled to 700 °C at 6 °C/hour, and annealed at 700 °C for another 12 hours. Then, the tube was centrifuged to remove the excess Al flux. All crystals of $\text{PrAlGe}_{1-x}\text{Si}_x$ were plate-like with the surface of the plate normal to the c -axis and its edges along the a -axis. FullProf suite was used for the Rietveld refinement¹ of the Powder XRD data [75]. The chemical composition of each crystal was determined by energy dispersive X-ray (EDX) spectroscopy using a ZEISS Ultra-55 field emission scanning electron microscope equipped with an EDAX detector. Our EDX analysis (see Appendix C.1) showed that $x = y$ in $\text{PrAlGe}_{1-x}\text{Si}_x$ samples with $y = 0, 0.5$, and 1. However, samples with $y = 0.75$ and 0.9, turned out to have $x = 0.7$ and 0.85, respectively, as seen from Table C.1 in Appendix C.1.

Notably, single crystals of PrAlGe made by flux growth and floating zone technique that have been reported in the literature show slightly different properties[174, 175]. The resistivity and magnetization characteristics of our PrAlGe samples are similar to those reported in Ref. [174] with a residual resistivity ratio (RRR) ≈ 2.2 that is 70% larger than the samples grown by floating zone technique (RRR ≈ 1.3 in Ref. [175]). Also, unlike the samples in Ref. [175], the EDX results in Appendix C.1 show that our samples are not Al-rich as we used a smaller quantity of Al-flux. We performed EDX measurements on three samples from each batch. The standard error for each composition is less than 1%, even though EDX can have accuracy errors of up to 5%. The EDX detector was calibrated with both Al and Si standards prior to the measurements.

Resistivity and magnetization Measurements– Electrical resistivity was measured with a standard four-probe technique and the heat capacity was measured

¹The Rietveld refinement was performed by F. Bahrami [77].

with a relaxation time method in a Quantum Design physical property measurement system (PPMS) Dynacool. The dc magnetization experiment was conducted on the vibrating sample magnetometer in a Quantum Design MPMS3. The high-field experiment² was performed in a 35 T dc Bitter magnet inside a ³He fridge at a base temperature of 300 mK, at the National High Magnetic Field laboratory in Tallahassee. All samples used for transport measurements were carefully sanded to remove the residual Al-flux and to have the ideal bar geometry for the determination of resistivity.

*Calculation*³– Electronic structure calculations were performed within the framework of DFT using the experimental lattice parameters and the projector augmented wave (PAW) method implemented in the Vienna ab-initio simulation package (VASP) [176]. Exchange-correlation effects were included using the generalized gradient approximation (GGA), and the spin-orbit coupling effects were included self-consistently [91, 177]. An on-site Coulomb interaction was added for Pr *f*-electrons within the GGA+U scheme with $U_{\text{eff}} = 6$ eV. An effective Wannier tight-binding Hamiltonian was obtained from the ab-initio results by using the VASP2WANNIER90 interface. This Hamiltonian was subsequently used to obtain topological properties [178].

*Second Harmonic Generation*⁴– The second harmonic generation (SHG) data were taken at normal incidence from the [101] face of as-grown crystals for incoming (outgoing) wavelengths 1500 (750) nm as a function of the incoming field polarization and measured for emitted light polarized parallel to [010] crystalline axis. In this geometry, all bulk contributions to SHG from a $I4_1/amd$ space group are forbidden, including the bulk magnetic dipolar, electric quadrupolar,

²D. E. Graf provided valuable help for high-field experiments [77]

³B. Singh performed first-principles calculations and theoretical analysis with assistance and guidance from C.-Y. Huang, W.-C. Chiu, S.-M. Huang, B. Wang, H. Lin, and A. Bansil [77].

⁴B. Lu and D. H. Torchinsky performed SHG experiments [77].

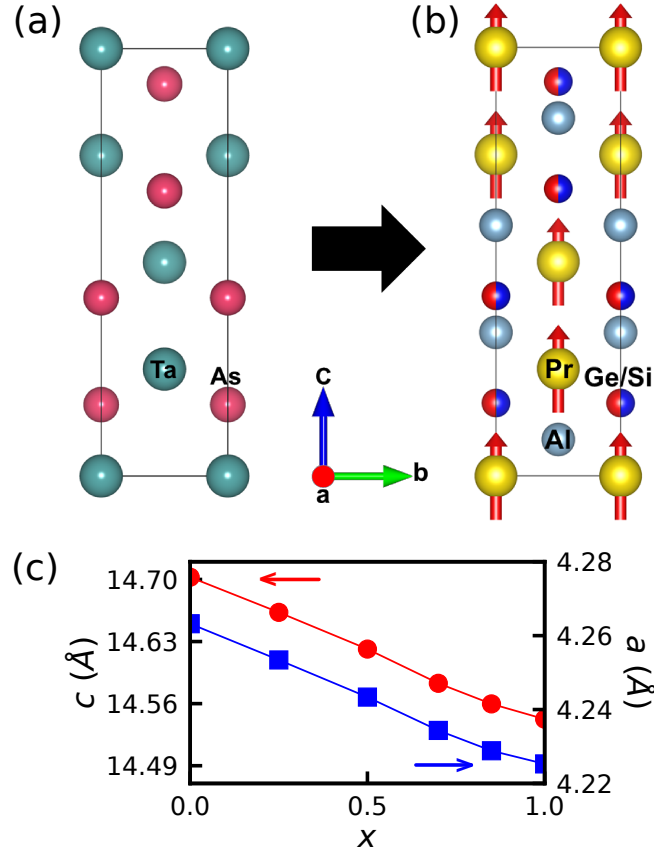


Figure 4.1: Crystal structure of $\text{PrAlGe}_{1-x}\text{Si}_x$. (a) Crystal structure of TaAs in the space group $I4_1md$ (#109). (b) The unit cell of $\text{PrAlGe}_{1-x}\text{Si}_x$, which is similar to TaAs but with additional Al atoms. (c) Continuous change of lattice parameters as a function of x among $\text{PrAlGe}_{1-x}\text{Si}_x$ compounds.

and electric-field induced SHG.

4.1.3 Crystal Structure

PrAlGe and PrAlSi are both WSMs due to broken inversion symmetry [72] similar to the archetypal WSM, TaAs [179, 180]. However, they undergo an FM transition at $T_C = 15\text{-}17$ K unlike TaAs which remains non-magnetic at all temperatures. As shown in Fig. 4.1(a) and (b), TaAs and the $\text{PrAlGe}_{1-x}\text{Si}_x$ crystallize in the same noncentrosymmetric space group ($I4_1md$) with the important difference that the Pr atoms in $\text{PrAlGe}_{1-x}\text{Si}_x$ provide a net magnetic moment along

the c -axis below T_C . Furthermore, a solid solution of Ge and Si is realized in $\text{PrAlGe}_{1-x}\text{Si}_x$ which results in a continuous change of lattice parameters as seen in Fig. 4.1(c). The lattice parameters in Fig. 4.1(c) are obtained from the Rietveld refinement of the powder X-ray diffraction data in the non-centrosymmetric space group $I4_1md$ (Appendix C.2). The point group C_{4v} is confirmed by SHG refinements in Appendix C.3. This structure is characteristic of the entire $R\text{AlSi}(\text{Ge})$ family ($R = \text{rare-earth}$), and generally leads to the appearance of Weyl nodes in their band structure [72] as observed in LaAlGe , [181] CeAlGe , [76] PrAlGe , [174] and $\text{CeAlSi}_{0.3}\text{Ge}_{0.7}$. [182]. As we will see, the number and positions of the Weyl nodes are similar in $\text{PrAlGe}_{1-x}\text{Si}_x$ at different x but the Fermi surface significantly changes across the series, giving rise to two regimes of AHE in the $\text{PrAlGe}_{1-x}\text{Si}_x$ family.

4.1.4 Magnetic Properties

A combination of magnetization and heat capacity measurements reveal the FM order, hence the breaking of time-reversal symmetry. The magnetic properties are similar among $\text{PrAlGe}_{1-x}\text{Si}_x$ samples as seen in Fig. 4.2 that shows representative data at $x = 0, 0.5$, and 1. The magnetic susceptibility is two orders of magnitude larger when measured with $H\parallel c$ (χ_c in Fig. 4.2(a)) compared to $H\parallel a$ (χ_a in Fig. 4.2(b)), indicating a strong Ising-like magnetic anisotropy. Based on a Curie-Weiss analysis (see Appendix C.4), the three samples have comparable Weiss temperatures $\Theta_W = 30\text{--}40$ K and effective moments $\mu_{\text{eff}} = 3.4\text{--}3.7 \mu_B$ as expected from Pr^{3+} ($3.56 \mu_B$). The FM transition temperature T_C is evaluated from the peak in the heat capacity data which yields $T_C = 15.1(2), 16.3(2)$, and $17.2(2)$ for PrAlGe , $\text{PrAlGe}_{0.5}\text{Si}_{0.5}$, and PrAlSi , respectively (see Fig. 4.2(c)). The magnetization curves with $H\parallel c$ and $H\parallel a$ are compared in Fig. 4.2(d) where $M(H\parallel c)$ saturates at approximately 0.5 T but $M(H\parallel a)$ does not. This is consistent with

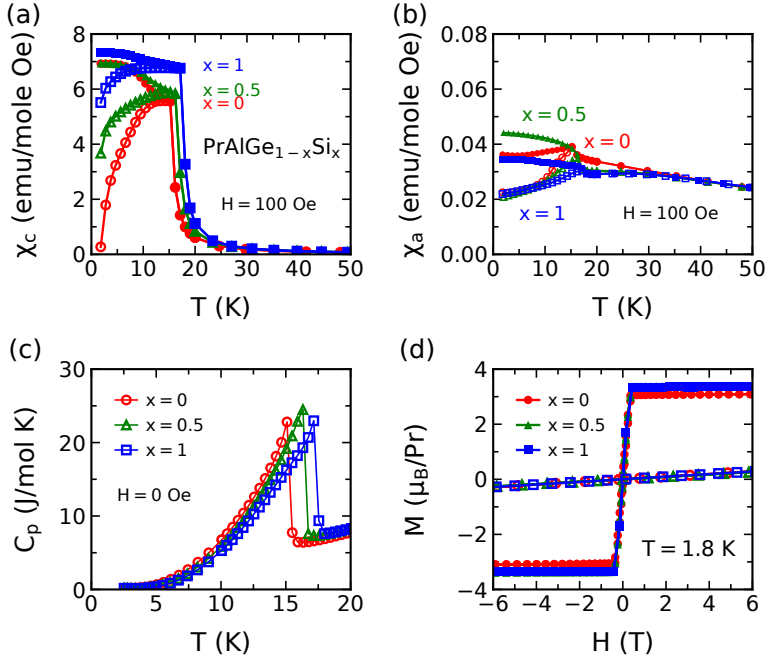


Figure 4.2: Magnetic properties of $\text{PrAlGe}_{1-x}\text{Si}_x$. (a) Magnetic susceptibility measured as a function of temperature with field parallel to the c -axis (χ_c). Red circles, green triangles, and blue squares represent the data for PrAlGe , $\text{PrAlGe}_{0.5}\text{Si}_{0.5}$, and PrAlSi , respectively (in all four panels). Empty and full symbols correspond to zero-field-cooling (ZFC) and field-cooling (FC), respectively. (b) Susceptibility data with field parallel to the a -axis (χ_a). Notice the y -scale is 100 times smaller than in panel (a) due to the Ising-like magnetic anisotropy. (c) Heat capacity as a function of temperature. The peaks correspond to T_C . (d) Magnetization as a function of field parallel to c - and a -axes (full and open symbols). Note that the coercive field is less than 0.1 T, so the hysteresis loop is not visible on this scale.

$\chi_c \gg \chi_a$ in Fig. 4.2(a) and the Ising anisotropy depicted in Fig. 4.1(b) with the c -axis as the magnetic easy-axis. The saturated moment for all $\text{PrAlGe}_{1-x}\text{Si}_x$ samples is approximately $3.3 \mu_B/\text{Pr}$. In summary, the magnetic properties of $\text{PrAlGe}_{1-x}\text{Si}_x$ samples are nearly identical.

4.1.5 Band Structure

We incorporated the crystalline and magnetic structures of PrAlGe and PrAlSi in our DFT calculations to arrive at realistic band structures. Even in a non-magnetic calculation, these compounds are Weyl semimetals due to broken inversion symmetry, similar to LaAlGe [181]. Including magnetism in DFT calculations shifts the location of Weyl nodes in k -space without changing their number. We compare the calculated band structures, Fermi surfaces, and Weyl nodes in PrAlGe (Figs. 4.3(a,c,e)) and PrAlSi (Figs. 4.3(b,d,f)). The band structure of both systems in Figs. 4.3(a,b) include tilted crossings near Σ and Σ_1 characteristic of type-II Weyl semimetals. The hole pocket between Σ_1 and Z is visibly larger in PrAlGe than that in PrAlSi . The Fermi surface is visualized for both PrAlGe and PrAlSi in Figs. 4.3(c,d) to highlight the larger size and the more isotropic shape of the hole pockets in PrAlGe compared to PrAlSi . Although the Fermi surfaces are quite different between the two compounds, their Weyl node structures as shown in Figs. 4.3(e,f) are quite similar. Both compounds have 40 Weyl nodes located at similar locations in the Brillouin zone. For completeness, we present the nodal structure of $\text{PrAlGe}_{0.5}\text{Si}_{0.5}$ in Appendix C.5 to confirm the same number of nodes across the entire series of $\text{PrAlGe}_{1-x}\text{Si}_x$. Notably, the preservation of topological properties with the substitution of elements is not always guaranteed [53], and such a preservation in the $\text{PrAlGe}_{1-x}\text{Si}_x$ family makes it a great platform to study the competition between intrinsic and extrinsic mechanisms of AHE.

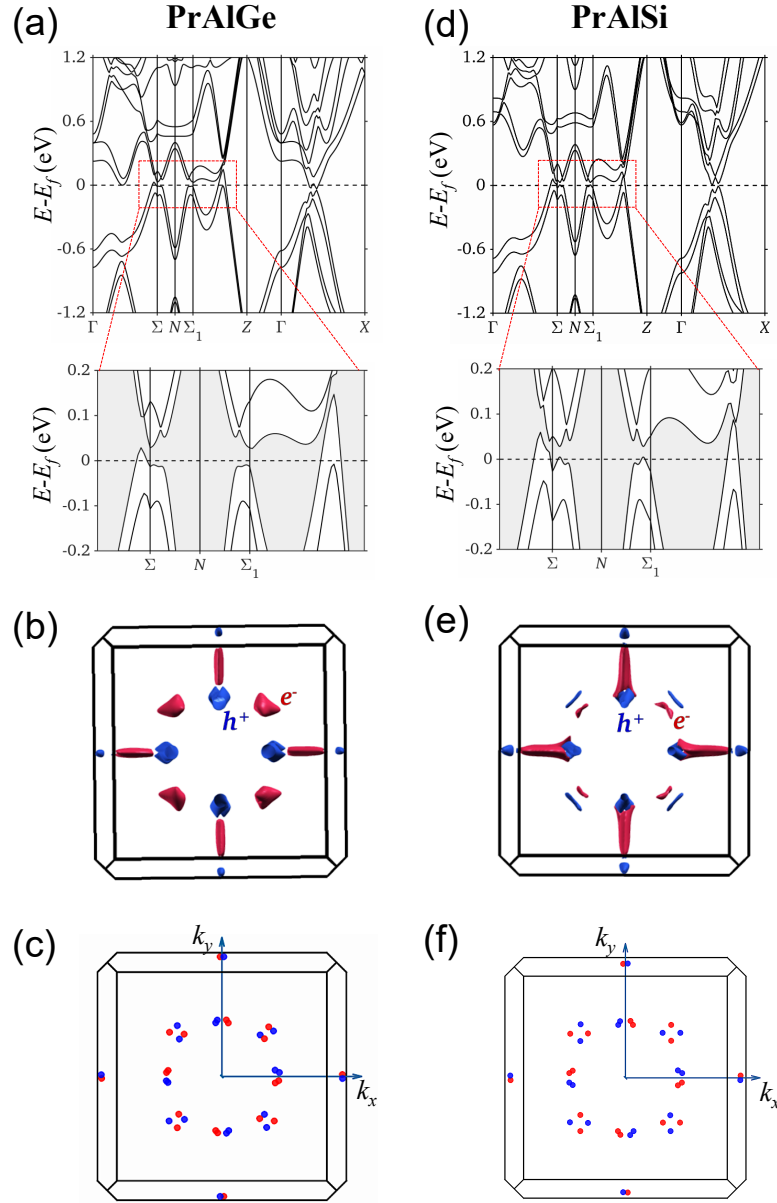


Figure 4.3: Band structure of $\text{PrAlGe}_{1-x}\text{Si}_x$. A comparison is made between the band structures (a,b), Fermi surfaces (c,d), and Weyl nodes (e,f) in PrAlGe and PrAlSi, respectively. Both noncentrosymmetric space group symmetry and FM order are considered in the calculations shown here. The shaded region in closeup band structure shows that valence and conduction bands are well separated along high-symmetry directions.

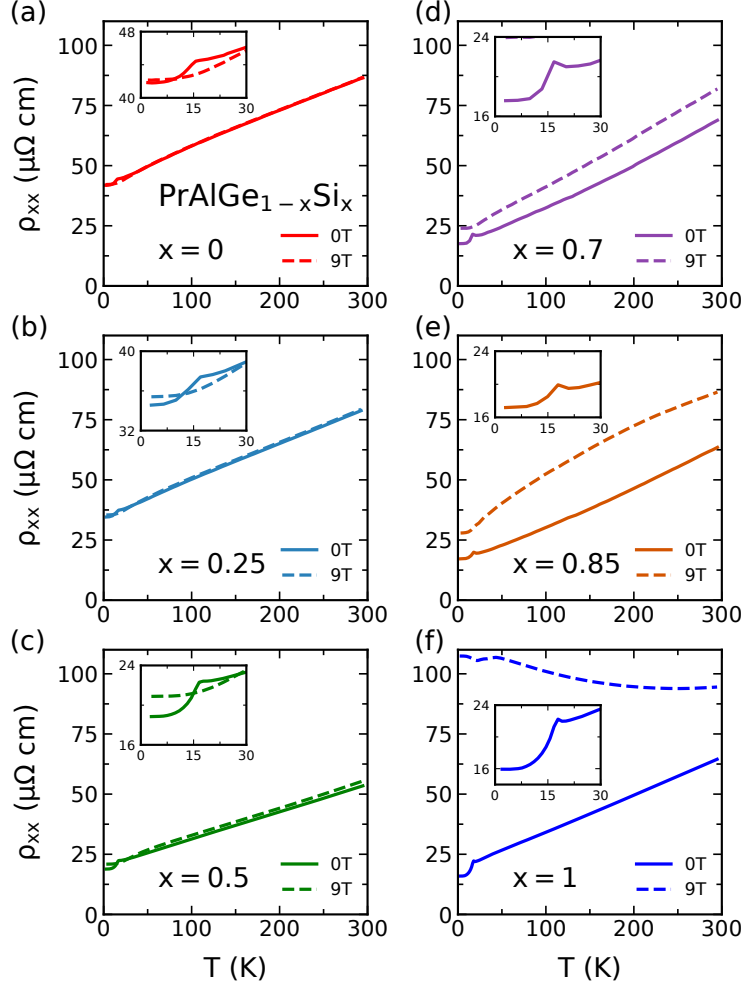


Figure 4.4: Resistivity of $\text{PrAlGe}_{1-x}\text{Si}_x$ as a function of temperature. Longitudinal resistivity ρ_{xx} plotted as a function of T in each $\text{PrAlGe}_{1-x}\text{Si}_x$ sample at both $H = 0$ and 9 T. The measurement was done with $I \parallel a$ and $H \parallel c$. The Si content for each sample (x) is quoted in the corresponding panels (a to f).

4.1.6 Electronic Properties

We observe considerable changes in the magnetoresistance $\text{MR}(\%) = 100 \times \frac{\rho_{xx}(H) - \rho_{xx}(0)}{\rho_{xx}(0)}$ within the $\text{PrAlGe}_{1-x}\text{Si}_x$ series. Figures 4.4(a) and 4.4(f) show very different temperature dependences of MR between the end members, PrAlGe and PrAlSi. The longitudinal resistivity ρ_{xx} is measured for each sample at both $H = 0$ (solid line) and 9 T (dashed line). PrAlGe shows a nearly field-independent ρ_{xx} at $T > T_C$, thus a negligible MR. A weak negative MR is observed near T_c which

is due to the magnetic fluctuations. In contrast, PrAlSi shows a considerably larger ρ_{xx} at $H = 9$ T compared to the zero-field data, thus a strong MR at all temperatures from 1.8 to 300 K. A continuous evolution of the MR is observed between these two limits in the rest of the PrAlGe $_{1-x}$ Si $_x$ samples in Figs. 4.4(b-e). The large difference in MR between PrAlGe and PrAlSi can be explained by a different $\omega_c\tau = H\sigma_{xx}(0)/ne$, where ω_c is the cyclotron frequency, τ is the relaxation time, $\sigma_{xx}(0)$ is the conductivity at 0 T, n is the carrier concentration, and e is the electron charge. A rough estimate of $\omega_c\tau$ at 2 K with data in Figs. 4.4 and 4.6 shows that its value in PrAlSi is 20 times larger than in PrAlGe. Therefore, PrAlSi is far more susceptible to the disruptive Lorentz force compared to PrAlGe leading to a much larger MR.

We present field dependences of both MR and Hall effect (ρ_{xy}) in Fig. 4.5. A weak MR is observed in PrAlGe as a function of field at $T = 30$ K (above T_C) in Fig. 4.5(a) consistent with Fig. 4.4(a). The MR gradually increases with increasing x in the PrAlGe $_{1-x}$ Si $_x$ series. Eventually, the MR in PrAlSi ($x = 1$) becomes 100 times larger than the MR in PrAlGe ($x = 0$). This behavior is more pronounced at $T = 1.8$ K (below T_C) in Fig. 4.5(b). We zoom in the low-field MR data in Fig. 4.5(c) to show the negative MR due to magnetic fluctuations in all samples. Although the negative MR is more pronounced in samples with higher x at $T = 1.8$ K, it never exceeds 4% and disappears at $T > 2T_C$ as seen in Fig. 4.4.

Figure 4.5(d) shows a variation of the Hall resistivity $\rho_{xy}(H)$ between different samples at $T = 30$ K (above T_C). The slope of the Hall resistivity $d\rho_{xy}/dH$ is small and positive at $H > 1$ T in PrAlGe; it gradually increases with increasing x and becomes significantly larger in PrAlGe $_{0.15}$ Si $_{0.85}$. Eventually, it shows an abrupt downturn in PrAlSi (at $H > 1$ T). This behavior is consistent with our DFT calculations that show smaller hole pockets with increasing Si-content x in Fig. 4.3. A gradual weakening of the antibonding orbital overlaps between the

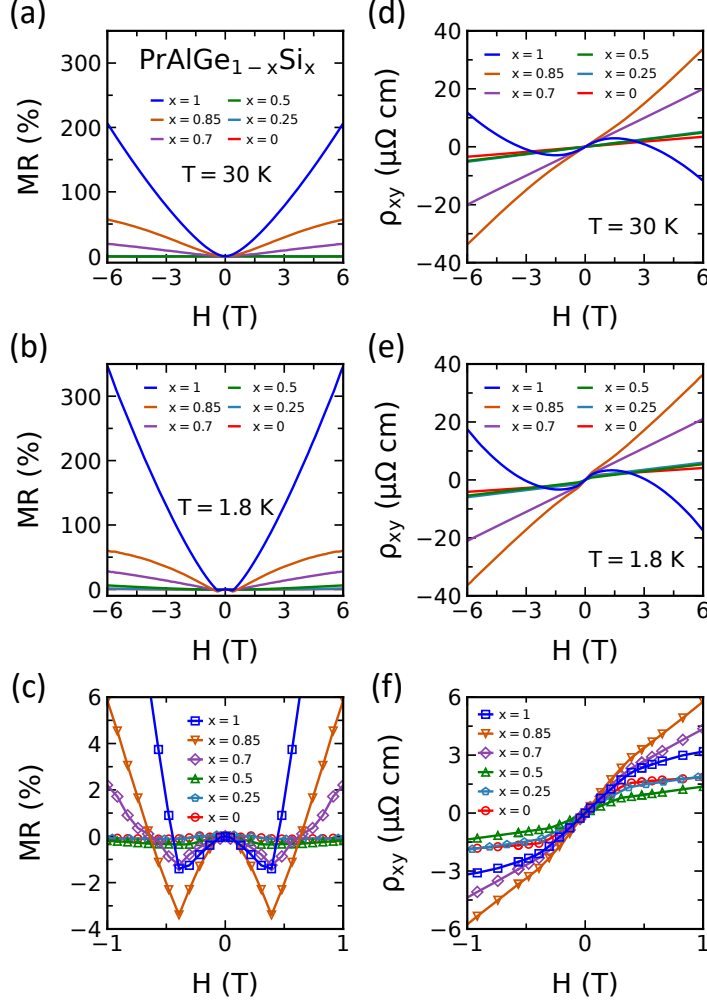


Figure 4.5: Resistivity and Hall effect of $\text{PrAlGe}_{1-x}\text{Si}_x$ in a magnetic field. (a) Transverse magnetoresistance in the $\text{PrAlGe}_{1-x}\text{Si}_x$ samples ($\text{MR}(\%) = 100 \times [\rho_{xx}(H) - \rho_{xx}(0)] / \rho_{xx}(0)$) measured as a function of field at $T = 30 \text{ K}$ ($> T_C$). The current is along a -axis and the applied field is along c -axis (z) in all panels. (b) MR at $T = 1.8 \text{ K}$ ($< T_C$). (c) A zoom-in view of panel (b) below 1 T. (d) Hall resistivity (ρ_{xy}) measured as a function of field at $T = 30 \text{ K}$ ($> T_C$). (e) ρ_{xy} at $T = 1.8 \text{ K}$ ($< T_C$). (f) A zoom-in view of panel (e) below 1 T.

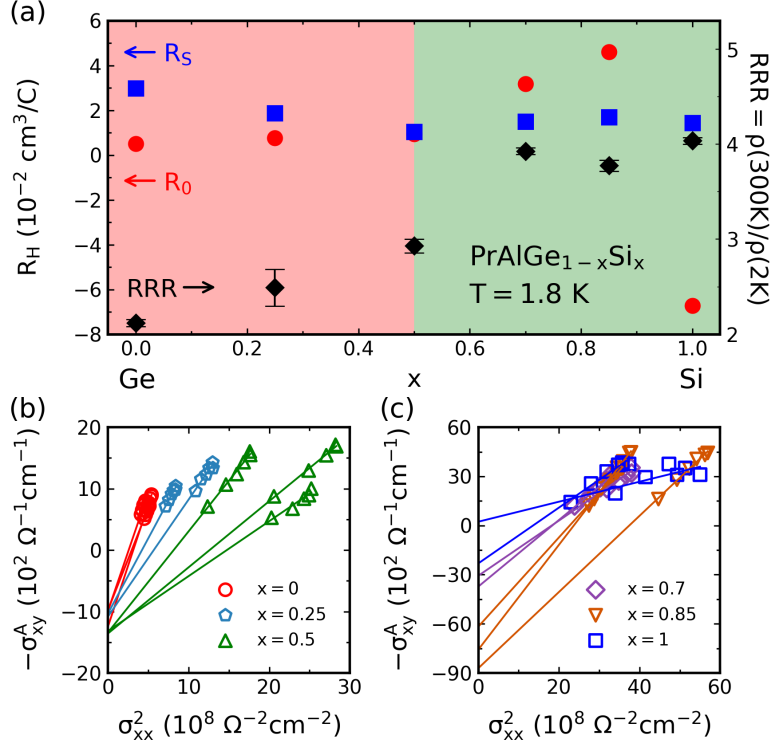


Figure 4.6: Anomalous Hall effect in $\text{PrAlGe}_{1-x}\text{Si}_x$. (a) Ordinary Hall coefficient (R_0), anomalous Hall coefficient (R_S) and residual resistivity ratio (RRR) are plotted as red circles, blue squares, and black diamonds, respectively, as a function of x in $\text{PrAlGe}_{1-x}\text{Si}_x$ at $T = 1.8$ K. The errorbars for R_0 and R_S are within the marker size, and the errorbar for RRR represents the range of RRR values for each composition. The red ($x \leq 0.5$) and green ($x > 0.5$) backgrounds distinguish two regions where the scaling analysis yields (b) the same intercept or (c) different intercepts according to Eq. 4.3.

p -orbitals of Al and Ge/Si with increasing x in $\text{PrAlGe}_{1-x}\text{Si}_x$ leads to smaller hole and larger electron Fermi surfaces. The ρ_{xy} behavior at high fields remains unchanged at $T = 1.8$ K (below T_C) as seen in Fig. 4.5(e). A zoom-in view at low-fields in Fig. 4.5(f) reveals the AHE in all samples at $T = 1.8$ K characterized by a rapid increase of $\rho_{xy}(H)$ until $H = 0.5$ T followed by a linear field dependence from $H = 0.5$ to 1 T. In the next section, we examine the AHE in detail and reveal a transition from intrinsic to extrinsic AHE in $\text{PrAlGe}_{1-x}\text{Si}_x$.

4.1.7 Anomalous Hall Effect

We present two separate analyses to investigate the AHE. The first analysis is based on Eq. 4.1 to differentiate the relative magnitudes of the ordinary and anomalous Hall coefficients (R_0 and R_S) in $\text{PrAlGe}_{1-x}\text{Si}_x$. The details of extracting R_0 and R_S are presented in Appendix C.6. We plot both R_0 and R_S as a function of x in Fig. 4.6(a) to reveal a crossing between the magnitudes of R_0 and R_S at $x = 0.5$ so that $|R_0|/|R_S| < 1$ at $x \leq 0.5$ but $|R_0|/|R_S| > 1$ at $x > 0.5$. The magnitude of R_S moderately decreases with increasing x at $x \leq 0.5$ and remains nearly unchanged afterwards. Whereas R_S shows only mild variations, R_0 shows considerable variations with x due to the change of Fermi surface shown in Fig. 4.3. R_0 is positive and increases slowly between $x = 0$ and 0.5, then increases rapidly until $x = 0.85$, and finally becomes negative abruptly at $x = 1$. Both the different $|R_0|/|R_S|$ ratios and different behaviors of the two Hall coefficients at $x \leq 0.5$ and $x > 0.5$ suggest a transition from one regime to another at $x = 0.5$. Furthermore, we are plotting RRR values for each composition in Fig. 4.6(a), revealing two different regimes. For $x \leq 0.5$, RRR increases linearly as x increases, but it saturates to approximately 4 for $x > 0.5$. These observations motivate our second analysis.

We follow the empirical analysis which was first proposed by Tian *et al.* [102] on iron thin films and was later justified theoretically [103, 104]. The analysis assumes a material not in the clean limit where the residual resistivity ρ_{xx0} plays an important role while the phonon scattering does not. These conditions are satisfied in $\text{PrAlGe}_{1-x}\text{Si}_x$ where $\text{RRR} \leq 4$ and the AHE occurs below 17 K so phonon scattering is negligible. Under such circumstance, the AHE can be described as

$$\rho_{xy}^A = (\alpha\rho_{xx0} + \beta\rho_{xx0}^2) + b\rho_{xx}^2 \quad (4.2)$$

where the coefficients α , β , and b parametrize the skew-scattering, side-jump, and intrinsic contributions to ρ_{xy}^A . The first two parameters depend on the impurity scattering in a specific sample, but the parameter b is independent of scattering. In general, the side-jump mechanism could also contribute to b through the same ρ_{xx}^2 dependence[104, 106]. However, in a material with topological band structures, we expect the intrinsic contribution to be dominant. Dividing both sides of Eq. 4.2 by ρ_{xx}^2 (and assuming that $\rho_{xx} \gg \rho_{xy}^A$)⁵ yields:

$$\sigma_{xy}^A = -(\alpha\sigma_{xx0}^{-1} + \beta\sigma_{xx0}^{-2})\sigma_{xx}^2 - b \quad (4.3)$$

where $\sigma_{xx0} = 1/\rho_{xx0}$ is the residual conductivity and $\sigma_{xy}^A = -\rho_{xy}^A/\rho_{xx}^2$ is the anomalous Hall conductivity (AHC). The first term in Eq. 4.3 depends on the residual conductivity and is sample dependent. However, the second term (b) is sample independent and constitutes the intrinsic contribution to the AHC.

Following Eq. 4.3, we measured two to three samples for each composition of $\text{PrAlGe}_{1-x}\text{Si}_x$, and determined b from the intercept of a linear fit to σ_{xy}^A as a function of σ_{xx}^2 . For example, the three data sets with green triangles in Fig. 4.6(b) correspond to three samples of $\text{PrAlGe}_{0.5}\text{Si}_{0.5}$. Their respective linear fits have different slopes showing different disorder levels, thus different α and β fitting parameters in Eq. 4.3. However, all three lines end at the same intercept (b) in the limit of $\sigma_{xx} \rightarrow 0$. The convergence of all linear fits strongly suggests an intrinsic mechanism for the AHE, which does not depend on the details of disorder level and only cares about the overall band structure. Interestingly, b seems to be the same in the three compositions $x = 0, 0.25, \text{ and } 0.5$ which is reasonably justified by the similar nodal structure of all $\text{PrAlGe}_{1-x}\text{Si}_x$ as illustrated in Fig. 4.3(c,f). Also, the magnitude of $\sigma_{xy}^{int} = -b \approx 10^3 \Omega^{-1}\text{cm}^{-1}$ is consistent with the magnitude

⁵In the limit $\rho_{xx} \gg \rho_{xy}^A$, the relations $\sigma_{xy}^A \sim \rho_{xy}^A/\rho_{xx}^2$ and $\sigma_{xx} \sim 1/\rho_{xx}^2$ are valid. In $\text{PrAlGe}_{1-x}\text{Si}_x$ this is the case as can be seen in the resistivity data (ρ_{xy}^A in Fig. 4.5(f) and ρ_{xx} in Fig. 4.4.)

of the resonant AHE caused by the intrinsic mechanism [107, 108]. Therefore, Fig. 4.6(b) suggests a universal intrinsic AHE in samples with $x \leq 0.5$. In contrast to Fig. 4.6(b), Fig. 4.6(c) shows that the parameter b varies randomly among samples with $x > 0.5$, hence the absence of a universal σ_{xy}^{int} . The failure of the scaling analysis suggests a predominantly extrinsic contribution to the AHC. Thus, we conclude that the AHE evolves from an intrinsic regime ($x \leq 0.5$) to an extrinsic one ($x > 0.5$) in $\text{PrAlGe}_{1-x}\text{Si}_x$, despite similar Weyl node structures in both end members, PrAlGe and PrAlSi .

4.1.8 Discussion and Conclusions

Here, we discuss the possible reasons underlying the transition from intrinsic to extrinsic AHE in the $\text{PrAlGe}_{1-x}\text{Si}_x$ family. We emphasize first that the failure of the scaling analysis for $x > 0.5$ does not imply that the intrinsic mechanism is absent, but only that the AHE is dominated by the extrinsic contribution in this regime. Earlier studies of itinerant ferromagnets show that the crossover from an intrinsic to extrinsic regime takes place as one approaches the clean limit [107, 108]. This trend is consistent with the results of Fig. 4.4 and Fig. 4.6(a), which show that σ_{xx} and RRR increase with x until $x = 0.7$ before it saturates. Larger values of both σ_{xx} and RRR with increasing x suggest that the system is approaching a cleaner limit where the extrinsic mechanisms become dominant as x increases [107]. Another factor that plays a role in the AHE for $x > 0.5$ is the position of E_F relative to the spin-orbit coupled bands. Figures 4.3(a) and (b) show that along the $\Gamma - X$ path, E_F crosses the conduction band in PrAlGe , but in PrAlSi E_F barely touches the conduction band and lies in a narrow gap. Notably, the occupied and unoccupied bands gapped out by spin-orbit coupling can possess finite Berry curvatures and opposite contributions to σ_{xy}^{int} [71, 183]. When E_F lies away from the gap, as is the case in PrAlGe , only the electronic levels with small Berry

curvatures will be populated with increasing temperature, so that σ_{xy}^{int} will not change substantially. In contrast, when E_F lies in the gap between the occupied and unoccupied bands (PrAlSi case), with increasing temperature, the unoccupied band will start to be populated and significantly reduce σ_{xy}^{int} . σ_{xy}^{int} will then acquire a temperature dependence that leads to the failure of the scaling analysis. The proximity to the clean limit and the relative position of E_F to the spin-orbit coupled bands together may explain why the scaling fails for $x > 0.5$, and the transition from intrinsic to extrinsic AHE in PrAlGe_{1-x}Si_x⁶.

4.2 CeAlSi: Loop Hall Effect Purely Induced by Weyl Nodes

An emerging frontier in condensed matter physics involves novel electromagnetic responses, such as the anomalous Hall effect (AHE), in ferromagnetic (FM) Weyl semimetals (WSMs). Candidate FM WSMs have been limited to materials that preserve inversion symmetry and generate Weyl crossings by breaking the time-reversal symmetry. These materials share three common features: a centrosymmetric lattice, a collinear FM ordering, and a large AHE observed when the field is parallel to the magnetic easy axis. Here, we present CeAlSi as a new type of FM WSMs in which the Weyl nodes are stabilized by breaking the inversion symmetry, but their positions are tuned by breaking the time-reversal symmetry. Unlike the other FM WSMs, CeAlSi has a noncentrosymmetric lattice,

⁶This work is largely based on the invited paper “*Transition from Intrinsic to Extrinsic Anomalous Hall Effect in the Ferromagnetic Weyl Semimetal PrAlGe_{1-x}Si_x*” published as part of the Special Topic on Topological Semimetals—New Directions in APL Materials [77]. We thank Chunli Huang and Hiroaki Ishizuka for helpful discussions. The work at Boston College was funded by the National Science Foundation through NSF/DMR-1708929. The work at Northeastern University was supported by the US Department of Energy (DOE), Office of Basic Energy Sciences, Grant No. DE-FG02-07ER46352, and benefited from Northeastern University’s Advanced Scientific Computation Center and the National Energy Research Scientific Computing Center through DOE Grant No. DE-AC02-05CH11231. The National High Magnetic Field Laboratory is supported by the National Science Foundation through NSF/DMR-1644779 and the State of Florida.

a noncollinear FM ordering, and a novel AHE that is anisotropic between the easy and hard magnetic axes. It also exhibits large FM domains that are promising for exploring both device applications and the interplay between the Weyl nodes and FM domain walls.

4.2.1 Introduction

Weyl nodes are protected linear crossings of two non-degenerate bands that lead to chiral relativistic quasiparticles [24, 184]. In WSMs, the presence of Weyl nodes at the Fermi level enables Berry phase engineering in the bulk, creates Fermi arcs on the surface, and leads to a host of emergent electromagnetic responses such as the topological Hall effect and the AHE [32, 33, 35, 61, 68, 77, 171, 185–191]. There are two main pathways for generating WSMs: breaking the inversion symmetry [192], or the time-reversal symmetry [15]. The former approach yielded the original discovery of non-magnetic WSMs in TaAs family [16, 17, 179]. The latter approach has recently led to the discovery of FM WSMs such as $\text{Co}_3\text{Sn}_2\text{S}_2$, Fe_3GeTe_2 , and Co_2MnGa [34, 69, 105, 193]. These FM WSMs crystallize in a centrosymmetric lattice and exhibit collinear FM ordering. They have been intensely studied due to a giant AHE that results from the Berry curvature around Weyl nodes, as confirmed by first-principle calculations [34, 68, 69, 105].

In this article, we introduce CeAlSi as a new type of FM WSMs that combines both routes mentioned above to generate Weyl nodes. CeAlSi crystallizes in the noncentrosymmetric space group $I4_1md$, a point we confirm via our second harmonic generation (SHG) experiments and first-principles calculations. The local f -moments of Ce^{3+} are found to interact within the noncentrosymmetric lattice and lead to a noncollinear FM order. The breaking of time-reversal symmetry in CeAlSi shifts the nodal positions and controls the magnitude of the AHE. We observe two different AHE responses in this material by orienting the magnetic

field along the easy and hard magnetic axes. The lack of inversion symmetry, the in-plane noncollinear FM order, and the novel anisotropic AHE make CeAlSi a new FM WSM candidate that is distinct from other FM WSMs.

4.2.2 Methods

Crystal growth and characterization– CeAlSi single crystals were grown by a self-flux method in both regular alumina crucibles and the Canfield crucible sets [194]. Both methods produced a similar crystal quality based on the PXRD⁷, SHG, EDX and resistivity measurements. In both methods, the starting materials were weighed in the ratio Ce:Al:Si = 1:10:1, placed inside a crucible in an evacuated quartz tube, heated to 1000 °C at 3 °C/min, stayed at 1000 °C for 12 h, cooled to 700 °C at 0.1 °C/min, stayed at 700 °C for 12 h, and centrifuged to decant the residual Al flux.

*Calculations*⁸– DFT calculations were performed using the experimental lattice parameters ($a = 4.252 \text{ \AA}$; $c = 14.5801 \text{ \AA}$) and the projector-augmented-wave (PAW) method implemented in the Vienna ab-initio simulation package (VASP) [176]. The exchange-correlation effects were included using the generalized gradient approximation (GGA). The spin-orbit coupling (SOC) was included self-consistently [91, 177]. An on-site Coulomb interaction was added for Ce f -electrons within the GGA+U scheme with $U_{\text{eff}} = 6 \text{ eV}$. A Wannier tight-binding Hamiltonian was obtained from the ab-initio results using the VASP2WANNIER90 interface, which was subsequently used in our topological properties calculations [178].

Transport, heat capacity, and magnetization measurements– Electrical resistivity was measured with the standard four-probe technique and the heat capacity was measured with the relaxation time method in a Quantum Design Physical

⁷F. Bahrami analyzed the X-ray data [78].

⁸B. Singh performed first-principles calculations and theoretical analysis with assistance and guidance from C.-Y. Huang, W.-C. Chiu, S.-M. Huang, B. Wang, H. Lin, and A. Bansil [78].

Property Measurement System (PPMS) Dynacool. Magnetic heat capacity C_m was obtained by first measuring the heat capacity of non-magnetic LaAlSi, and then subtracting it from the heat capacity of CeAlSi. DC magnetization experiments were conducted on the vibrating sample magnetometer in a Quantum Design MPMS3.

*High-field experiments*⁹– High-field experiments were performed using a 35 T DC Bitter magnet and a ³He fridge with base temperature of 300 mK at the MagLab in Tallahassee. Comparison of the quantum oscillation frequencies between theory and experiment was carried out by using the DFT-generated bxsf file and the program SKEAF [100].

*Neutron diffraction*¹⁰– The nuclear structure of CeAlSi was characterized by a single-crystal time-of-flight experiment at 100 K on TOPAZ at the Oak Ridge National Lab. A 3D diffraction map was acquired from 14 different sample positions allowing measurements of 6946 Bragg peaks where the nuclear structure factors were extracted following the method of Schultz *et al.* [195]. Structural refinements were performed using GSAS-II [196]. The magnetic structure was determined by diffraction experiments at the NIST Center for Neutron Research. The magnetic structure factors were determined using the thermal triple-axis spectrometer BT-7 by collecting rocking scans at various Bragg positions with incident and scattered neutron energies of 14.7 meV. Two single crystals were inserted in a top-loading CCR and a 7 T magnet to measure Bragg peaks in both the (H0L) and (HHL) planes. The order parameter measurement in Fig. 4.7(f) was performed with the SPINS spectrometer using 3.7 meV incident and scattered neutrons.

*Second harmonic generation*¹¹ – The SHG data in Fig. 4.7(b) were taken at normal incidence on the [101] face of as-grown crystals for incoming(outgoing)

⁹D. E. Graf provided valuable help for high-field experiments [78].

¹⁰J. Gaudet and C. L. Broholm performed neutron diffraction experiments [78].

¹¹B. Lu and D. H. Torchinsky performed SHG experiments [78].

wavelength of 1500(750) nm as a function of the incoming field polarization and measured for emitted light polarized parallel to the [010] crystalline axis [197]. In this geometry, all bulk contributions to the SHG signal from a $I4_1/amd$ space group are forbidden

*Scanning SQUID imaging*¹²– We used scanning SQUID susceptometers with two gradiometric field coils and pickup loops [198]. The SQUID pickup loop and the field-coil average radii were 3.25 and 7 μm formed from Nb lines of 0.5 and 1 μm width, respectively. The scanning SQUID apparatus was housed in a closed-cycle Montana Instruments Fusion cryostat (Bozeman, Montana, USA) with the cryostat base temperature of 3 K.

4.2.3 Main Results

Figure 4.7 summarizes our main results related to the discovery of a new non-centrosymmetric FM WSM with an anisotropic AHE. The body-centered tetragonal unit cell of CeAlSi (Fig. 4.7A) contains two vertical mirror planes (σ_v) but lacks a horizontal mirror plane (σ_h), thus breaking the inversion symmetry. The viability of an FM-WSM in such a structure (space group $I4_1md$) was first proposed by DFT calculations in CeAlGe [72, 181]; however, experiments reported an antiferromagnetic (AF) order instead of an FM order [76, 182, 199]. On the contrary, our neutron diffraction and magnetization measurements show that CeAlSi hosts an FM order with net magnetization along the crystallographic [110] direction and an in-plane non-collinear spin texture as illustrated in Fig. 4.7(a). Although the non-collinear FM order distinguishes CeAlSi from other FM WSMs, our neutron diffraction result shows that the angle between the non-collinear spins does not change with the applied magnetic field up to 8 T. Thus, the AHE observed in CeAlSi is distinct from the THE in non-coplanar magnets such as the MnGe and

¹²I. Sochnikov, B. Xu, and J. Franklin performed the scanning SQUID microscopy [78].

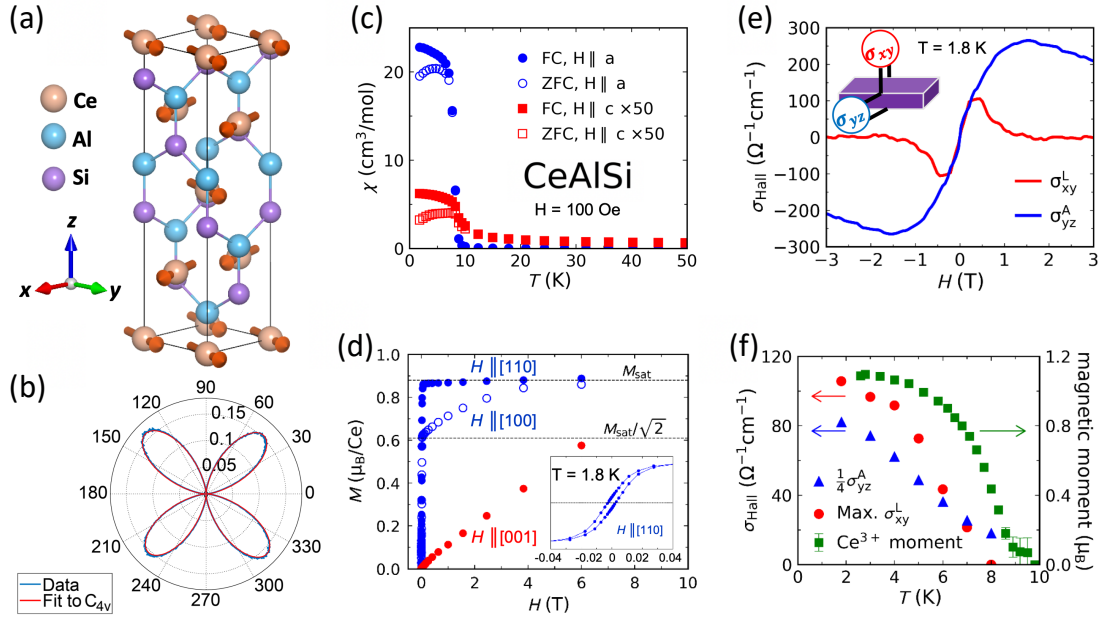


Figure 4.7: Non-collinear order, non-centrosymmetric structure, and anomalous Hall effect in CeAlSi. (a) Non-collinear FM order in the tetragonal unit cell of CeAlSi. (b) Second-harmonic generation data refined in the noncentrosymmetric C_{4v} point group. (c) Anisotropic magnetic susceptibility as a function of temperature showing the in-plane easy-axis. (d) Magnetization curves with the field oriented along the [110], [100], and [001] directions. Inset shows hysteresis due to FM domains with a coercive field of 70 Oe. (e) Two distinct Hall responses are observed when a magnetic field is applied along the easy axis (σ_{yz}^A : anomalous Hall effect) or the hard axis (σ_{xy}^L : loop Hall effect). (f) Evolution of the magnetic ordering parameter (the Ce^{3+} moment), σ_{yz}^A , and σ_{xy}^L with temperature. Note that the order parameter here does not represent the saturated moment, which only drops by $\sim 10\%$ from 1.8 K to 8 K (see Appendix D.3 for details).

MnSi [185, 186].

An important structural detail is the possibility of site mixing between Al and Si, which could invalidate the proposal of CeAlSi being a noncentrosymmetric FM WSM. Intersite mixing can restore the σ_h mirror plane and change the space and point groups from noncentrosymmetric $I4_1md$ (C_{4v}) to centrosymmetric $I4_1/amd$ (C_{4h}). Neither X-ray nor neutron diffraction can reliably distinguish between the two space groups, see Sec. M1 in the Supplemental Material for details. However, SHG can discriminate between these two structures because the SHG signal predominantly originates from a bulk electric dipole in a noncentrosymmetric unit cell. Figure 4.7(b) shows a strong SHG signal ($\chi_{xxz} = 200$ pm/V) that is commensurate with the pronounced signal in GaAs [200] and fits the point group C_{4v} . Thus, we confirm the noncentrosymmetric space group $I4_1md$ as the correct structure, see Sec. M2 in the Supplemental Material for details.

CeAlSi is ferromagnetic with a strong magnetic anisotropy with an in-plane easy axis. As seen in Fig. 4.7(c), the in-plane magnetic susceptibility (blue) is 200 times larger than the out-of-plane susceptibility (red). The field dependence of magnetization (Fig. 4.7(d)) indicates that the [110] crystallographic direction as the easy axis (see Appendix D.3 for the persistent saturation of magnetic moments at high fields). A gradual saturation of the $M(H\parallel[100])$ curve from $M_{sat}(H\parallel[110])/\sqrt{2}$ to $M_{sat}(H\parallel[110])$ implies the presence of zero-field magnetic domains with $\mathbf{M}\parallel$ [110], [1-10], [-110], and [-1-10] directions.

Due to the in-plane easy-axis orientation, we expect to observe an AHE when the magnetic field is oriented in the ab -plane. Figure 4.7(e) confirms such an anomalous Hall conductivity (the step in σ_{yz}^A), but it also reveals an unexpected signal (σ_{xy}^L) which is observed when the field lies along the hard axis. The superscript L in σ_{xy}^L stands for its loop-shape behavior. Figure 4.7(f) shows the parallel temperature dependence of σ_{yz}^A , σ_{xy}^L , and the magnetic order parameter determined

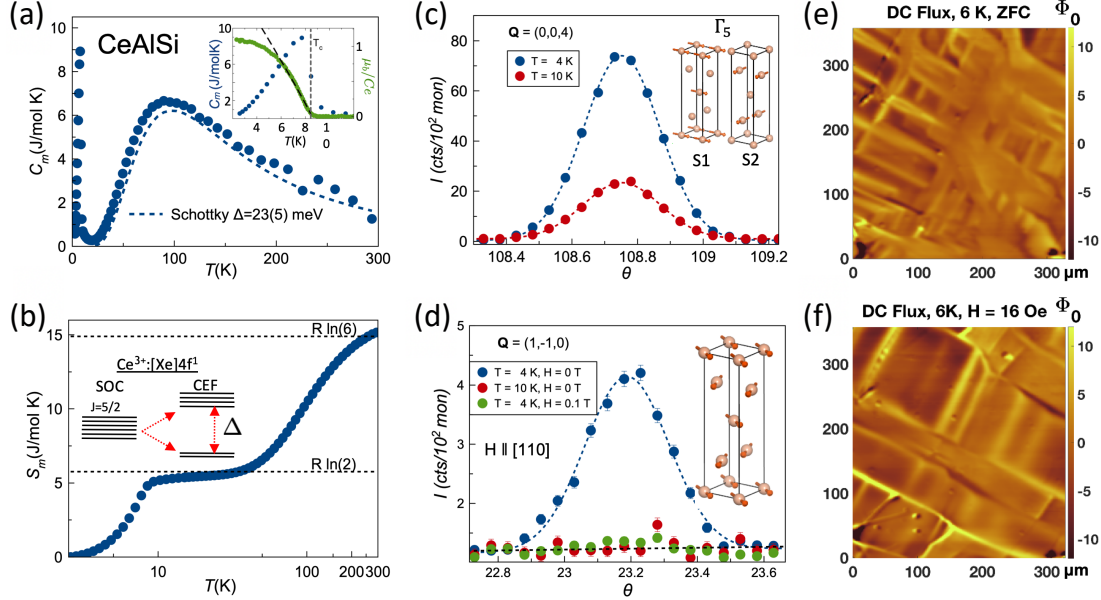


Figure 4.8: Magnetic structure of CeAlSi. (a) Magnetic specific heat as a function of temperature with a fit to the crystal electric field (CEF) levels. Inset shows a magnified view of the FM transition and a fit to the temperature dependence of the order parameter (magnetic moment per Ce atom). (b) Magnetic entropy as a function of temperature. Inset shows the CEF levels with a doublet ground-state. (c) Neutron scattering Bragg peak at $\mathbf{Q} = (0,0,4)$. (d) Neutron scattering Bragg peak at $\mathbf{Q} = (1,-1,0)$ is observed below $T_C = 8.2(3)$ K in zero-field and suppressed by applying a field of 0.1 T along the $[110]$ direction. (e) Scanning SQUID image of FM domains obtained at $T = 6$ K under zero field. (f) Large in-plane domains develop under a small in-plane field (16 Oe).

by neutron diffraction, suggesting that both Hall responses are controlled by the FM order. We will examine these findings in detail in subsequent sections.

4.2.4 In-Plane Noncollinear FM Order and Domains

The magnetic heat capacity (C_m) of CeAlSi in Fig. 4.8(a) exhibits a sharp FM transition at $T_C = 8.2(3)$ K and a broad (Schottky) peak at 80 K due to the crystal electric field (CEF) splitting of Ce^{3+} atomic levels. As shown in Fig. 4.8(b), the $J = 5/2$ sextet of Ce^{3+} splits into a doublet ground-state and a quadruplet excited-state, leading to two plateaus at $R \ln(2)$ and $R \ln(6)$ in the magnetic entropy S_m . From a fit to the C_m data in Fig. 4.8(a), we estimate a gap of $\Delta = 25$ meV

between the doublet and the quadruplet, and identify the ground-state of CeAlSi as a Kramers doublet with effective spin-1/2.

The in-plane noncollinear FM order of CeAlSi was determined by neutron diffraction. Figure 4.8(c) shows the $\mathbf{Q} = (004)$ peak corresponding to the FM ordering vector $\mathbf{k} = (000)$. The magnetic moment per Ce^{3+} (order parameter) is extracted from the intensity of this peak and plotted as a function of temperature in the inset of Fig. 4.8(a) along with the low- T heat capacity. These data are consistent with a second-order mean-field transition with the critical exponent $\beta = 0.48(4)$. Thus, the magnetic structure of CeAlSi belongs to a single irreducible representation (irrep) of the $I4_1md$ space group. The combination of our symmetry analysis (see Appendix D.4) with the observation of several (00L) peaks allows us to conclude that CeAlSi orders in the Γ_5 manifold, where all spins lie in the ab -plane (Fig. 4.8(c)).

As illustrated in the inset of Fig. 4.8(c), the Γ_5 manifold allows for a complete decoupling of the Ce spins between the adjacent $(0,0,z+1/4)$ layers. We define \mathbf{S}_1 to be the Ce spin at $(0,0,0)$ and \mathbf{S}_2 to be that at $(0,1/2,1/4)$. Intensity of the neutron Bragg peaks with $\mathbf{k} = (000)$ and (110) ordering vectors is proportional to $\mathbf{S}_1 + \mathbf{S}_2$ and $\mathbf{S}_1 - \mathbf{S}_2$, respectively. Thus, the observation of both the ordering vectors in Figs. 4.8(c) and (d) suggest that both $\mathbf{S}_1 + \mathbf{S}_2$ and $\mathbf{S}_1 - \mathbf{S}_2$ are finite, so that the angle between \mathbf{S}_1 and \mathbf{S}_2 , defined by $\theta = \cos^{-1}(\frac{\mathbf{S}_1 \cdot \mathbf{S}_2}{\|\mathbf{S}_1\| \|\mathbf{S}_2\|})$, must be nonzero. Detailed refinement of the spin structure was then performed against 40 symmetrically distinct Bragg peaks collected at both 1.4 K and 10 K in zero-field, see Sec. M3 in Supplementary Material for details. Assuming $\|\mathbf{S}_1\| = \|\mathbf{S}_2\|$, the refinement suggests a moment size of $1.2(2)\mu_B$ and $\theta = 70(30)^\circ$, confirming the in-plane noncollinear FM order in CeAlSi (inset of Fig. 4.8(d)).

We performed scanning SQUID microscopy [198, 201, 202] to visualize the FM domain structure of CeAlSi. The images in Figs. 4.8(e) and (f) were obtained

by scanning a SQUID sensor over the ab -surface of a polished crystal to measure the out-of-plane stray field from the in-plane domains. Although the domains are small under zero-field-cooling (Fig. 4.8(e)), a weak in-plane field of a few Gauss is enough to generate large in-plane FM domains that are hundreds of microns across (Fig. 4.8(f)). The development of large domains is also implied by the selection of a single domain revealed by neutron diffraction. Under a small in-plane field $\mathbf{H} \parallel [110]$, the system selects a single domain with $\mathbf{M} \parallel [110]$ among all symmetrically equivalent directions. As a result, the vector $\mathbf{S}_1\text{-}\mathbf{S}_2$ only points along $[1\text{-}10]$ and the $\mathbf{Q} = (1\text{-}10)$ Bragg peak is suppressed accordingly, as seen in Fig. 4.7(d) when a field of 0.1 T is applied in the $[110]$ direction. Magnitude of the observed DC flux is on the order of a few Φ_0 , consistent with the remnant magnetization determined from the c -axis bulk magnetization measurements. According to our estimates based on the remanent a -axis magnetization, if the domains were to have flipped magnetization from the in-plane to the out-of-plane direction, it would have produced DC signal on the order of hundreds of Φ_0 , which is clearly not the case in Figs. 4.8(e) and (f) (see Appendix D.5). The picture that emerges from our neutron scattering and scanning SQUID measurements in CeAlSi is that of a noncollinear in-plane FM order with large domains.

4.2.5 Band Structure, Shifted Weyl Nodes, and Intrinsic Anomalous Hall Conductivity

Band structure of CeAlSi (Fig. 4.9(a)) consists of small hole and electron pockets with a nearly vanishing density of states (DOS) at E_F (Fig. 4.9(b)). The DOS in the majority and minority spin channels peaks at different energies (Fig. 4.9(b)) and leads to FM ordering. The residual electron and hole pockets are illustrated in Fig. 4.9(c), which also shows the 12 pairs of Weyl nodes next to the $k_x = 0$ and $k_y = 0$ mirror-planes. We denote the 4 pairs of nodes located on the $k_z = 0$ plane

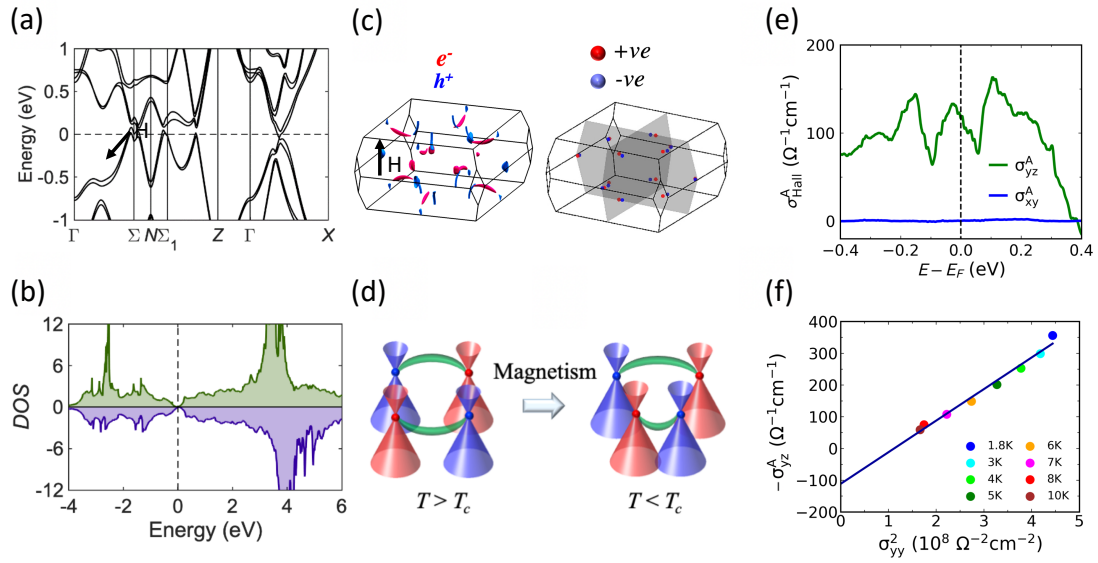


Figure 4.9: Band structure and Weyl nodes in CeAlSi. (a) Band structure of CeAlSi including spin-orbit coupling. (b) Partial density of states for the majority (green) and minority (purple) spin channels. (c) Electron (red) and hole (blue) pockets (left) and the Weyl nodes (right) are shown in the BZ. (d) Effects of breaking the inversion (left) and time-reversal (right) symmetries on the positions of Weyl nodes are shown schematically. (e) Theoretical values of the anomalous Hall conductivity with the field oriented in-plane (σ_{yz}^A) and out-of-the-plane (σ_{xy}^A). (f) Scaling behavior $\sigma_{yz}^A \propto \sigma_{yy}^2$ in CeAlSi, confirming an intrinsic AHE.

as W_1 , and the other 8 as W_2 . The W_1 nodes are 80 – 120 meV away from E_F but the W_2 nodes lie within 25 meV of the E_F , see Sec. M5 in Supplementary Material for details. All W_1 and W_2 Weyl fermions exhibit linear energy dispersions in all k -directions, suggesting that CeAlSi is a type-I WSM (see Appendix D.6 for details). This is different from the case of the related material CeAlGe that hosts both type-I and type-II Weyl nodes [72, 181] driven by the stronger spin-orbit coupling of Ge and the slightly different Wyckoff site coordinates. Note that the Weyl nodes in CeAlSi result from a broken inversion symmetry (\mathcal{I}) and the effect of breaking the time-reversal symmetry (\mathcal{T}) at $T < T_C$ is to shift the positions of the Weyl nodes in the BZ (Fig. 4.9(d)) [32, 72]. CeAlSi is thus a new FM WSM, in sharp contrast to the centrosymmetric systems such as $\text{Co}_3\text{Sn}_2\text{S}_2$ [34, 193], Fe_3GeTe_2 [69], and the Heusler alloys [203] where the Weyl nodes result from the broken \mathcal{T} .

We calculated the anomalous Hall conductivity (AHC) along the easy (σ_{yz}^A) and hard (σ_{xy}^A) axes as a function of the Fermi energy in Fig. 4.9(e) [68]. Magnitude of the theoretical AHC along the easy axis in Fig. 4.9(e) is comparable to the corresponding experimental values ($\sigma_{xy}^A = \rho_{yx}^A / \rho_{xx}^2$; $\rho_{yx}^A = \rho_{yx} - R_0 H$) [77, 102] in Fig. 4.9(f). The scaling behavior between σ_{yz}^A and σ_{yy}^2 (Fig 4.9(f)) indicates the presence of intrinsic and extrinsic contributions to the AHE [61], where the y-intercept codes the intrinsic contribution and the scaling with σ_{yy}^2 represents the extrinsic contribution[77, 102]. Note that, according to the DFT, we do not expect an AHC ($\sigma_{xy}^A = 0$) along the magnetic hard-axis $H \parallel c$. Therefore, the observation of a loop-shaped Hall signal with $H \parallel c$ is a novel electromagnetic response as discussed further below.

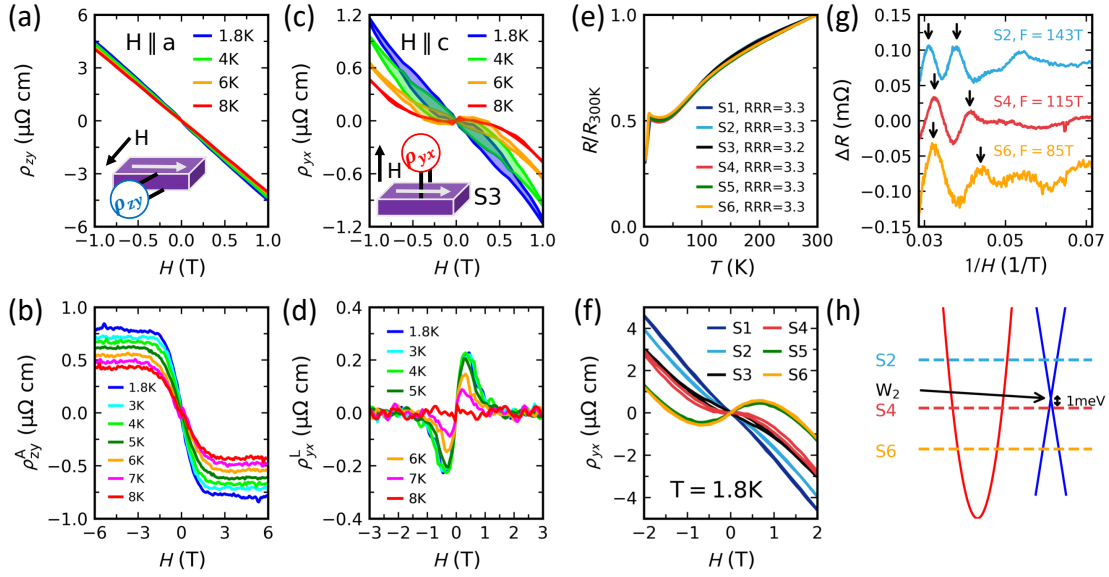


Figure 4.10: Anisotropic AHE of CeAlSi and its E_F dependence revealed by QO. (a) Hall resistivity ρ_{zy} measured at several temperatures with the field along the magnetic easy axis ($H \parallel a$). (b) Anomalous Hall resistivity ρ_{zy}^A derived from ρ_{zy} . (c) Hall resistivity ρ_{yx} measured at several temperatures with the field along the hard axis ($H \parallel c$). (d) Loop Hall resistivity ρ_{yx}^L derived from ρ_{yx} . (e) Normalized resistivity plotted as a function of temperature in samples S1-S6 with similar residual resistivity ratios. (f) Hall resistivity ρ_{yx} of samples S1-S6 measured at $T = 1.8$ K. (g) QOs in samples S2, S4, and S6, showing the evolution of the oscillation period. (h) Schematic band structure of CeAlSi illustrating an electron band, a Weyl crossing, and the Fermi levels of samples S2, S4 and S6. The decreasing QO frequency seen in panel (g) originates from the electron pocket (left) as the Fermi level shifts in samples S2, S4 and S6.

4.2.6 Anisotropic Anomalous Hall Effect

CeAlSi displays two different anomalous Hall responses when measured under in-plane (easy-axis) and out-of-plane (hard-axis) magnetic fields; such a concurrence is quite unusual and has been reported only in few cases [204]. We start by examining the Hall resistivity ρ_{zy} as a function of the in-plane field $H\|a$ (Fig. 4.10(a)). We separate the conventional and anomalous Hall signals by fitting the data at $H > 1$ T to $\rho_{zy} = R_0H + \rho_{zy}^A$. The conventional Hall effect (R_0H) has a slope $R_0 = -3.9 \mu\Omega\text{cmT}^{-1}$ corresponding to a small electron concentration $n_e = -1.6 \times 10^{20} \text{ cm}^{-3}$ (0.0003 electrons per unit cell), consistent with the small value of DOS at the E_F in Fig. 4.9(b). The anomalous Hall resistivity ρ_{zy}^A is plotted as a function of field in Fig. 4.10(b). Note that ρ_{zy}^A does not exactly follow the magnetization (Fig. 1D) like other conventional AHE materials, which is expected in systems with noncollinear spin texture such as $\text{Pr}_2\text{Ir}_2\text{O}_7$ [205, 206]. The anomalous Hall conductivity calculated from $\sigma_{yz}^A = \rho_{zy}^A / \rho_{xx}^2$ is plotted in Figs. 4.7(e) and 4.9(g). Magnitude of σ_{yz}^A is in agreement with the DFT results in Fig. 4.9(e).

Next, we discuss the Hall resistivity ρ_{yx} as a function of the out-of-plane field $H\|c$ (hard-axis) in Fig. 4.10(c), where an unusual loop is observed. This loop corresponds to different traces of $\rho_{yx}(H)$ between the field sweeps in the positive and negative directions (arrows in Fig. 4.10(c)). It extends over a region of ± 2 T, two orders of magnitude larger than the magnetic coercive field (70 Oe, inset of Fig. 4.7(d)). Notice that the loop-shaped Hall effect (LHE) does not scale with magnetization $M(H)$ and appears only when measured along the magnetic hard axis, unlike the AHE that saturates as the magnetization does and appears when the field is parallel to the easy axis. In order to study the temperature dependence of the LHE, we subtract the positive field sweep from the negative sweep and plot the loop Hall resistivity as $\rho_{yx}^L = \rho_{yx}(3 \rightarrow -3 \text{ T}) - \rho_{yx}(-3 \rightarrow 3 \text{ T})$ at several

temperatures (Fig. 4.10(d)). The loop Hall conductivity σ_{xy}^L in Figs. 4.7(e) and (f) was calculated as $\sigma_{xy}^L = \rho_{yx}^L / \rho_{xx}^2$, see Sec. M6 in Supplementary Material for details of the ρ_{xx} data.

In order to explore the link between the LHE and Weyl nodes, we measured samples with different separations between the Fermi level and the Weyl nodes. For this purpose, we selected six samples (S1-S6) with comparable residual resistivity ratios $RRR = R(300\text{K})/R(2\text{K})$ (Fig. 4.10(e)). Slight off-stoichiometry of Si and Al in our samples (see Appendix D.8) causes a shift of the Fermi level relative to the Weyl nodes [86, 122]. Variations in the E_F between the samples is evident in Fig. 4.10(f), which shows three categories of Hall curves: a linear ρ_{yx} with negative slope in samples S1 and S2; a moderately nonlinear ρ_{yx} with negative slope at all fields in S3 and S4; and, a strongly nonlinear ρ_{yx} with positive slope at low fields and negative slope at high fields in S5 and S6. Since the slope of ρ_{yx} is related to the sign of charge carriers, we adduce that E_F crosses only electron pockets in samples S1 and S2, nearly crosses another hole pocket in S3 and S4, and crosses both the electron and hole pockets in S5 and S6 as illustrated in Fig. 4.10(h). The LHE is observed only in S3 and S4 where the E_F lies near the crossing of electron and hole bands, i.e. near the Weyl node (Fig. 4.10(h)).

In order to confirm the scenario of Fig. 4.10(h), we used Schubnikov-de Haas (SdH) oscillations to locate the E_F with respect to the Weyl nodes along the lines of prior work on Weyl and magnetic semimetals [99, 123]. Figure 4.10(g) shows quantum oscillations for magnetic field between 15 and 33 T in samples S2, S4, and S6. The frequency of SdH oscillations, $F = A \left(\frac{\hbar}{2\pi e} \right)$, is proportional to the extremal orbit area A , and it will change as we shift the E_F in the band structure. The E_F for each sample can then be pinned down by matching experimental and theoretical frequencies of the electron pocket (the left portion in Fig. 4.10(h)). Through such an analysis, we obtain E_F values for samples S2, S4, and S6 to

lie 32, 23, and 12 meV above the DFT-calculated value, respectively; see Sec. M8 of Supplementary Material for details. When we compare these E_F values to the energies of Weyl nodes, we find that all Weyl nodes lie away from the E_F in samples S2 and S6, but a set of W_2^2 Weyl nodes is located within 1 meV of the E_F in sample S4, as illustrated in Fig. 4.10(h). Thus, we conclude that the LHE is observed only in samples where the E_F nearly crosses the Weyl nodes.

4.2.7 Outlook

In summary, CeAlSi is a unique noncentrosymmetric FM-WSM with an in-plane noncollinear FM order and novel anisotropic anomalous Hall responses along the easy and hard magnetic axes. In particular, CeAlSi exhibits the LHE which appears when the applied field lies along the hard axis. The LHE does not scale with either the field or the magnetization and is deeply connected with the Weyl nodes. The LHE is distinct from the THE [185–187] because the magnetic structure of CeAlSi may not support spin chirality or a skyrmion phase. In order to gain insight into the LHE in CeAlSi, we consider $\text{Nd}_2\text{Ir}_2\text{O}_7$, which also exhibits loop-shaped signals in magnetoresistance and Hall resistivity [207, 208]. $\text{Nd}_2\text{Ir}_2\text{O}_7$ hosts an all-in-all-out magnetic order of null spin chirality and requires an explanation other than the THE for its loop responses. Recently, it was proposed that $\text{Nd}_2\text{Ir}_2\text{O}_7$, despite having an insulating ground state, is very close to a WSM phase and that slight doping or external pressure will turn it into a WSM [171, 209, 210]. As a result, topological Fermi arcs in $\text{Nd}_2\text{Ir}_2\text{O}_7$ projected from the Weyl nodes on the magnetic domain walls interact to form exotic surface states (SSs); these topological Fermi-arc-induced (FAI) SSs survive the annihilation of Weyl nodes in the insulating regime [211]. The FAI SSs have been mapped out in $\text{Nd}_2\text{Ir}_2\text{O}_7$ by impedance spectroscopy [212], and can serve as special conducting channels responsible for the anomalous loop responses [207, 208, 211].

Keeping the preceding discussion of the FAI SSs in mind, we compare and contrast $\text{Nd}_2\text{Ir}_2\text{O}_7$ and CeAlSi to gain insight into the origin of the LHE in CeAlSi as follows.

1. $\text{Nd}_2\text{Ir}_2\text{O}_7$ is an overall AFM system with an all-in-all-out magnetic order, whereas CeAlSi hosts a non-collinear FM order. FAI SSs, however, only require the presence of the magnetic domain walls and the proximity of a WSM phase, and can thus be expected also in CeAlSi .
2. Although $\text{Nd}_2\text{Ir}_2\text{O}_7$ is insulating whereas CeAlSi is semimetallic, FAI SSs can exist in both materials. In $\text{Nd}_2\text{Ir}_2\text{O}_7$, FAI SSs are remnant traces of the Fermi arcs in the system before it becomes insulating, while in CeAlSi , they are the Fermi arcs connecting the bulk Weyl nodes.
3. The loop response in $\text{Nd}_2\text{Ir}_2\text{O}_7$ appears in both magnetoresistance (ρ_{xx}) and Hall resistivity ρ_{yx} , whereas in CeAlSi it only appears in ρ_{yx} . Generally, $\rho_{xx} \sim \sum_i^n \frac{\sigma_i}{1+\mu_i^2 B^2}$, where the summation extends over all conducting bands. Since $\sigma_i = n_i e_i \mu_i$ is always positive, ρ_{xx} is dominated by the bands with large carrier densities n . Since $\text{Nd}_2\text{Ir}_2\text{O}_7$ is insulating, the FAI SSs provide the only conducting channels and dominate ρ_{xx} and lead to the loop-shaped behavior. CeAlSi , in contrast, is metallic and its topological SSs fail to show a loop response in ρ_{xx} because the small density of states associated with these SSs is overwhelmed by the contribution from the bulk bands. On the other hand, note that $\rho_{yx} \sim \sum_i^n \frac{\sigma_i \mu_i}{1+\mu_i^2 B^2}$ and it can, therefore, be either positive or negative depending on the sign of the carriers. In $\text{Nd}_2\text{Ir}_2\text{O}_7$, the FAI SSs being the only carriers, they also drive ρ_{yx} and yield a loop response. In CeAlSi , the electron and hole (bulk) contributions to ρ_{yx} nearly cancel (Fig. 4.9(c)) and, as a result, the topological SSs control the behavior of ρ_{yx} and drive its loop response in CeAlSi . This argument is consistent with

our quantum oscillation results, which reveal an enhanced SS contribution (LHE) in the CeAlSi samples in which the Fermi energy lies close to the Weyl nodes.

CeAlSi will not only be amenable to ARPES studies due to its metallicity but it will also be suitable for device engineering and tuning of the Fermi arcs [213]. CeAlSi would thus provide an interesting materials platform for exploring the physics of Weyl nodes and how these nodes are connected with the exotic electromagnetic responses of topological materials¹³.

¹³This section is largely based on the publication “*A new noncollinear ferromagnetic Weyl semimetal with anisotropic anomalous Hall effect*” [78]. We thank Chunli Huang, Hiroaki Ishizuka, Bohm-Jung Yang and Ying Ran for helpful discussions. F.T. acknowledges funding by the National Science Foundation under Award No. NSF/DMR-1708929. The work at Northeastern University was supported by the US Department of Energy (DOE), Office of Science, Basic Energy Sciences grant number DE-SC0019275 and benefited from Northeastern University’s Advanced Scientific Computation Center (ASCC) and the NERSC supercomputing center through DOE grant number DE-AC02-05CH11231. Neutron scattering was supported as part of the Institute for Quantum Matter, an Energy Frontier Research Center funded by the U.S. Department of Energy, Office of Science, Basic Energy Sciences under Award No. DE-SC0019331. A portion of this research used resources at the High Flux Isotope Reactor and Spallation Neutron Source, a DOE Office of Science User Facility operated by the Oak Ridge National Laboratory. The National High Magnetic Field Laboratory is supported by National Science Foundation through NSF/DMR-1644779 and the State of Florida. The work by I.S. was in part supported by the US Department of Defense, and the US State of Connecticut. B.X. and J.F. were supported through graduate assistantship provided by the University of Connecticut’s College for Liberal Arts and Sciences. We acknowledge the support of the National Institute of Standards and Technology, U.S. Department of Commerce. Certain commercial equipment, instruments, or materials (or suppliers, or software, etc.) are identified to foster understanding. Such identification does not imply recommendation or endorsement by the National Institute of Standards and Technology, nor does it imply that the materials or equipment identified are necessarily the best available for the purpose.

APPENDICES

APPENDIX A

Supplementary Material for LaAs

A.1 XMR and Residual Resistivity Ratio

It has been shown in prior works [26] that XMR magnitude depends on the residual resistivity ratio (RRR). We have characterized about 10 LaAs samples and we never observed RRR in excess of 150. However, for a comparable RRR, LaAs samples still show smaller XMR compared to LaBi. Figure A.1 compares the temperature dependence of the normalized resistivity between a LaAs and a LaBi sample with comparable RRR. Note the qualitative difference between the two materials where $\rho(2\text{K}) > \rho(300\text{K})$ in LaBi but $\rho(2\text{K}) < \rho(300\text{K})$ in LaAs. Note that magnetoresistance is the ratio of $R(B)/R(B = 0)$ whereas RRR is a $B = 0$ quantity. Figure A.1 shows that the difference in XMR between the two compounds is a finite-field effect not a zero-field effect.

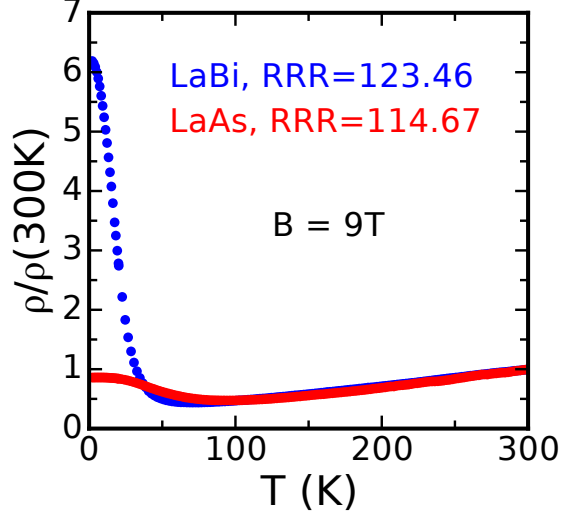


Figure A.1: Normalized resistivity of LaAs and LaBi. Normalized resistivity $\rho/\rho(300\text{K})$ at $B = 9$ T plotted as a function of temperature in a LaAs and a LaBi sample with comparable residual resistivity ratios (RRR).

A.2 Multiband Fit

The general expressions for the longitudinal and transverse resistivity (ρ_{xx} and ρ_{xy}) of a multiband system are [83]:

$$\rho_{xx} = \frac{\sum_i^n \frac{\sigma_i}{1+\mu_i^2 B^2}}{\left(\sum_i^n \frac{\sigma_i}{1+\mu_i^2 B^2}\right)^2 + \left(\sum_i^n \frac{\sigma_i \mu_i}{1+\mu_i^2 B^2}\right)^2 B^2} \quad (\text{A.1})$$

$$R_H = \rho_{xy}/B = \frac{\left(\sum_i^n \frac{\sigma_i \mu_i}{1+\mu_i^2 B^2}\right)}{\left(\sum_i^n \frac{\sigma_i}{1+\mu_i^2 B^2}\right)^2 + \left(\sum_i^n \frac{\sigma_i \mu_i}{1+\mu_i^2 B^2}\right)^2 B^2}, \quad (\text{A.2})$$

where $i = 1, 2, \dots, n$ is the band index, σ is conductivity, μ is mobility, and B is the magnetic field. The Fermi surface of LaAs (see Figs. 3.3(a,b)) consists of two hole pockets (β and γ) and a triplet of electron pockets (α) in the first Brillouin zone. Assuming the field direction is along $[001]$, the electron pocket in the k_z direction (α_1) will have different extremal area than the other two electron pockets (α_2) which lie in the k_x and k_y directions. The cross section of α_1 is a small circle at the Brillouin zone Z point while that of α_2 is a larger ellipse at X and Y points.

Table A.1: Carrier densities and mobilities of LaAs. Carrier density n and mobility μ for each band are computed from the multiband fits. The ratio of densities is nearly one $n_e/n_h = (3 \times 1.40)/(2.05 + 2.13) = 1.005$. The ratio of mobilities $\bar{\mu}_e/\bar{\mu}_h = 12.7$ is of order ten.

Band	n (cm ⁻³)	μ (cm ² V ⁻¹ s ⁻¹)
α_1	1.40×10^{19}	64118
α_2	1.40×10^{19}	12855
β	2.05×10^{19}	1462
γ	2.13×10^{19}	4602

Since both orbits belong to the same pocket (α), their contributions to Eqs. A.1 and A.2 appear with the same carrier concentration but with different mobilities. As a result, Eqs. A.1 and A.2 sum over contributions from α_1 , $2\alpha_2$, β and γ .

After setting up the model, we fit Eq. A.1 and A.2, with n up to 5 as explained in the previous paragraph, to the ρ_{xx} and ρ_{xy} data *simultaneously* to extract only one set of parameters (carrier concentrations and mobilities). According to Eq. A.1 and A.2, if the multiband model works, one single set of parameters should be able to describe the behavior of ρ_{xx} and ρ_{xy} simultaneously. Multiband fits are often mistreated in the literature. If ρ_{xx} data is fitted to Eq. A.1 without checking how the resultant fitting parameters behave in describing ρ_{xy} , the analysis would be incomplete and questionable. The parameters derived by fitting only ρ_{xx} data, when substituted into the formula of ρ_{xy} , may largely disagree with the experimental ρ_{xy} data.

The results of our multiband fit to the transport data are summarized in Table A.1. The ratio $n_e/n_h = 1.005$ from multiband fits to the transport data agrees with $n_e/n_h = 1.01$ from quantum oscillation experiments confirming the perfect electron-hole compensation in LaAs similar to LaSb and LaBi.

Table A.2: Calculations of Fermi volumes. Carrier concentrations are calculated for the α , β , and γ pockets from the quantum oscillations data in this work (LaAs) and Ref. [147] (LaSb/LaBi). Three different models are used to estimate the Fermi volume of γ as described in the text. From these concentrations, the ratio n_e/n_h is reported for the three lanthanum monopnictides.

sample/model	n_α (cm ⁻³)	n_β (cm ⁻³)	n_γ (cm ⁻³)	n_e/n_h
LaAs/ave. spheres	1.55×10^{19}	9.37×10^{18}	3.66×10^{19}	1.01
LaAs/3 ellipsoids, a-b	1.55×10^{19}	9.37×10^{18}	3.97×10^{19}	0.95
LaAs/3 ellipsoids, a-a/2	1.55×10^{19}	9.37×10^{18}	3.26×10^{19}	1.11
LaSb/ave. spheres	6.98×10^{19}	5.33×10^{19}	1.73×10^{20}	0.93
LaSb/3 ellipsoids, a-b	6.98×10^{19}	5.33×10^{19}	1.86×10^{20}	0.87
LaSb/3 ellipsoids, a-a/2	6.98×10^{19}	5.33×10^{19}	1.59×10^{20}	0.99
LaBi/ave. spheres	1.28×10^{20}	9.00×10^{19}	3.38×10^{20}	0.89
LaBi/3 ellipsoids, a-b	1.28×10^{20}	9.00×10^{19}	3.61×10^{20}	0.85
LaBi/3 ellipsoids, a-a/2	1.28×10^{20}	9.00×10^{19}	3.19×10^{20}	0.94

A.3 Calculations of Fermi Volumes

We estimated the volume of each Fermi pocket in LaAs from quantum oscillation frequencies. α was treated as an ellipsoid and β was treated as a sphere, so there were no ambiguities in calculating their volumes from the extremal cross sections. Calculating the volume of the jack-shaped γ pocket requires some explanation. By varying the angle between the crystallographic a -axis and the applied magnetic field, we observed a maximal cross section A_{max} at $\theta = 0^\circ$ and 90° , as well as a minimal cross section A_{min} at $\theta = 45^\circ$ for the γ pocket as shown in Fig. 4(c). We used the values of A_{max} and A_{min} to estimate the carrier concentration of γ using three different models:

(i) Average of two spheres: A_{max} was treated as the cross section of a large sphere, A_{min} was treated as the cross section of a small sphere, and the γ pocket was assumed to have its volume as the average of the two.

(ii) Three a - b ellipsoids: A_{max} was treated as the superposition of two ellipses, with semi-major axis a and semi-minor axis b . A_{min} was treated as a single ellipse.

As a result, we calculated a and b through the following set of relations:

$$A_{max} = 2\pi ab - \pi b^2, \quad (\text{A.3})$$

$$A_{min} = \pi ab. \quad (\text{A.4})$$

After finding a and b , we calculated the volume of the γ pocket using:

$$V_\gamma = 3 \times \frac{4\pi}{3} ab^2 - 2 \times \frac{4\pi}{3} b^3. \quad (\text{A.5})$$

(iii) Three a - $a/2$ ellipsoids: This model was almost the same as the $a-b$ model by simply assuming $b = a/2$. As a result, a was calculated from

$$A_{max} = 2\pi a \frac{a}{2} - \pi \left(\frac{a}{2}\right)^2 = \frac{3\pi}{4} a^2, \quad (\text{A.6})$$

and the volume of γ pocket in this model was

$$V_\gamma = 3 \times \frac{4\pi}{3} a \left(\frac{a}{2}\right)^2 - 2 \times \frac{4\pi}{3} \left(\frac{a}{2}\right)^3 = \frac{2\pi}{3} a^3 \quad (\text{A.7})$$

This model was used to calculate the ratio n_e/n_h for LaSb in Ref. [24]. Once the volumes V_F of each pocket are calculated, we determined the carrier concentration for each pocket using:

$$n = \frac{V_F}{4\pi^3}, \quad (\text{A.8})$$

The ratio n_e/n_h was determined by considering three electron pockets (α), and two hole pockets (β and γ):

$$\frac{n_e}{n_h} = \frac{3n_\alpha}{n_\beta + n_\gamma}. \quad (\text{A.9})$$

Table A.2 summarizes the estimation of n_e/n_h using the three different methods in LaAs, LaSb, and LaBi. The precise ratio of n_e/n_h depends on the model, but

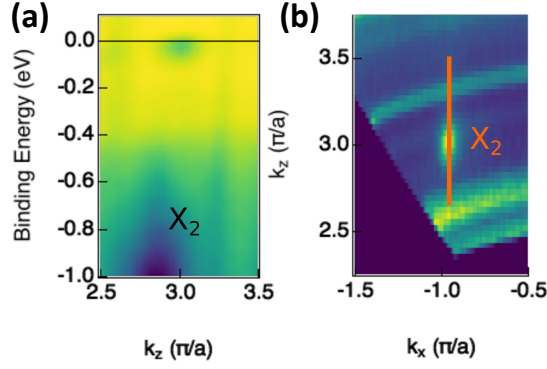


Figure A.2: k_z dispersion in LaAs. (a) k_z dispersion of the α pocket at X . The dispersion is consistent with bulk states and the gap between valence and conduction bands is persistent. There is no evidence of a surface state at X . (b) Constant energy cut of the α pocket at E_F . The orange line indicates the location of the dispersion cut in (a).

within each model, the three compounds are compensated with comparable ratio of electrons to holes.

A.4 ARPES: k_z Dispersion

In order to verify the bulk nature of the electronic states at X , we measured their dispersion in the k_z direction (along the sample normal). If a topological state was present it would be confined to the surface of the crystal. Due to this confinement in the real space coordinate z , the uncertainty principle dictates that k_z is a poor quantum number for these states and one would expect non-dispersive features in the k_z direction from these states. Our ARPES dispersions along the k_z direction in Fig. A.4 clearly show a lack of non-dispersive features, and the persistence of the gap between the conduction and valence bands. We therefore rule out the existence of topological surface states.

APPENDIX B

Supplementary Material for HoBi

B.1 Magnetoresistance with Different Field Directions

Figure B.1 compares the magnitude of magnetoresistance $\text{MR}(\%) = 100 \times [\rho(H) - \rho(0)]/\rho(0)$ with the field parallel to the crystallographic [001] and [110] directions. In both cases, the electrical current is perpendicular to the field. MR is large and of comparable magnitudes for both field directions. The data in Fig. B.1 and Fig. 3 in the main text are obtained from the same sample with a residual resistivity ratio $\text{RRR} = 127$.

B.2 Magnetization Data with Different Field Directions

The $M(H)$ data, dM/dH curves, and T - H phase diagrams are compared between three field directions $H \parallel [001]$, [110], and [111]. The first row shows the magnetization data, the second row shows dM/dH curves, and the third row compares the phase diagrams. Comparing the three $M(H)$ curves in Fig. B.2(d) reveals a magnetocrystalline anisotropy in HoBi. When $H \parallel [001]$, the saturated moment is twice as large as the other two field directions. The phase diagram with $H \parallel [110]$ and [111] are almost identical and have fewer MM transitions compared to the [001] direction.

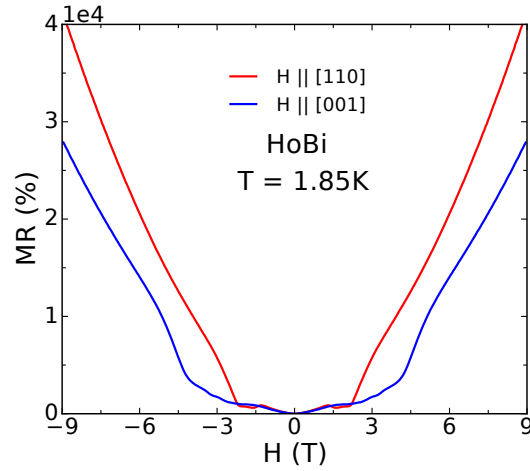


Figure B.1: Magnetoconductance of HoBi with $H||[001]$ and $[110]$ directions. Magnetoconductance (MR) is compared between two measurements on the same sample ($RRR = 127$) with $H||[001]$ (blue) and $[110]$ (red).

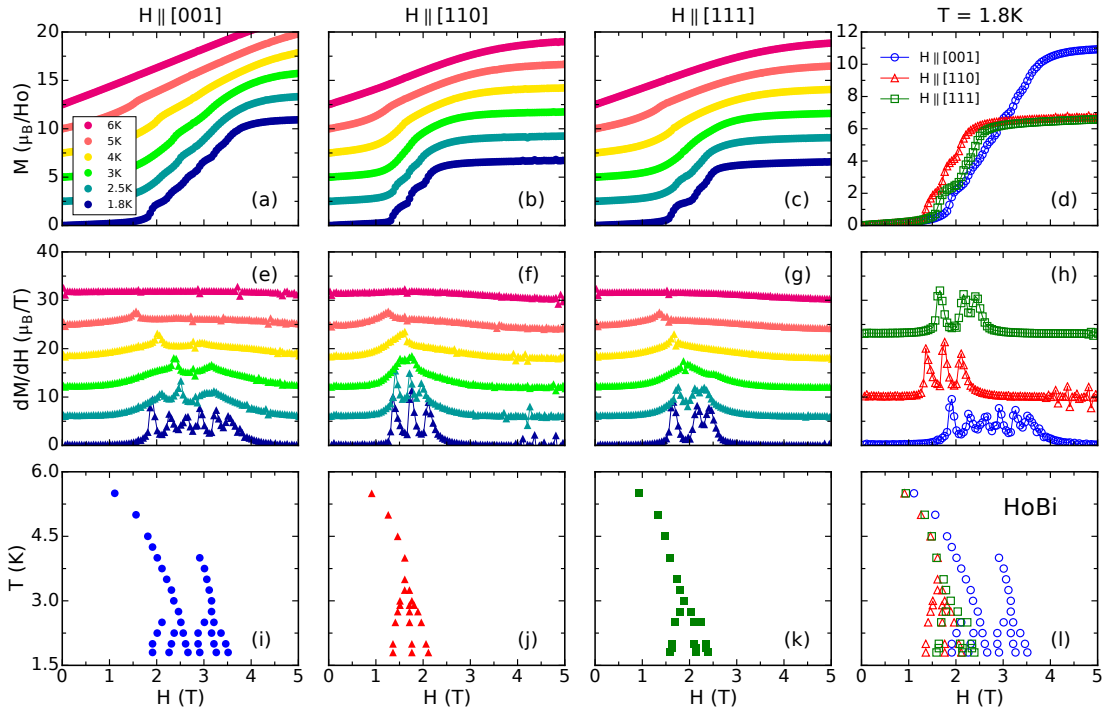


Figure B.2: Magnetization data with $H||[111]$, $[110]$, and $[001]$ directions. (a–c) Magnetization data of HoBi for $H||[001]$, $[110]$, and $[111]$. (d) Comparing the $M(H)$ curves along the three directions. (e–g) dM/dH curves for $H||[001]$, $[110]$, and $[111]$. (h) Comparing the dM/dH curves along the three directions. (i–k) Phase diagrams for $H||[001]$, $[110]$, and $[111]$. (l) Comparing the phase diagrams along the three directions.

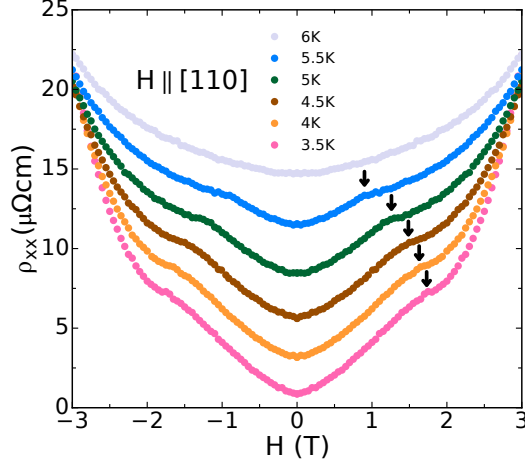


Figure B.3: Resistivity features and the AFM order. Resistivity is plotted as a function of field at $T > 3.3$ K in HoBi ($T_N = 5.75$ K). This figure is complementary to Fig. 3.7 in the main text. Arrows mark the boundary of the AFM phase as determined from the resistivity data.

B.3 Resistivity Features and the AFM Order

Figure B.3 shows the $\rho(H)$ curves from $H = -3$ to 3 T with field along the [110] direction at $3.3 < T < T_N$ in HoBi. At the AFM transition, a break appears in the slope of each $\rho(H)$ curve which eventually disappears above $T_N = 5.75$ K. The evolution of the AFM order with increasing field is marked by the arrows in Fig. B.3. The black points at $3.3 < T < T_N$ in Fig. 3(d) in the main text correspond to the position of the arrows in Fig. B.3.

B.4 Features in Transport, Magnetization and Neutron Data

Figure B.4 compares $\rho(H)$, $d\rho/dH$, $M(H)$, and the intensity of the (1, 1, 1) peak with $H \parallel [110]$ at low temperatures in HoBi. The onset of XMR is marked by a step-like increase of $d\rho/dH$ (black curve) at $H = 2.3$ T, above which, it shows a broad peak and eventually flattens. This behavior reflects a steep increase of $\rho(H)$ (blue circles) in the region $2.3 < H < 3.5$, followed by a less steep increase

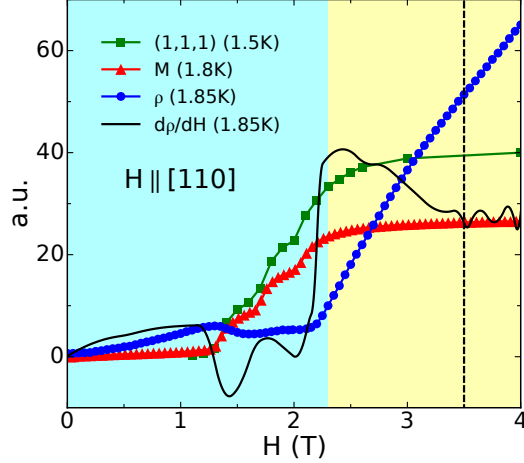


Figure B.4: Features in transport, magnetization and neutron data. A comparison is made for $\rho(H)$, $d\rho/dH$, $M(H)$, and the neutron diffraction intensity of $(1, 1, 1)$ order at $T < 2$ K with $H \parallel [110]$. The MM transitions are finished by 2.3 T but the $M(H)$ curve does not saturate until about 3.5 T (vertical dashed line). Similarly, the intensity of the $(1, 1, 1)$ diffraction peak does not saturate until about 3.5 T. Here, we use the $(1, 1, 1)$ intensity to parametrise the FM $(0, 0, 0)$ order. $d\rho/dH$ shows a broad hump and $\rho(H)$ shows an initial boost in XMR in the region $2.3 < H < 3.5$ T.

above 3.5 T. Both the magnetization $M(H)$ curve and the $(1, 1, 1)$ neutron peak intensity show a slow increase in the region $2.3 < H < 3.5$ T before they saturate above 3.5 T marked by the vertical dashed line. Note that the $(1, 1, 1)$ peak is a subset of FM $(0, 0, 0)$ and represents the polarization of spins in the FM phase.

B.5 Band Structures Calculated by Different U

Figure B.5 compares the band structure of HoBi calculated with different U values. A change of 0.02 Ry has a dramatic effect on the smallest hole pocket at Γ (the green band in Fig. B.5). This pocket has been particularly helpful to restrict our choice of U in the DFT calculation. The band structure in Fig. B.5(b) with $U = 0.52$ Ry contains the small hole pocket at Γ with a calculated frequency $f = 243$ T that matches the measured frequency $f = 280$ T from the SdH experiments. Figure B.5(a) shows that decreasing U by a small amount will eliminate this small

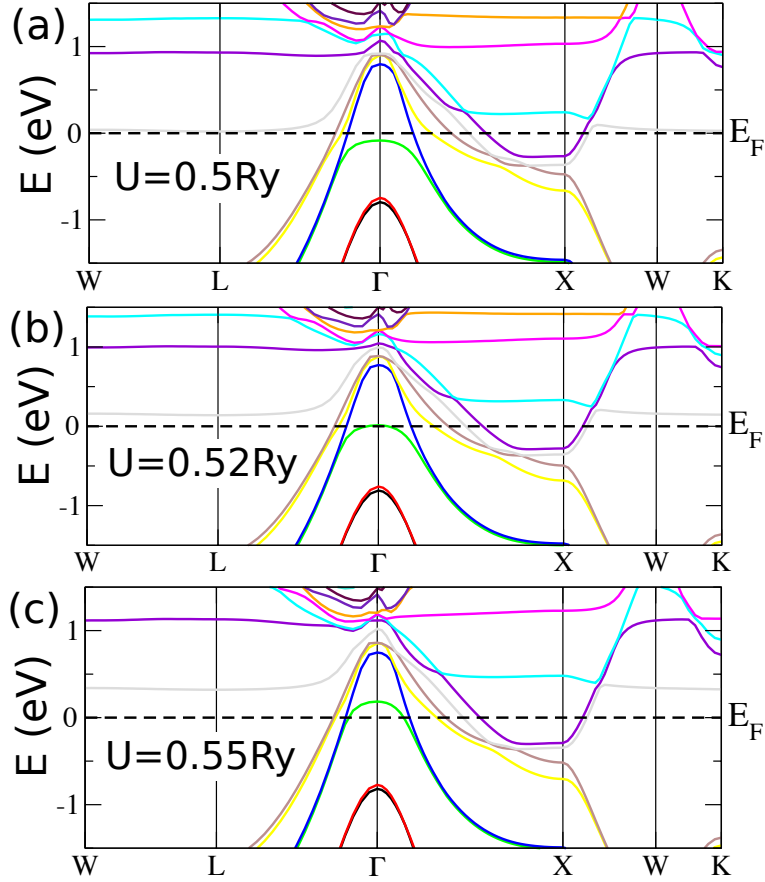


Figure B.5: Band structures calculated by different U in HoBi. Band structure of HoBi is calculated by PBE+SOC+ U using (a) $U = 0.50$ Ry (6.803 eV), (b) $U = 0.52$ Ry (7.075 eV), and (c) $U = 0.55$ Ry (7.483 eV). Notice the sensitivity of the green hole band at Γ to the choice of Hubbard U . The Fermi momentum corresponding to this small Fermi surface matches the frequency of quantum oscillations when $U = 0.52$ Ry.

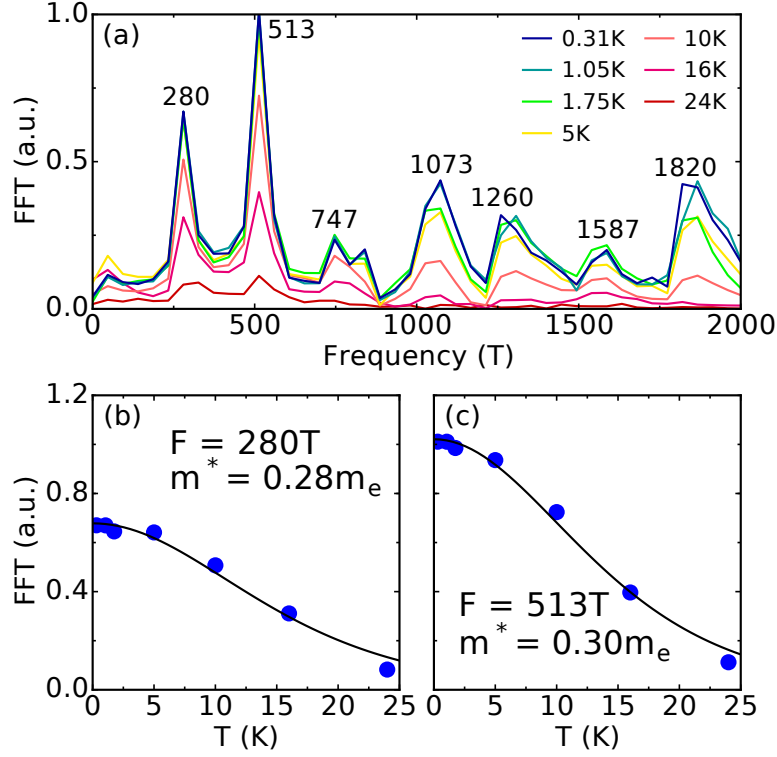


Figure B.6: Extraction of effective masses in HoBi. (a) Fourier transform of SdH oscillations at several temperatures between 0.31 and 24 K. The oscillation amplitudes damp with temperature according to the Lifshitz-Kosevich expression (Eq. B.1). A fit to this formula is used to obtain the effective mass of carriers on the Fermi surfaces with frequencies (b) 280 T and (c) 513 T. This analysis is less accurate in peaks at higher frequencies that could overlap with harmonics of the low-frequency peaks.

hole pocket. Figure B.5(c) shows that increasing U by a small amount will increase the size of this pocket to 781 Hz which is inconsistent with the experimental result. The band structure in Fig. B.5(b) is presented in Fig. 4(a) in the main text and used for the discussion around DFT calculations and SdH oscillations. Figure B.5(b) is also in qualitative agreement with the results of a recent ARPES experiment on HoSb [43].

B.6 Effective Mass

We measured electrical resistance in high magnetic fields to resolve SdH oscillations. As shown in Fig. 3.8(b) of the main text, the oscillations do not appear until 20 T which makes high-field experiments necessary. Measurements of electrical resistance were performed at seven temperatures from 0.31 to 24 K in a ^3He fridge inside a DC Florida-Bitter magnet. A smooth background was subtracted from $R(T)$ data at each temperature to resolve SdH oscillations that are periodic in $1/H$. The oscillation data, after subtraction, were Fourier transformed to obtain the frequencies corresponding to the extremal orbit areas of the Fermi surfaces. These frequencies are listed in Table 1 in the main text and compared to the results of DFT calculations. Figure B.6(a) shows the damping of SdH frequencies with temperature. The damping factor can be obtained by fitting the FFT peak amplitudes to a Lifshitz-Kosevich (LK) formula [112, 113] according to:

$$R_L = \frac{X}{\sinh(X)} \quad , \quad X = \frac{\alpha T m^*}{H} \quad (\text{B.1})$$

where R_L is the damping factor and $\alpha = 2\pi^2 k_B m_e / e\hbar$ is a constant made of Boltzmann factor k_B , bare electron mass m_e , electron charge e , and reduced Planck constant \hbar . The effective mass m^* is calculated in units of m_e . Figures B.6(b,c) show the results of fits to the LK formula for the two smallest frequencies at 280 and 513 T. The results of a similar analysis on other Fermi surfaces are given in Table 1 in the main text. These results are in acceptable agreement with the calculated frequencies from DFT.

APPENDIX C

Supplementary Material for $\text{PrAlGe}_x\text{Si}_{1-x}$

C.1 EDX Results

We performed an EDX analysis to evaluate the Si-content (x) in $\text{PrAlGe}_{1-x}\text{Si}_x$ accurately. The first column in Table C.1 shows the mole ratio used in the crystal growth process ($\text{Pr:Al:Ge:Si} = 1:10:y:1 - y$). The last column gives the final Si-content (x) in various $\text{PrAlGe}_{1-x}\text{Si}_x$ crystals. For $y = 0, 0.5$ and 1 , $x = y$. For $y = 0.75$ and 0.9 , $x = 0.7$ and 0.85 , respectively.

C.2 Rietveld Refinement

To extract the lattice parameters for various compositions, we performed Rietveld X-ray refinement for all cases, and the results are given in Fig. C.1. The

Table C.1: EDX results for various $\text{PrAlGe}_{1-x}\text{Si}_x$ samples. The atomic weights derived from EDX spectra are normalized to Pr content. These results are subject to an error of ± 0.05 .

y	Pr	Al	Ge	Si	Si/(Si+Ge) (x)
0	1.00	1.00	0.00	1.07	1.00
0.5	1.00	0.90	0.47	0.49	0.51
0.75	1.00	1.08	0.37	0.82	0.69
0.9	1.00	0.95	0.15	0.87	0.85
1	1.00	0.82	0.00	0.86	1.00

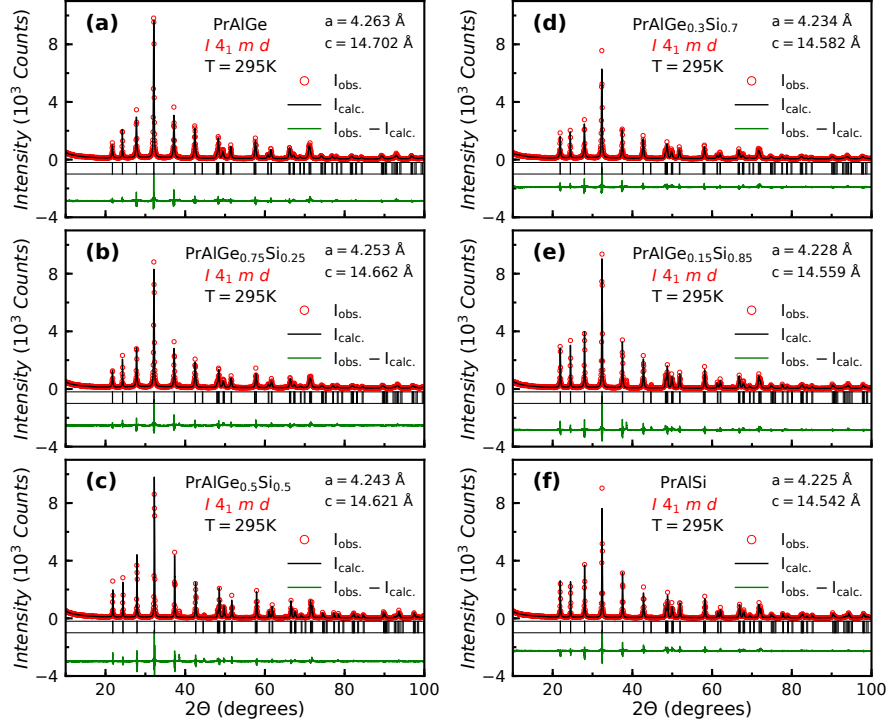


Figure C.1: Rietveld refinement of powder XRD data for $\text{PrAlGe}_{1-x}\text{Si}_x$.

calculated X-ray diffraction patterns match well the corresponding experimental patterns. Fig. 4.1 shows that the extracted lattice parameters evolve continuously across the $\text{PrAlGe}_{1-x}\text{Si}_x$ family.

C.3 Second Harmonic Generation

The SHG data were fit to functions appropriate for four different experimental configurations: incoming polarization rotating, output polarizer fixed with polarization parallel to the crystalline $[010]$ axis, denoted by $I_H(\phi)$; incoming polarization rotating, output polarizer fixed with polarization parallel to the $[10\bar{1}]$ axis, denoted by $I_V(\phi)$; incoming polarization rotating, outgoing polarizer rotated at 0° angle relative to the incoming polarization, denoted by $I_{\parallel}(\phi)$; and incoming polarization rotating, outgoing polarizer rotated with polarization axis at 90° angle relative to the incoming polarization, denoted by $I_{\perp}(\phi)$. In the electric dipole ap-

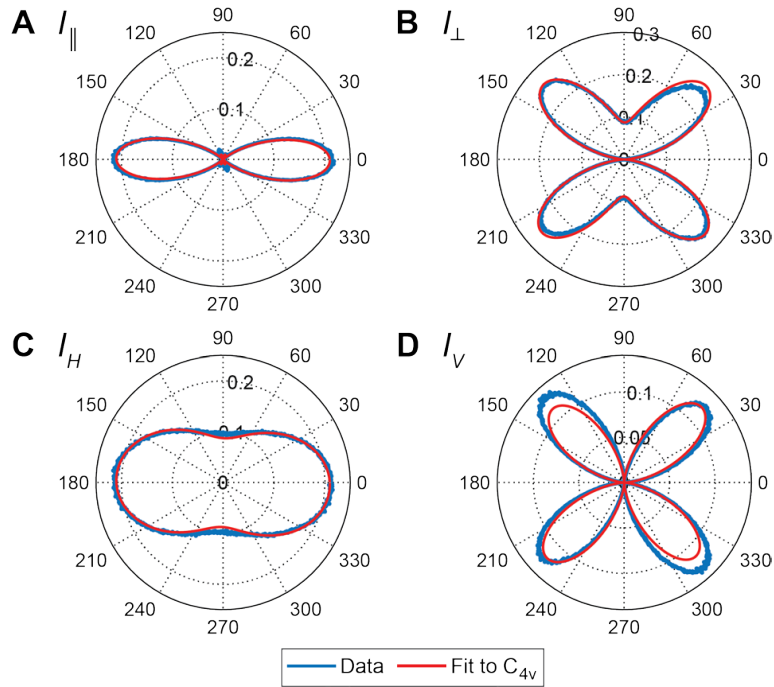


Figure C.2: Second harmonic generation data of $\text{PrAlGe}_{1-x}\text{Si}_x$. The SHG data for incoming wavelength of 1500 nm, outgoing wavelength of 750 nm, and the corresponding fits to the bulk electric dipolar SHG in the C_{4v} point group as given by Eqs. [D.1-D.4] for (A) $I_{||}$, (B) I_{\perp} , (C) I_V , and (D) I_H .

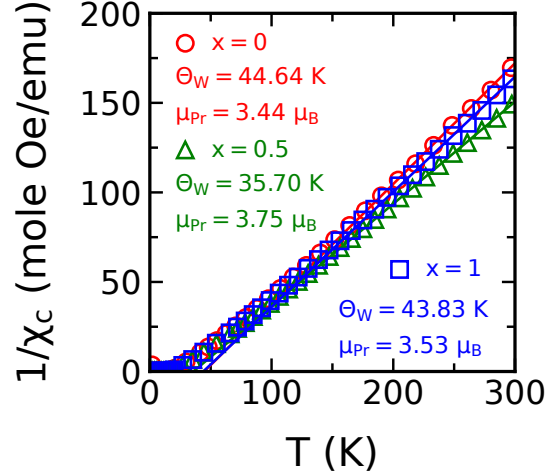


Figure C.3: Curie-Weiss analysis for $\text{PrAlGe}_{1-x}\text{Si}_x$ for $x = 0, 0.5,$ and $1.$

proximation, the mathematical forms of the various responses for the $[101]$ crystal face in the $I4_1md$ space group (C_4v point group) are given by

$$I_{\parallel}^{eee}(\phi) = \frac{1}{32} \cos^2(\phi) [(-2\chi_{xxz}^{eee} - \chi_{zxx}^{eee} + \chi_{zzz}^{eee}) \cos(2\phi) + 6\chi_{xxz}^{eee} + 3\chi_{zxx}^{eee} + \chi_{zzz}^{eee}]^2 \quad (\text{C.1})$$

$$I_{\perp}^{eee}(\phi) = \frac{1}{8} \sin^2(\phi) [(-2\chi_{xxz}^{eee} + \chi_{zxx}^{eee} + \chi_{zzz}^{eee}) \cos^2(\phi) + 2\chi_{zxx}^{eee} \sin^2(\phi)]^2 \quad (\text{C.2})$$

$$I_H^{eee}(\phi) = \frac{1}{8} [(2\chi_{xxz}^{eee} + \chi_{zxx}^{eee} + \chi_{zzz}^{eee}) \cos^2(\phi) + 2\chi_{zxx}^{eee} \sin^2(\phi)]^2 \quad (\text{C.3})$$

$$I_V^{eee}(\phi) = 2 [\chi_{xxz}^{eee} \sin(\phi) \cos(\phi)]^2 \quad (\text{C.4})$$

The data were fit to expressions [D.1-D.4] accounting for a rotation of the sample axes relative to the laboratory x-axis to produce excellent fits to the data, as seen in Fig. C.2. The competing space group assignment $I4_1/amd$ (point group D_{4h}) is centrosymmetric and thus should not produce as strong of a SHG response as we have shown here.

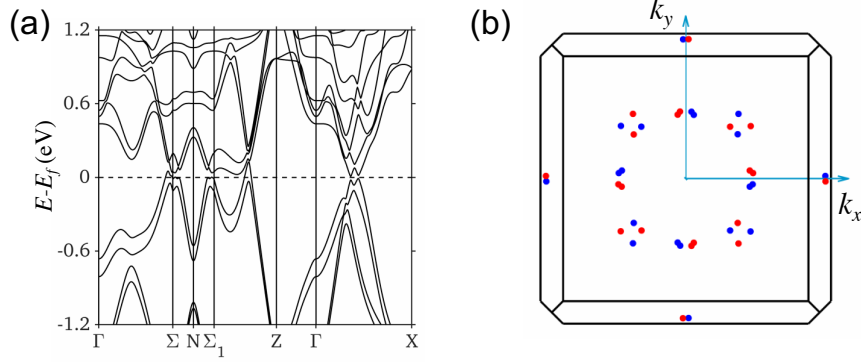


Figure C.4: DFT calculations for $\text{PrAlGe}_{0.5}\text{Si}_{0.5}$. (a) Band structure and (b) distribution of Weyl nodes in the momentum space in $\text{PrAlGe}_{1-x}\text{Si}_x$ for $x = 0.5$. We get 40 Weyl nodes in the Brillouin zone similar to the end members PrAlGe and PrAlSi .

C.4 Curie-Weiss Analysis

Curie-Weiss analysis was performed on $\text{PrAlGe}_{1-x}\text{Si}_x$ for $x = 0, 0.5$ and 1 . The Curie-Weiss fit was made to the high-temperature data ($T > 150$ K) to extract the Weiss temperature Θ_W and the effective moment μ_{Pr} (Fig. C.3). Based on this analysis, different compositions of $\text{PrAlGe}_{1-x}\text{Si}_x$ family are found to have similar values of Θ_W and μ_{Pr} .

C.5 Topological Electronic Structure of $\text{PrAlGe}_{0.5}\text{Si}_{0.5}$

The calculated band structure of $\text{PrAlGe}_{1-x}\text{Si}_x$ for $x = 0.5$ in the presence of SOC is shown in Fig C.4(a). It has both electron and hole band crossings at the Fermi level, which are similar to those in the end members PrAlGe and PrAlSi . There are 40 Weyl nodes whose Brillouin zone distribution remains similar to that of $\text{PrAl}(\text{Ge},\text{Si})$ (see Fig C.4(b)). These results further show that the Weyl state remains robust with changes in Si concentration.

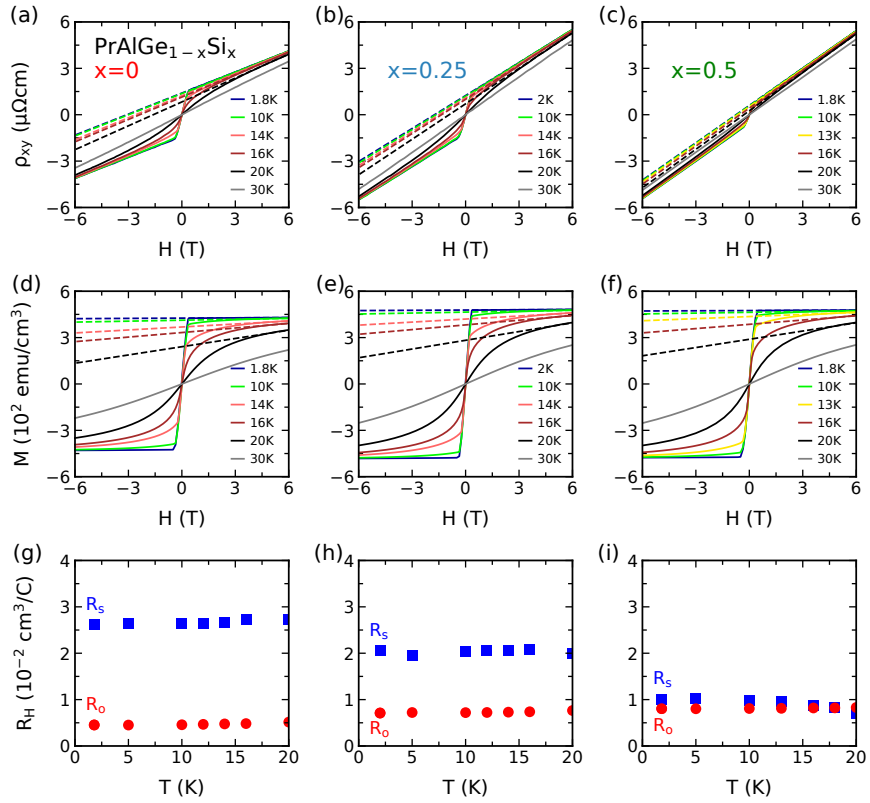


Figure C.5: Data used to extract R_0 and R_S in $\text{PrAlGe}_{1-x}\text{Si}_x$ compounds for $x \leq 0.5$. (a-c) ρ_{xy} measured at different temperatures. The y-intercepts of the fitting lines are extracted as ρ_{xy}^A . (d-f) Magnetization measured at different temperatures. Fitting lines are based on the high-field part of the data. (g-i) R_0 and R_S values at different temperatures.

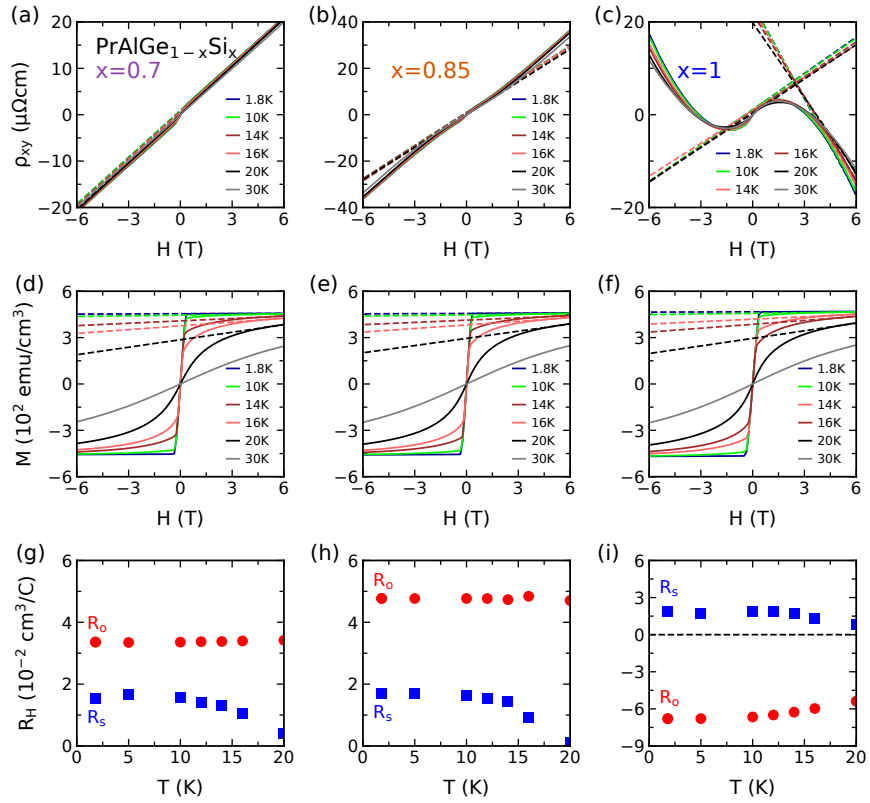


Figure C.6: Data used to extract R_0 and R_S in $\text{PrAlGe}_{1-x}\text{Si}_x$ compounds for $x > 0.5$. (a-c) ρ_{xy} measured at different temperatures. The y-intercepts of the fitting lines are extracted as ρ_{xy}^A . (d-f) Magnetization measured at different temperatures. Fitting lines are based on the high-field part of the data. (g-i) R_0 and R_S values at different temperatures.

C.6 The Analysis of R_0 and R_S

Here, we show all the data needed to extract R_0 and R_S values according to Eq. 4.1 in Figs. C.5 and C.6. Note that, for $x = 0.85$ and $x = 1$, ρ_{xy} is not linear at high fields. Thus, to extract ρ_{xy}^A for these two compositions, the data between $H = 0.5$ and 1 T were fitted to a straight line, the intercept of which at $H = 0$ T was extracted as ρ_{xy}^A . For other compositions, the data at $H > 4$ T were used for the fitting lines to extract ρ_{xy}^A . Slopes of these lines are reported as R_0 except for $x = 1$, where a second fitting line was made to the high-field data to capture the behavior of the ordinary Hall effect.

C.7 Quantum Oscillation and Anomalous Hall Conductivity

Results of QO experiments and the calculated AHCs are given in Fig. C.7. Note that to match the experimental and theoretical frequencies, the E_F in the calculations should be at 6 meV for PrAlSi. At 6 meV in Fig. C.7(d), the calculated AHC is about 300-400 $\Omega^{-1}\text{cm}^{-1}$ for PrAlSi. Since the calculation here only considers the contribution from Berry curvature, there could be a discrepancy as shown in the literature [106]. Overall, the magnitude of the calculated AHC is comparable to the experimental one.

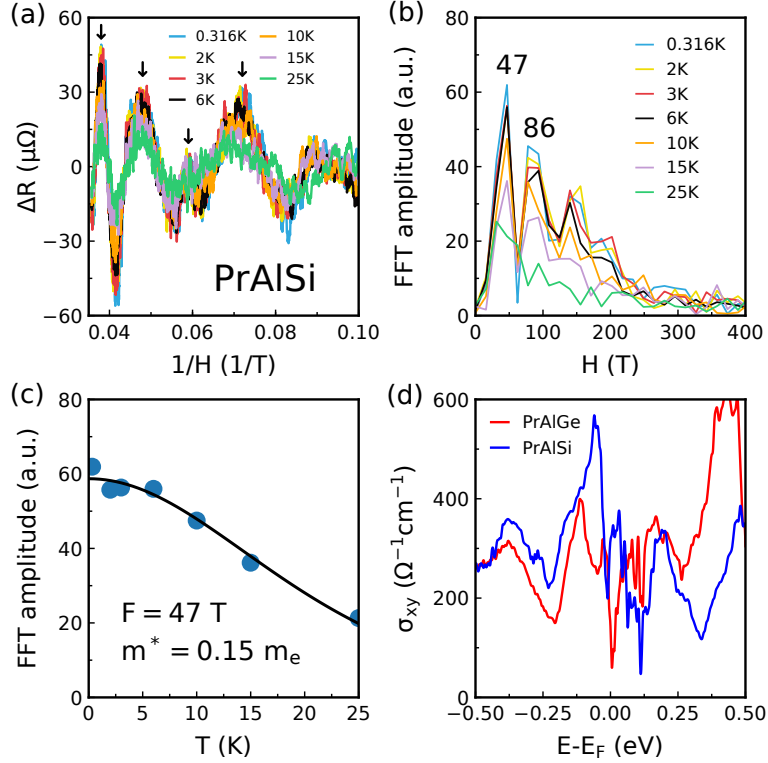


Figure C.7: Quantum oscillation and calculated anomalous hall conductivity of $\text{PrAlGe}_{1-x}\text{Si}_x$. (a) Shubnikov-de Haas oscillations in PrAlSi. The field was applied along c -axis. The arrows mark the peaks of the oscillations. (b) Fast Fourier transform (FFT) of the data shown in (a). (c) Effective mass extracted by the Lifshitz-Kosevich formula [113] for the Fermi surface corresponds to $F = 47$ T. (d) Calculated intrinsic AHC for PrAlGe and PrAlSi.

APPENDIX D

Supplementary Material for CeAlSi

D.1 Structural Analysis by X-ray and Neutron Diffraction

The noncentrosymmetric $I4_1md$ (#109) and centrosymmetric $I4_1/amd$ (#141) space groups are nearly indistinguishable in the powder X-ray diffraction. We compare the refinement of the powder X-ray data in these two space groups in Figs. D.1A,B and Table D.1 to show the difficulty of distinguishing them with X-ray diffraction. We also provide structural refinements of neutron diffraction data from single crystals of CeAlSi in Figs. D.1C,D. The two refinements are nearly indistinguishable, but the goodness-of-fit parameter (χ^2) is slightly better in the noncentrosymmetric case (#109). Because the diffraction data are not conclusive, we used SHG measurements discussed in the main text to identify the correct space group. SHG signal is especially sensitive to the absence of a center of inversion in the unit cell, being negligible in a centrosymmetric space group. The large SHG signal shown in the main text identifies the noncentrosymmetric space group $I4_1md$ (#109) unambiguously.

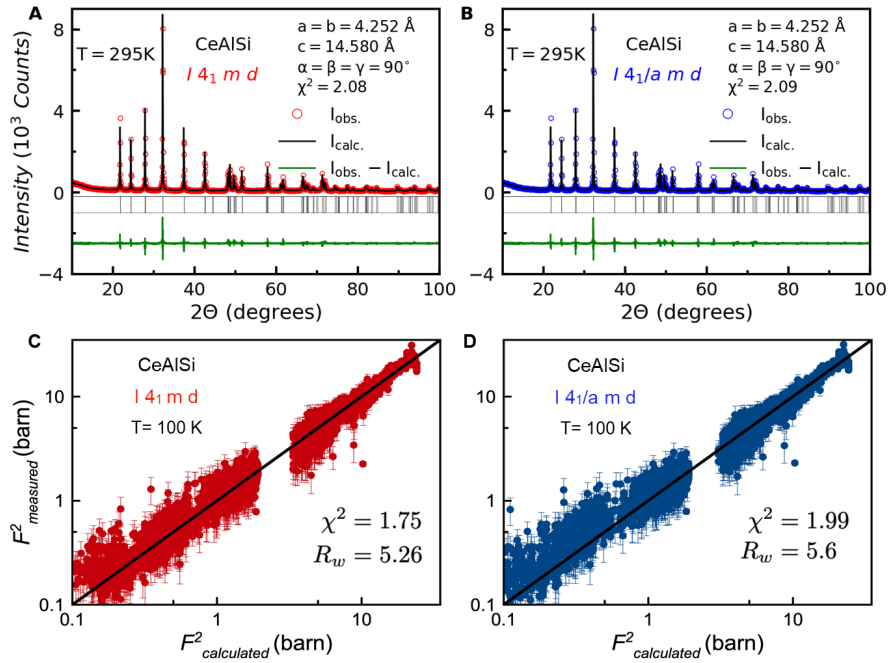


Figure D.1: Rietveld refinement analysis of Powder XRD and neutron data for CeAlSi. (A) X-ray refinement in the noncentrosymmetric space group $I4_1md$ (#109). (B) X-ray refinement in the centrosymmetric space group $I4_1/amd$ (#141), which is nearly indistinguishable from A. (C) Neutron refinement in the centrosymmetric space group $I4_1md$ (#109). (D) Neutron refinement in the noncentrosymmetric space group $I4_1/amd$ (#141) with a slightly worse χ^2 than in C.

Table D.1: Rietveld refinement parameters for CeAlSi. R -factors and χ^2 are listed for the refinements in Figs. D.1A and B.

Space Group	$I 4_1 m d$	$I 4_1/a m d$
R_{Bragg}	5.13	5.20
R_f	4.38	4.47
R_{exp}	7.06	7.06
R_p	7.86	7.88
R_{wp}	10.2	10.2
χ^2	2.08	2.09

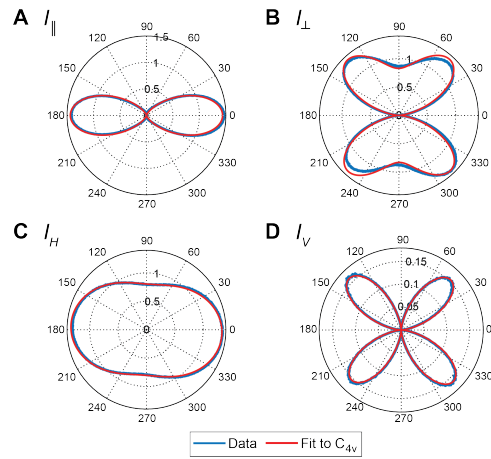


Figure D.2: Second harmonic generation of CeAlSi. The SHG data for incoming wavelength of 1500 nm and outgoing wavelength of 750 nm, and fits to the bulk electric dipolar SHG in the C_{4v} point group as given by Eqs. [D.1-D.4] for (A) I_{\parallel} , (B) I_{\perp} , (C) I_V , and (D) I_H .

D.2 Second Harmonic Generation

The SHG data were fit to functions appropriate to the four different experimental configurations as follows: incoming polarization rotating, output polarizer fixed with polarization parallel to the crystalline [010] axis, denoted $I_H(\phi)$; incoming polarization rotating, output polarizer fixed with polarization parallel to the $[10\bar{1}]$ axis, denoted $I_V(\phi)$; incoming polarization rotating, outgoing polarizer rotated at 0° angle relative to the incoming polarization, denoted $I_{\parallel}(\phi)$; and incoming polarization rotating, outgoing polarizer rotated with polarization axis at 90° angle relative to the incoming polarization, denoted $I_{\perp}(\phi)$. In the electric dipole approximation, the mathematical forms of the various responses for the [101] crystal face in the $I4_1md$ space group (C_{4v} point group) are given by

$$I_{\parallel}^{eee}(\phi) = \frac{1}{32} \cos^2(\phi) [(-2\chi_{xxz}^{eee} - \chi_{zxx}^{eee} + \chi_{zzz}^{eee}) \cos(2\phi) + 6\chi_{xxz}^{eee} + 3\chi_{zxx}^{eee} + \chi_{zzz}^{eee}]^2 \quad (\text{D.1})$$

$$I_{\perp}^{eee}(\phi) = \frac{1}{8} \sin^2(\phi) [(-2\chi_{xxz}^{eee} + \chi_{zxx}^{eee} + \chi_{zzz}^{eee}) \cos^2(\phi) + 2\chi_{zxx}^{eee} \sin^2(\phi)]^2 \quad (\text{D.2})$$

$$I_H^{eee}(\phi) = \frac{1}{8} [(2\chi_{xxz}^{eee} + \chi_{zxx}^{eee} + \chi_{zzz}^{eee}) \cos^2(\phi) + 2\chi_{zxx}^{eee} \sin^2(\phi)]^2 \quad (\text{D.3})$$

$$I_V^{eee}(\phi) = 2 [\chi_{xxz}^{eee} \sin(\phi) \cos(\phi)]^2 \quad (\text{D.4})$$

The data were fit to expressions [D.1-D.4] accounting for a rotation of the sample axes relative to the laboratory x-axis to produce excellent fits to the data as seen in Fig. D.2. The competing space group assignment $I4_1/amd$ (point group D_{4h}) is centrosymmetric and thus would not be expected to produce as strong of a SHG response as we have shown here.

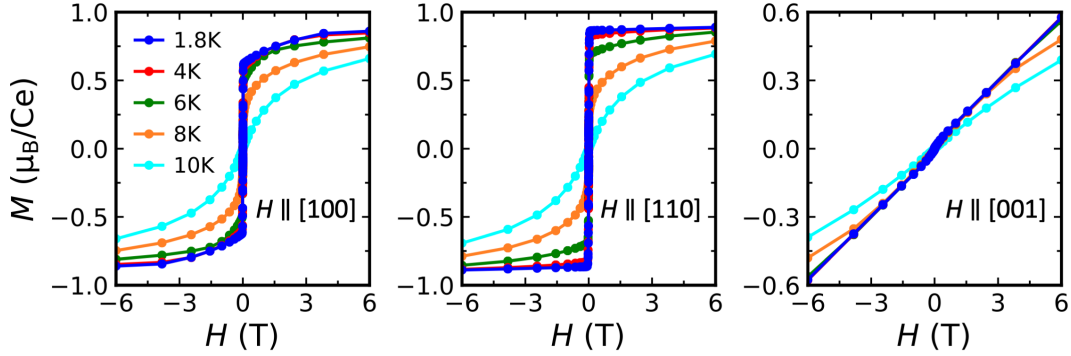


Figure D.3: Temperature dependence of M v.s. H curves in CeAlSi. The magnetization data measured at different temperatures for $\mathbf{H} \parallel [100]$ (left panel), $\mathbf{H} \parallel [110]$ (central panel), and $\mathbf{H} \parallel [001]$ (right panel). Note that the scale of y-axis in the right panel is different from the others. For each temperature in all panels, a full hysteresis loop is measured and plotted here but is not visible at the current scale.

D.3 Temperature Dependence of M v.s. H Curves

Figure D.3 shows the magnetization data for different field orientations. When the field is in-plane ($\mathbf{H} \parallel [100]$ and $[110]$), the magnetization quickly jumps up at small fields and saturated at high fields. Such saturated behavior is most pronounced at $T = 1.8$ K, and persists up to near $T_C \sim 8$ K. From the base temperature 1.8 K to T_C , the saturated moment at the same field (6 T) drops by 10%, which is typical of ferromagnetic materials [34].

D.4 Neutron Scattering

A symmetry analysis of the possible irreducible representations (irreps) appropriate for the $\vec{k} = (000)$ ordering in CeAlSi was done with SARAh software package [214]. The observed structure factors were determined by the areas of various measured rocking scans, which were corrected for resolution function effects using the Cooper-Nathan formalism [215]. This analysis revealed three possible irreps: Γ_2 and Γ_4 , which correspond to FM and AF structures, respectively, with

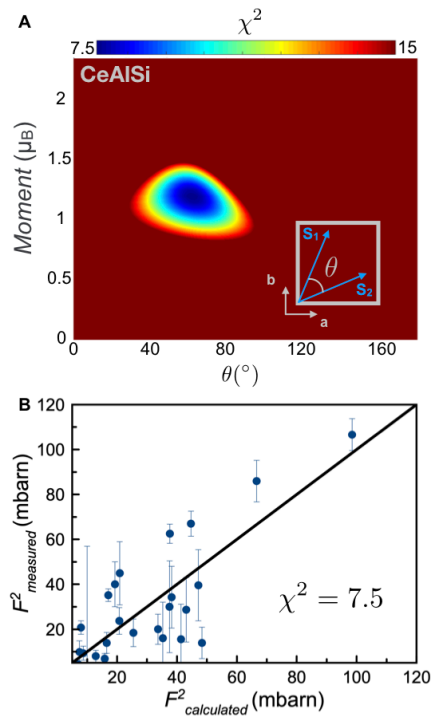


Figure D.4: Neutron diffraction data of CeAlSi. **(A)** A color map of χ^2 in the magnetic refinement of CeAlSi as a function of the Ce moment and the angle (θ between the Ce1 and Ce2 spins, see inset). **(B)** The calculated and observed magnetic structure factors of CeAlSi for $\theta = 68^\circ$ and a magnetic moment of $1.1 \mu_B$.

the spins oriented along the c -axis, and Γ_5 with the spins constrained to the ab -plane. We observe several (00L) peaks that can only occur for spins pointing in the ab -plane, allowing us to conclude that CeAlSi orders in the Γ_5 manifold. The results of our refinement are shown in Fig. D.4A where the χ^2 is plotted as a function of the moment of the Ce spins and the angle between the Ce1 spins at (000) and the Ce2 spins at (0,1/2,1/4). χ^2 shows a minimum at $\theta = 68^\circ$ with a moment of $1.1 \mu_B$. This refinement assumed that the moments of Ce1 and Ce2 spins are identical, although a different moment on the two sites is not strictly forbidden by symmetry. This ambiguity introduces a large uncertainty in the possible angle between the two Ce spins. The final refinement is presented in Fig. D.4B where the calculated and observed structure factors are plotted.

D.5 Scanning SQUID Imaging

Although we have already shown our DC flux images in the main text, these are reproduced here (Figs. D.5A,B), along with the AC susceptibility images (Figs. D.5C,D) to provide more information about the FM domains. The susceptibility data were measured by scanning a SQUID sensor over the ab -plane of a polished crystal while applying a small current in the induction coil (Fig. D.5E). The blue regions in Figs. D.5C,D are stable in-plane FM domains with negligible out-of-plane susceptibility. The green regions, however, are metastable domains with larger out-of-plane spin fluctuations, particularly noticeable at zero field. Whether these metastable domains are an inherent feature of FM-WSM remains an open question. The overall configuration of domains is not reproducible with temperature cycling; therefore, the domains do not originate from compositional variations across the sample. Local susceptibility from the SQUID sensor shows a sharp phase transition (Fig. D.5F) at the same temperature as other bulk experiments discussed in the main text.

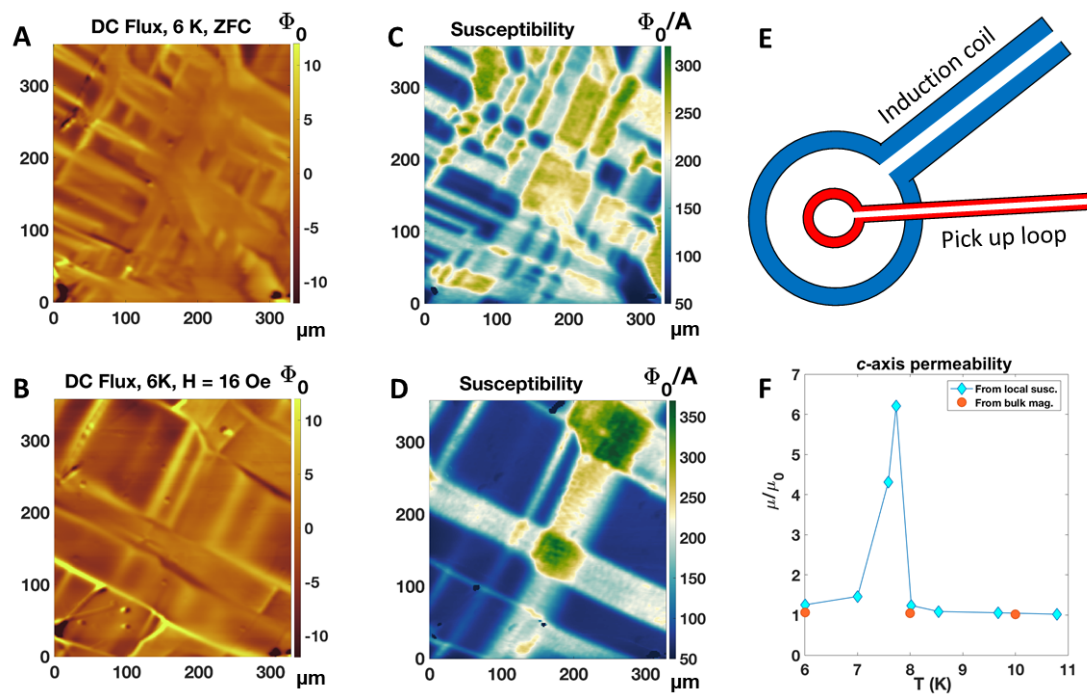


Figure D.5: Scanning SQUID Imaging of FM domains in CeAlSi. (A) DC flux at 6 K under zero field. (B) DC flux at 6 K under 16 G in-plane field. (C) AC susceptibility at 6 K under zero field. (D) AC susceptibility at 6 K under 16 G in-plane field. (E) Schematic diagram of the SQUID sensor and the field coil. (F) Comparison between the susceptibility from the scanning SQUID microscope and bulk measurements.

Table D.2: Momentum space locations and energies of the Weyl nodes in CeAlSi with [110] ferromagnetic order. Eight W_1 (four sets $W_1^{1,2,3,4}$) and sixteen W_2 (four sets $W_2^{1,2,3,4}$) nodes are listed. The Weyl nodes in the same set are related by symmetries: $m_{[110]}$, $m_{[1\bar{1}0]} \times T$, and $C_{2z} \times T$, where m 's denote the mirror planes, C_{2z} is the rotational axis, and T is the time-reversal operation.

Weyl nodes	(k_x, k_y, k_z) ($1/\text{\AA}$) [chirality]	E (meV)
W_1^1	$(-0.006, 0.765, 0.000)$ [+], $(-0.765, 0.006, 0.000)$ [-]	118
W_1^2	$(0.759, 0.008, 0.000)$ [+], $(-0.008, -0.759, 0.000)$ [-]	103
W_1^3	$(0.008, -0.773, 0.000)$ [+], $(0.773, -0.008, 0.000)$ [-]	86
W_1^4	$(-0.774, -0.009, 0.000)$ [+], $(0.009, 0.774, 0.000)$ [-]	81
W_2^1	$(0.361, -0.024, \pm 0.273)$ [+], $(0.024, -0.361, \pm 0.273)$ [-]	16
W_2^2	$(0.034, 0.362, \pm 0.263)$ [+], $(-0.362, -0.034, \pm 0.263)$ [-]	24
W_2^3	$(-0.385, 0.027, \pm 0.259)$ [+], $(-0.027, 0.385, \pm 0.259)$ [-]	-10
W_2^4	$(-0.025, -0.376, \pm 0.261)$ [+], $(0.376, 0.025, \pm 0.261)$ [-]	-9

D.6 Weyl Points

In this section, we describe the energies, locations, and dispersions of the Weyl nodes in CeAlSi. There is a total of 24 Weyl nodes in the BZ including eight W_1 and sixteen W_2 nodes as summarized in Table D.2. The terminology of W_1 and W_2 here refers to the location of the nodes. The W_1 nodes are located on the $k_z = 0$ plane and come in four pairs. The W_2 nodes are located at $k_z \neq 0$ points and come in eight pairs. Without considering magnetism, these Weyl nodes are symmetry-related and lie across the $k_x = 0$ and $k_y = 0$ mirror planes. Magnetic ordering reduces the momentum-space symmetries, and leads to the final locations and energies given in Table D.2. W_1 nodes are located $\sim 80 - 120$ meV above the E_F , whereas W_2 nodes lie close to the E_F and dominate the low-energy physics of CeAlSi.

We show the energy dispersion in the vicinity of three representative Weyl nodes in Fig. D.6. A linear dispersion is seen along the three momentum directions near both W_1 and W_2 nodes, indicating that these Weyl fermions in CeAlSi are type I.

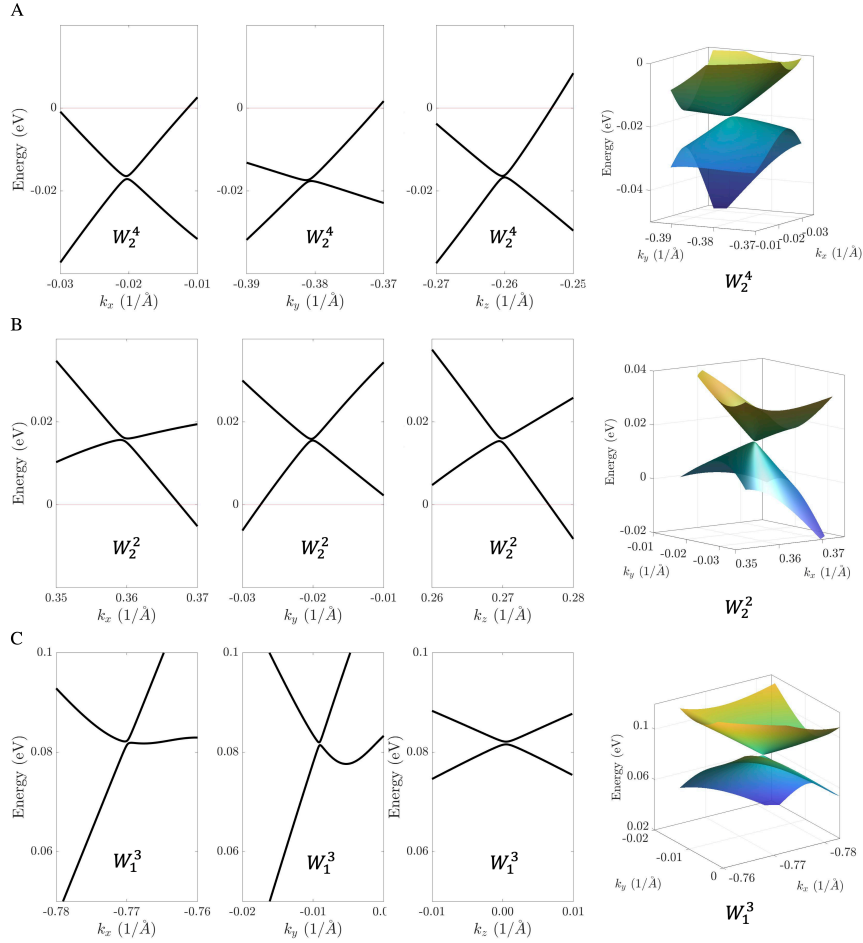


Figure D.6: Energy dispersion of the Weyl quasiparticles in CeAlSi. (A) Calculated band structure in the vicinity of W_2^4 along the k_x (left), k_y (middle), and k_z (right) momentum directions. (B) and (C) are same as (A) except that they refer to the energy dispersion close to W_2^2 and W_1^3 , respectively. All Weyl nodes are type-I. This is better seen in the three-dimensional rendition of the band structure near the nodal points in the rightmost column of figures.

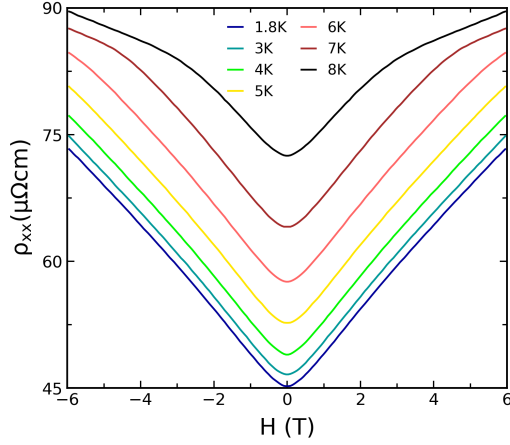


Figure D.7: ρ_{xx} Data. ρ_{xx} of CeAlSi measured at different temperatures.

D.7 ρ_{xx} Data

In order to calculate the loop Hall conductivity $\sigma_{yx}^L = \rho_{yx}^L / \rho_{xx}^2$, we used ρ_{yx}^L in Fig. 4.10(d) of the main text and ρ_{xx} shown here in Fig. D.7. ρ_{xx} was measured as a function of field at different temperatures.

D.8 EDX Analysis

Here we discuss the Ce:Al:Si ratios based on an EDX analysis of a few representative samples. As shown in Table D.3, different crystals in the same batch as well as the crystals taken from different batches can show slight off-stoichiometry. Due to the small size of the Fermi pockets in CeAlSi, Al/Si off-stoichiometry affects the carrier density and E_F , but it has little effect on the carrier mobility and RRR . Note that semimetals have small Fermi surfaces, so that they can have relatively large $\omega_c\tau$ values and exhibit quantum oscillations even in the presence

Table D.3: EDX results for CeAlSi crystals grown by several different methods. The reported atomic ratios were derived by normalizing the Ce content to 1. Sample labels 1 and 2 refer to different crystals in the same batch, NC means that a normal alumina crucible was used, and CC means that a Canfield crucible (a set of crucibles with an alumina strainer) was used. Both NC and CC growths followed the heating cycle described in the main text. NC-slow used a Canfield crucible but with a slower cooling rate (0.05 °C/min). The error in all the reported values is 1%.

Sample label	Ce	Al	Si
NC-1	1	0.96	1.00
NC-2	1	0.98	0.96
CC-1	1	0.99	1.00
CC-2	1	1.01	1.01
NC-slow-1	1	1.05	1.02
NC-slow-2	1	0.96	0.99

of small levels of disorder.

D.9 Quantum Oscillation

SdH oscillations were measured in the resistivity data with the magnetic field oriented 30 degrees away from the c -axis towards the a -axis (Fig. D.8A-C). Quantum oscillation (QO) frequencies were derived from the experimental data by two different methods. (1) By determining the separation between the neighboring peaks of the raw data in Fig. 4G of the main text and Fig. D.8D-F (denoted Exp-DIR), and (2) from the positions of the peaks in the FFT spectra in Fig. D.8G-I (denoted Exp-FFT). Only one frequency (α , the electron pocket in Fig. 4G) is derived from Exp-DIR dataset, whereas the second method yields not only the α but also another frequency β (another electron pocket, not shown in Fig. 4G), see Table D.4. We note that the β frequency is less robust in our data since it can not be identified by Exp-DIR and does not appear clearly in all samples in the FFT spectra. However, our assignment of E_F 's can be done by only using α , and we include β frequency for a complete presentation of our data even though it is

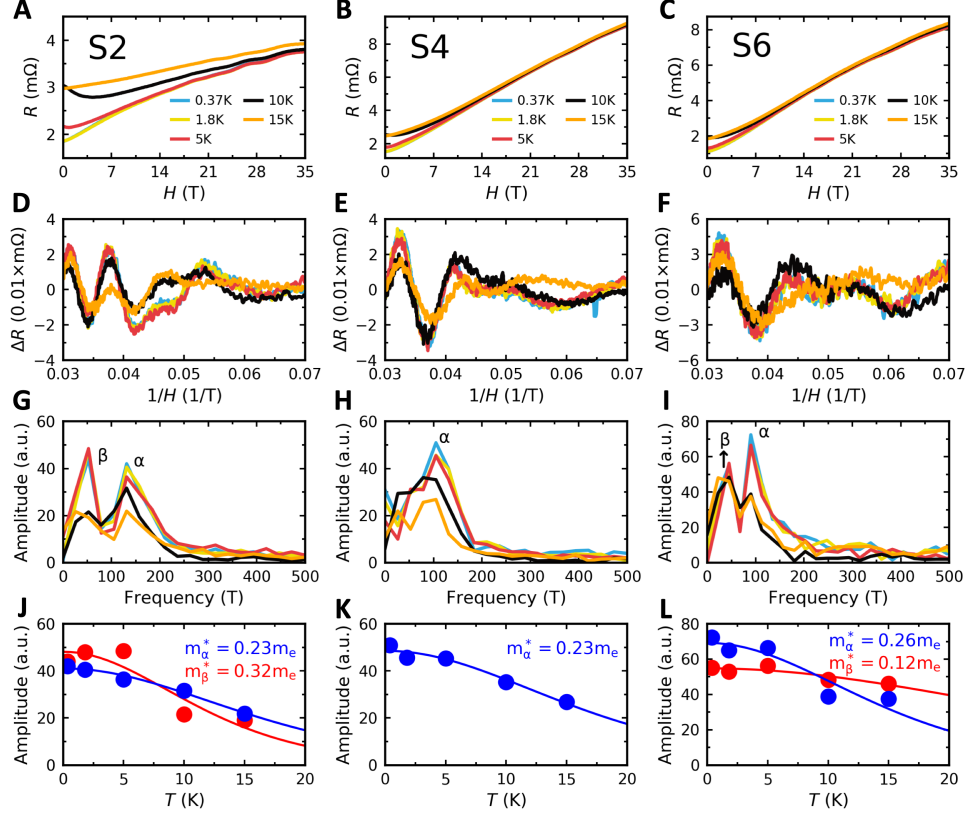


Figure D.8: Quantum oscillation data of CeAlSi. (A)-(C) Resistivity data at various temperatures for samples S2, S4 and S6 up to 35 T. (D)-(F) Shubnikov-de Haas oscillations extracted from (A)-(C) by subtracting a smooth background from the data. (G)-(I) Fast Fourier Transform (FFT) spectra corresponding to the data in (D)-(F). α and β frequencies for each sample are listed in Table D.4. (J)-(L) The fitting of FFT amplitudes (dots) to Lifshitz-Kosevich formula[112, 113] (lines) for the samples S2, S4 and S6. The FFT amplitudes of α and β frequencies are shown as blue and red dots. Effective masses are given in the upper right corners.

Table D.4: Determination of E_F from quantum oscillations for CeAlSi. SdH frequencies obtained directly from the experimental data (Exp-DIR, Fig. 4.10G of the main text and Figs. D.8D-F) and from the Fourier transform of the data (Exp-FFT, Figs. D.8G-I) are compared with the values based on the computed band structures (Theory). By matching the frequencies between theory and experiment and tracking the systematic evolution of the α and β frequencies, we determine the E_F value in samples S2, S4 and S6 to lie 32, 23, and 12 meV above the DFT-calculated E_F values, respectively. Similar methods have been applied to other semimetals [53, 99, 123].

Method	Frequency α (T)			Frequency β (T)		
	S2	S4	S6	S2	S4	S6
Exp-DIR	143	115	85	N/A	N/A	N/A
Exp-FFT	131	105	90	52	N/A	34
Theory	144	118	87	58	41	24

not necessary for our main argument. From either the Exp-DIR or the Exp-FFT dataset based analysis scheme, it is clear that α evolves monotonically in going from the sample S2 to S4 to S6. To determine the E_F for samples S2, S4 and S6, we varied the E_F in our calculated band structure and obtained the extremal areas of the corresponding Fermi surfaces via the SKEAF code [100]. Through the Onsager relation, these areas were then converted to QO frequencies and fitted to the corresponding experimental values to obtain the correct E_F values for the various samples. Table D.4 shows the agreement between Exp-DIR, Exp-FFT and Theory results after the correct E_F value is determined for samples S2 (32 meV above the DFT-calculated value E_F^{DFT}), S4 (23 meV above E_F^{DFT}), and S6 (12 meV above E_F^{DFT}). Experimental [112, 113] and theoretical [100] effective masses listed in Table D.5 also show reasonable agreement. The agreement between the SdH frequencies derived directly from the data, the FFT spectra, and the DFT calculations strongly supports our assignment of E_F for these three samples.

Table D.5: Effective masses of CeAlSi. Experimental and theoretical effective masses for the α and β pockets for various samples as discussed in the text.

Method	Effective Mass of α (m_e)			Effective Mass of β (m_e)		
	S2	S4	S6	S2	S4	S6
Exp-FFT	0.22	0.23	0.26	0.32	N/A	0.12
Theory	0.25	0.25	0.23	0.10	0.09	0.08

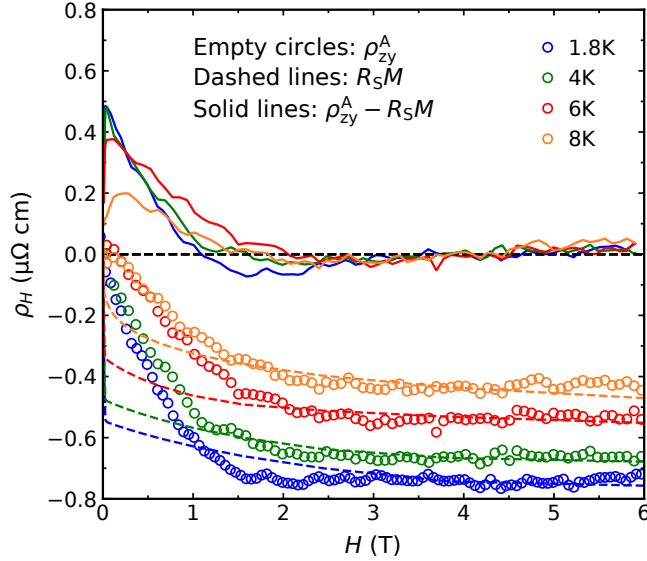


Figure D.9: ρ_{zy}^A and R_{SM} data of CeAlSi. ρ_{zy}^A , R_{SM} , and $\rho_{zy}^{other} = \rho_{zy}^A - R_{SM}$ are plotted as empty circles, dashed lines, and solid lines at four representative temperatures. The color code of temperature used for empty circles applies to dashed lines and solid lines as well.

D.10 The Difference between ρ_{zy}^A and $R_S M$

Ideally, for a material with a collinear FM order, its anomalous Hall signal is usually expected to scale with the magnetization as the field increases. However, in CeAlSi, we find a noncollinear FM order which likely leads to a misalignment between the anomalous Hall signal ρ_{zy}^A and M measured with $H \parallel [100]$ [205, 206]. Here, we extract the difference between them as a reference. We assumed a simple model $\rho_{zy} = R_0 H + \rho_{zy}^A$ (see Fig. 4A and 4B in the main text) and $\rho_{zy}^A = R_S M + \rho_{zy}^{other}$ to get a general picture of the difference between ρ_{zy}^A and $R_S M$, while more complicated models are also available [216]. As shown in Fig. D.9, ρ_{zy}^A does not scale with M at all fields; although they both saturate and align well at $H > 2$ T, there is another Hall signal ρ_{zy}^{other} appearing at $H < 2$ T. Since CeAlSi hosts a noncollinear magnetism, it may be tentative to think of ρ_{zy}^{other} as a topological Hall effect [185, 186]. A topological Hall effect usually requires a finite scalar spin chirality caused by noncoplanar spins at intermediate fields, and the effect disappears as the spins align with the magnetic field at high fields. In CeAlSi, the noncollinear spins are in-plane, and the canting angle between them does not change up to $H = 8$ T when the field is along the easy axis based on our neutron experiment. These two observations do not support ρ_{zy}^{other} appearing at $H < 2$ T as a topological Hall effect. Another possibility might be that the entire ρ_{zy} is dominated by a multiband effect, but this is not very likely considering that the scaling behavior of σ_{yz}^A v.s. σ_{yy}^2 reveals an intrinsic anomalous Hall conductivity that agrees with the theoretical calculation (see Sec. III in the main text). As a result, we think the difference between ρ_{zy}^A and $R_S M$ may be due to the fact that CeAlSi hosts a noncollinear FM order which does not easily saturates, similar to the $\text{Pr}_2\text{Ir}_2\text{O}_7$ case when the field is along [100] and [110].

As a reference, the R_S coefficients for $T = 1.8, 4, 6,$ and 8 K are (in units of cm^3/C): 0.047, 0.045, 0.036, 0.033.

BIBLIOGRAPHY

- [1] K. v. Klitzing, G. Dorda, and M. Pepper, *Phys. Rev. Lett.* **45**, 494 (1980).
- [2] D. J. Thouless, M. Kohmoto, M. P. Nightingale, and M. den Nijs, *Phys. Rev. Lett.* **49**, 405 (1982).
- [3] L. Fu, C. L. Kane, and E. J. Mele, *Phys. Rev. Lett.* **98**, 106803 (2007).
- [4] L. Fu and C. L. Kane, *Phys. Rev. B* **76**, 045302 (2007).
- [5] H. Zhang, C.-X. Liu, X.-L. Qi, X. Dai, Z. Fang, and S.-C. Zhang, *Nat. Phys.* **5**, 438 (2009).
- [6] Y. L. Chen, J. G. Analytis, J.-H. Chu, Z. K. Liu, S.-K. Mo, X. L. Qi, H. J. Zhang, D. H. Lu, X. Dai, Z. Fang, S. C. Zhang, I. R. Fisher, Z. Hussain, and Z.-X. Shen, *Science* **325**, 178 (2009).
- [7] D. Hsieh, Y. Xia, L. Wray, D. Qian, A. Pal, J. H. Dil, J. Osterwalder, F. Meier, G. Bihlmayer, C. L. Kane, Y. S. Hor, R. J. Cava, and M. Z. Hasan, *Science* **323**, 919 (2009).
- [8] B. A. Bernevig, T. L. Hughes, and S.-C. Zhang, *Science* **314**, 1757 (2006).
- [9] M. König, S. Wiedmann, C. Brüne, A. Roth, H. Buhmann, L. W. Molenkamp, X.-L. Qi, and S.-C. Zhang, *Science* **318**, 766 (2007).
- [10] S. M. Young, S. Zaheer, J. C. Y. Teo, C. L. Kane, E. J. Mele, and A. M. Rappe, *Phys. Rev. Lett.* **108**, 140405 (2012).
- [11] Z. Wang, Y. Sun, X.-Q. Chen, C. Franchini, G. Xu, H. Weng, X. Dai, and Z. Fang, *Phys. Rev. B* **85**, 195320 (2012).
- [12] Z. Wang, H. Weng, Q. Wu, X. Dai, and Z. Fang, *Phys. Rev. B* **88**, 125427 (2013).
- [13] S. Borisenko, Q. Gibson, D. Evtushinsky, V. Zabolotnyy, B. Büchner, and R. J. Cava, *Phys. Rev. Lett.* **113**, 027603 (2014).
- [14] Z. K. Liu, B. Zhou, Y. Zhang, Z. J. Wang, H. M. Weng, D. Prabhakaran, S.-K. Mo, Z. X. Shen, Z. Fang, X. Dai, Z. Hussain, and Y. L. Chen, *Science* **343**, 864 (2014).
- [15] X. Wan, A. M. Turner, A. Vishwanath, and S. Y. Savrasov, *Phys. Rev. B* **83**, 205101 (2011).
- [16] S.-M. Huang, S.-Y. Xu, I. Belopolski, C.-C. Lee, G. Chang, B. Wang, N. Alidoust, G. Bian, M. Neupane, C. Zhang, S. Jia, A. Bansil, H. Lin, and M. Z. Hasan, *Nat. Commun.* **6**, 7373 (2015).

- [17] S.-Y. Xu, I. Belopolski, N. Alidoust, M. Neupane, G. Bian, C. Zhang, R. Sankar, G. Chang, Z. Yuan, C.-C. Lee, S.-M. Huang, H. Zheng, J. Ma, D. S. Sanchez, B. Wang, A. Bansil, F. Chou, P. P. Shibayev, H. Lin, S. Jia, and M. Z. Hasan, *Science* **349**, 613 (2015).
- [18] D.-X. Qu, Y. S. Hor, J. Xiong, R. J. Cava, and N. P. Ong, *Science* **329**, 821 (2010).
- [19] J. G. Analytis, R. D. McDonald, S. C. Riggs, J.-H. Chu, G. S. Boebinger, and I. R. Fisher, *Nat. Phys.* **6**, 960 (2010).
- [20] R. Yu, W. Zhang, H.-J. Zhang, S.-C. Zhang, X. Dai, and Z. Fang, *Science* **329**, 61 (2010).
- [21] C.-Z. Chang, J. Zhang, X. Feng, J. Shen, Z. Zhang, M. Guo, K. Li, Y. Ou, P. Wei, L.-L. Wang, Z.-Q. Ji, Y. Feng, S. Ji, X. Chen, J. Jia, X. Dai, Z. Fang, S.-C. Zhang, K. He, Y. Wang, L. Lu, X.-C. Ma, and Q.-K. Xue, *Science* **340**, 167 (2013).
- [22] X. Kou, S.-T. Guo, Y. Fan, L. Pan, M. Lang, Y. Jiang, Q. Shao, T. Nie, K. Murata, J. Tang, Y. Wang, L. He, T.-K. Lee, W.-L. Lee, and K. L. Wang, *Phys. Rev. Lett.* **113**, 137201 (2014).
- [23] C.-Z. Chang, W. Zhao, D. Y. Kim, P. Wei, J. K. Jain, C. Liu, M. H. W. Chan, and J. S. Moodera, *Phys. Rev. Lett.* **115**, 057206 (2015).
- [24] N. P. Armitage, E. J. Mele, and A. Vishwanath, *Rev. Mod. Phys.* **90**, 015001 (2018).
- [25] T. Liang, Q. Gibson, M. N. Ali, M. Liu, R. J. Cava, and N. P. Ong, *Nat. Mater.* **14**, 280 (2015).
- [26] F. F. Tafti, Q. Gibson, S. Kushwaha, J. W. Krizan, N. Haldolaarachchige, and R. J. Cava, en, *Proc. Natl. Acad. Sci.* **113**, E3475 (2016).
- [27] F. F. Tafti, Q. D. Gibson, S. K. Kushwaha, N. Haldolaarachchige, and R. J. Cava, en, *Nat. Phys.* **12**, 272 (2016).
- [28] D. T. Son and B. Z. Spivak, *Phys. Rev. B* **88**, 104412 (2013).
- [29] X. Huang, L. Zhao, Y. Long, P. Wang, D. Chen, Z. Yang, H. Liang, M. Xue, H. Weng, Z. Fang, X. Dai, and G. Chen, *Phys. Rev. X* **5**, 031023 (2015).
- [30] M. Hirschberger, S. Kushwaha, Z. Wang, Q. Gibson, S. Liang, C. A. Belvin, B. A. Bernevig, R. J. Cava, and N. P. Ong, *Nat. Mater.* **15**, 1161 (2016).
- [31] S. Liang, J. Lin, S. Kushwaha, J. Xing, N. Ni, R. J. Cava, and N. P. Ong, *Phys. Rev. X* **8**, 031002 (2018).
- [32] K.-Y. Yang, Y.-M. Lu, and Y. Ran, *Phys. Rev. B* **84**, 075129 (2011).
- [33] A. A. Burkov, *Phys. Rev. Lett.* **113**, 187202 (2014).
- [34] E. Liu, Y. Sun, N. Kumar, L. Muechler, A. Sun, L. Jiao, S.-Y. Yang, D. Liu, A. Liang, Q. Xu, J. Kroder, V. Süß, H. Borrmann, C. Shekhar, Z. Wang, C. Xi, W. Wang, W. Schnelle, S. Wirth, Y. Chen, S. T. B. Goennenwein, and C. Felser, *Nat. Phys.* **14**, 1125 (2018).

- [35] Y. Tokura, M. Kawasaki, and N. Nagaosa, *Nat. Phys.* **13**, 1056 (2017).
- [36] X. Wang, Y. Du, S. Dou, and C. Zhang, *Phys. Rev. Lett.* **108**, 266806 (2012).
- [37] J. Tang, L.-T. Chang, X. Kou, K. Murata, E. S. Choi, M. Lang, Y. Fan, Y. Jiang, M. Montazeri, W. Jiang, Y. Wang, L. He, and K. L. Wang, *Nano Lett.* **14**, 5423 (2014).
- [38] M. Zeng, C. Fang, G. Chang, Y.-A. Chen, T. Hsieh, A. Bansil, H. Lin, and L. Fu, *arXiv preprint arXiv:1504.03492* (2015).
- [39] S. Sun, Q. Wang, P.-J. Guo, K. Liu, and H. Lei, *New J. Phys.* **18**, 082002 (2016).
- [40] N. Kumar, C. Shekhar, S.-C. Wu, I. Leermakers, O. Young, U. Zeitler, B. Yan, and C. Felser, *Phys. Rev. B* **93**, 241106 (2016).
- [41] K. Wang, D. Graf, L. Li, L. Wang, and C. Petrovic, en, *Sci. Rep.* **4**, 7328 (2014).
- [42] Y. Li, L. Li, J. Wang, T. Wang, X. Xu, C. Xi, C. Cao, and J. Dai, *Phys. Rev. B* **94**, 121115 (2016).
- [43] Y. Wu, Y. Lee, T. Kong, D. Mou, R. Jiang, L. Huang, S. L. Bud'ko, P. C. Canfield, and A. Kaminski, *Phys. Rev. B* **96**, 035134 (2017).
- [44] N. J. Ghimire, Y. Luo, M. Neupane, D. J. Williams, E. D. Bauer, and F. Ronning, en, *J. Phys.: Condens. Matter* **27**, 152201 (2015).
- [45] Y.-Y. Wang, Q.-H. Yu, P.-J. Guo, K. Liu, and T.-L. Xia, *Phys. Rev. B* **94**, 041103 (2016).
- [46] M. N. Ali, J. Xiong, S. Flynn, J. Tao, Q. D. Gibson, L. M. Schoop, T. Liang, N. Haldolaarachchige, M. Hirschberger, N. P. Ong, and R. J. Cava, en, *Nature* **514**, 205 (2014).
- [47] X. H. Niu, D. F. Xu, Y. H. Bai, Q. Song, X. P. Shen, B. P. Xie, Z. Sun, Y. B. Huang, D. C. Peets, and D. L. Feng, *Phys. Rev. B* **94**, 165163 (2016).
- [48] Y. Wu, T. Kong, L.-L. Wang, D. D. Johnson, D. Mou, L. Huang, B. Schunk, S. L. Bud'ko, P. C. Canfield, and A. Kaminski, *Phys. Rev. B* **94**, 081108 (2016).
- [49] J. Nayak, S.-C. Wu, N. Kumar, C. Shekhar, S. Singh, J. Fink, E. E. D. Rienks, G. H. Fecher, S. S. P. Parkin, B. Yan, and C. Felser, *Nat. Commun.* **8**, 13942 (2017).
- [50] R. Lou, B.-B. Fu, Q. N. Xu, P.-J. Guo, L.-Y. Kong, L.-K. Zeng, J.-Z. Ma, P. Richard, C. Fang, Y.-B. Huang, S.-S. Sun, Q. Wang, L. Wang, Y.-G. Shi, H. C. Lei, K. Liu, H. M. Weng, T. Qian, H. Ding, and S.-C. Wang, *Phys. Rev. B* **95**, 115140 (2017).

- [51] L.-K. Zeng, R. Lou, D.-S. Wu, Q. N. Xu, P.-J. Guo, L.-Y. Kong, Y.-G. Zhong, J.-Z. Ma, B.-B. Fu, P. Richard, P. Wang, G. T. Liu, L. Lu, Y.-B. Huang, C. Fang, S.-S. Sun, Q. Wang, L. Wang, Y.-G. Shi, H. M. Weng, H.-C. Lei, K. Liu, S.-C. Wang, T. Qian, J.-L. Luo, and H. Ding, *Phys. Rev. Lett.* **117**, 127204 (2016).
- [52] H. Oinuma, S. Souma, D. Takane, T. Nakamura, K. Nakayama, T. Mitsuhashi, K. Horiba, H. Kumigashira, M. Yoshida, A. Ochiai, T. Takahashi, and T. Sato, *Phys. Rev. B* **96**, 041120 (2017).
- [53] H.-Y. Yang, T. Nummy, H. Li, S. Jaszewski, M. Abramchuk, D. S. Dessau, and F. Tafti, *Phys. Rev. B* **96**, 235128 (2017).
- [54] T. Wiener and P. Canfield, *Journal of Alloys and Compounds* **303**, 505 (2000).
- [55] L. Ye, T. Suzuki, C. R. Wicker, and J. G. Checkelsky, *Phys. Rev. B* **97**, 081108 (2018).
- [56] N. Wakeham, E. D. Bauer, M. Neupane, and F. Ronning, *Phys. Rev. B* **93**, 205152 (2016).
- [57] Y. Zhou, X. Zhu, S. Huang, X. Chen, Y. Zhou, C. An, B. Zhang, Y. Yuan, Z. Xia, C. Gu, and Z. Yang, *Phys. Rev. B* **96**, 205122 (2017).
- [58] Y. Wang, J. H. Yu, Y. Q. Wang, C. Y. Xi, L. S. Ling, S. L. Zhang, J. R. Wang, Y. M. Xiong, T. Han, H. Han, J. Yang, J. Gong, L. Luo, W. Tong, L. Zhang, Z. Qu, Y. Y. Han, W. K. Zhu, L. Pi, X. G. Wan, C. Zhang, and Y. Zhang, *Phys. Rev. B* **97**, 115133 (2018).
- [59] E. H. Hall, *The London, Edinburgh, and Dublin Philosophical Magazine and Journal of Science* **10**, 301 (1880).
- [60] E. M. Pugh and N. Rostoker, *Rev. Mod. Phys.* **25**, 151 (1953).
- [61] N. Nagaosa, J. Sinova, S. Onoda, A. H. MacDonald, and N. P. Ong, *Rev. Mod. Phys.* **82**, 1539 (2010).
- [62] R. Karplus and J. M. Luttinger, *Phys. Rev.* **95**, 1154 (1954).
- [63] J. Smit, *Physica* **24**, 39 (1958).
- [64] L. Berger, *Phys. Rev. B* **2**, 4559 (1970).
- [65] G. Sundaram and Q. Niu, *Phys. Rev. B* **59**, 14915 (1999).
- [66] T. Jungwirth, Q. Niu, and A. H. MacDonald, *Phys. Rev. Lett.* **88**, 207208 (2002).
- [67] M. Onoda and N. Nagaosa, *J. Phys. Soc. Jpn.* **71**, 19 (2002).
- [68] Y. Yao, L. Kleinman, A. H. MacDonald, J. Sinova, T. Jungwirth, D.-s. Wang, E. Wang, and Q. Niu, *Phys. Rev. Lett.* **92**, 037204 (2004).
- [69] K. Kim, J. Seo, E. Lee, K.-T. Ko, B. S. Kim, B. G. Jang, J. M. Ok, J. Lee, Y. J. Jo, W. Kang, J. H. Shim, C. Kim, H. W. Yeom, B. I. Min, B.-J. Yang, and J. S. Kim, *Nat. Mater.* **17**, 794 (2018).

- [70] L. Ye, M. Kang, J. Liu, F. Von Cube, C. R. Wicker, T. Suzuki, C. Jozwiak, A. Bostwick, E. Rotenberg, D. C. Bell, L. Fu, R. Comin, and J. G. Checkelsky, *Nature* **555**, 638 (2018).
- [71] D. Xiao, M.-C. Chang, and Q. Niu, *Rev. Mod. Phys.* **82**, 1959 (2010).
- [72] G. Chang, B. Singh, S.-Y. Xu, G. Bian, S.-M. Huang, C.-H. Hsu, I. Belopolski, N. Alidoust, D. S. Sanchez, H. Zheng, H. Lu, X. Zhang, Y. Bian, T.-R. Chang, H.-T. Jeng, A. Bansil, H. Hsu, S. Jia, T. Neupert, H. Lin, and M. Z. Hasan, *Phys. Rev. B* **97**, 041104 (2018).
- [73] P. C. Canfield and Z. Fisk, *Philos. Mag. B: Physics of Condensed Matter; Statistical Mechanics, Electronic, Optical and Magnetic Properties* **65**, 1117 (1992).
- [74] M. G. Kanatzidis, R. Pöttgen, and W. Jeitschko, *Angewandte Chemie International Edition* **44**, 6996 (2005).
- [75] J. Rodriguez-Carvajal, *Physica B: Condensed Matter* **192**, 55 (1993).
- [76] H. Hodovanets, C. J. Eckberg, P. Y. Zavalij, H. Kim, W.-C. Lin, M. Zic, D. J. Campbell, J. S. Higgins, and J. Paglione, *Phys. Rev. B* **98**, 245132 (2018).
- [77] H. Y. Yang, B. Singh, B. Lu, C. Y. Huang, F. Bahrami, W. C. Chiu, D. Graf, S. M. Huang, B. Wang, H. Lin, D. Torchinsky, A. Bansil, and F. Tafti, *APL Mater.* **8**, 011111 (2020).
- [78] H.-Y. Yang, B. Singh, J. Gaudet, B. Lu, C.-Y. Huang, W.-C. Chiu, S.-M. Huang, B. Wang, F. Bahrami, B. Xu, J. Franklin, I. Sochnikov, D. E. Graf, G. Xu, Y. Zhao, C. M. Hoffman, H. Lin, D. H. Torchinsky, C. L. Broholm, A. Bansil, and F. Tafti, *Phys. Rev. B* **103**, 115143 (2021).
- [79] S. Blundell, *Magnetism in Condensed Matter* (Oxford University Press, 2003).
- [80] A. Kitaev, *Ann. Phys.* **321**, 2 (2006).
- [81] A. P. Ramirez, *Ann. Rev. Mater. Sci.* **24**, 453 (1994).
- [82] A. B. Pippard, *Magnetoresistance in Metals* (Cambridge university press, 1989).
- [83] J. M. Ziman, *Principles of the Theory of Solids* (Cambridge university press, 1972).
- [84] E. H. Hall, *American Journal of Mathematics* **2**, 287 (1879).
- [85] J. Xiong, S. K. Kushwaha, T. Liang, J. W. Krizan, M. Hirschberger, W. Wang, R. J. Cava, and N. P. Ong, *Science* **350**, 413 (2015).
- [86] C. L. Zhang, S. Y. Xu, I. Belopolski, Z. Yuan, Z. Lin, B. Tong, G. Bian, N. Alidoust, C. C. Lee, S. M. Huang, T. R. Chang, G. Chang, C. H. Hsu, H. T. Jeng, M. Neupane, D. S. Sanchez, H. Zheng, J. Wang, H. Lin, C. Zhang, H. Z. Lu, S. Q. Shen, T. Neupert, M. Z. Hasan, and S. Jia, *Nat. Commun.* **7**, 10735 (2016).

- [87] O. Pavlosiuk, D. Kaczorowski, and P. Wiśniewski, *Phys. Rev. B* **99**, 125142 (2019).
- [88] P. Hohenberg and W. Kohn, *Phys. Rev.* **136**, B864 (1964).
- [89] W. Kohn and L. J. Sham, *Phys. Rev.* **140**, A1133 (1965).
- [90] P. Blaha, K. Schwarz, G. K. H. Madsen, D. Kvasnicka, and J. Luitz, *WIEN2K an augmented Plane wave + Local Orbitals program for calculating crystal properties* (Karlheinz Schwarz, Techn. Universität Wien, Austria, Wien, Austria, 2001).
- [91] J. P. Perdew, K. Burke, and M. Ernzerhof, *Phys. Rev. Lett.* **77**, 3865 (1996).
- [92] F. Tran and P. Blaha, *Phys. Rev. Lett.* **102**, 226401 (2009).
- [93] D. Koller, F. Tran, and P. Blaha, *Phys. Rev. B* **83**, 195134 (2011).
- [94] V. I. Anisimov, J. Zaanen, and O. K. Andersen, *Phys. Rev. B* **44**, 943 (1991).
- [95] V. I. Anisimov, I. V. Solovyev, M. A. Korotin, M. T. Czyzyk, and G. A. Sawatzky, *Phys. Rev. B* **48**, 16929 (1993).
- [96] M. T. Czyzyk and G. A. Sawatzky, *Phys. Rev. B* **49**, 14211 (1994).
- [97] A. I. Liechtenstein, V. I. Anisimov, and J. Zaanen, *Phys. Rev. B* **52**, R5467 (1995).
- [98] P. Novák, F. Boucher, P. Gressier, P. Blaha, and K. Schwarz, *Phys. Rev. B* **63**, 235114 (2001).
- [99] H.-Y. Yang, J. Gaudet, A. A. Aczel, D. E. Graf, P. Blaha, B. D. Gaulin, and F. Tafti, *Phys. Rev. B* **98**, 045136 (2018).
- [100] P. M. Rourke and S. R. Julian, *Comput. Phys. Commun.* **183**, 324 (2012).
- [101] J. M. Ziman, *Electrons and phonons: the theory of transport phenomena in solids* (Oxford university press, 2001).
- [102] Y. Tian, L. Ye, and X. Jin, *Phys. Rev. Lett.* **103**, 087206 (2009).
- [103] A. Shitade and N. Nagaosa, *J. Phys. Soc. Jpn.* **81**, 083704 (2012).
- [104] D. Hou, G. Su, Y. Tian, X. Jin, S. A. Yang, and Q. Niu, *Phys. Rev. Lett.* **114**, 217203 (2015).
- [105] I. Belopolski, K. Manna, D. S. Sanchez, G. Chang, B. Ernst, J. Yin, S. S. Zhang, T. Cochran, N. Shumiya, H. Zheng, B. Singh, G. Bian, D. Multer, M. Litskevich, X. Zhou, S.-M. Huang, B. Wang, T.-R. Chang, S.-Y. Xu, A. Bansil, C. Felser, H. Lin, and M. Z. Hasan, *Science* **365**, 1278 (2019).
- [106] J. Weischenberg, F. Freimuth, J. Sinova, S. Blügel, and Y. Mokrousov, *Phys. Rev. Lett.* **107**, 106601 (2011).
- [107] S. Onoda, N. Sugimoto, and N. Nagaosa, *Phys. Rev. Lett.* **97**, 126602 (2006).

- [108] T. Miyasato, N. Abe, T. Fujii, A. Asamitsu, S. Onoda, Y. Onose, N. Nagaosa, and Y. Tokura, *Phys. Rev. Lett.* **99**, 086602 (2007).
- [109] L. Landau, *Z. Physik* **64**, 629 (1930).
- [110] L. Onsager, *The London, Edinburgh, and Dublin Philosophical Magazine and Journal of Science* **43**, 1006 (1952).
- [111] I. Lifshitz and A. Kosevich, *Sov. Phys. JETP* **2**, 636 (1956).
- [112] R. K. Willardson and A. C. Beer, *Semiconductors and semimetals*, Vol. 1 (Academic Press, 1967).
- [113] D. Shoenberg, *Magnetic Oscillations in Metals* (Cambridge University Press, Sept. 2009).
- [114] G. P. Mikitik and Y. V. Sharlai, *Phys. Rev. Lett.* **82**, 2147 (1999).
- [115] K. S. Novoselov, Z. Jiang, Y. Zhang, S. V. Morozov, H. L. Stormer, U. Zeitler, J. C. Maan, G. S. Boebinger, P. Kim, and A. K. Geim, *Science* **315**, 1379 (2007).
- [116] Z. Ren, A. A. Taskin, S. Sasaki, K. Segawa, and Y. Ando, *Phys. Rev. B* **82**, 241306 (2010).
- [117] B. Datta, P. C. Adak, L.-k. Shi, K. Watanabe, T. Taniguchi, J. C. W. Song, and M. M. Deshmukh, *Sci, Adv.* **5**, eaax6550 (2019).
- [118] K.-W. Chen, X. Lian, Y. Lai, N. Aryal, Y.-C. Chiu, W. Lan, D. Graf, E. Manousakis, R. E. Baumbach, and L. Balicas, *Phys. Rev. Lett.* **120**, 206401 (2018).
- [119] G. P. Mikitik and Y. V. Sharlai, *Phys. Rev. B* **85**, 033301 (2012).
- [120] C. M. Wang, H.-Z. Lu, and S.-Q. Shen, *Phys. Rev. Lett.* **117**, 077201 (2016).
- [121] L. Balicas, in *Aps march meeting abstracts*, Vol. 2019 (2019), H04–004.
- [122] C. Y. Guo, F. Wu, Z. Z. Wu, M. Smidman, C. Cao, A. Bostwick, C. Jozwiak, E. Rotenberg, Y. Liu, F. Steglich, and H. Q. Yuan, *Nat. Commun.* **9**, 4622 (2018).
- [123] R. Schönemann, N. Aryal, Q. Zhou, Y.-C. Chiu, K.-W. Chen, T. J. Martin, G. T. McCandless, J. Y. Chan, E. Manousakis, and L. Balicas, *Phys. Rev. B* **96**, 121108 (2017).
- [124] J.-P. Issi, *Aust. J. Phys.* **32**, 585 (1979).
- [125] J. W. McClure and W. J. Spry, *Phys. Rev.* **165**, 809 (1968).
- [126] F. Y. Yang, K. Liu, K. Hong, D. H. Reich, P. C. Searson, and C. L. Chien, *Science* **284**, 1335 (1999).
- [127] Y. Kopelevich, J. H. S. Torres, R. R. da Silva, F. Mrowka, H. Kempa, and P. Esquinazi, *Phys. Rev. Lett.* **90**, 156402 (2003).
- [128] X. Du, S.-W. Tsai, D. L. Maslov, and A. F. Hebard, *Phys. Rev. Lett.* **94**, 166601 (2005).

- [129] B. Fauqué, B. Vignolle, C. Proust, J.-P. Issi, and K. Behnia, en, *New J. Phys.* **11**, 113012 (2009).
- [130] Y. Zhao, H. Liu, J. Yan, W. An, J. Liu, X. Zhang, H. Wang, Y. Liu, H. Jiang, Q. Li, Y. Wang, X.-Z. Li, D. Mandrus, X. C. Xie, M. Pan, and J. Wang, *Phys. Rev. B* **92**, 041104 (2015).
- [131] E. Mun, H. Ko, G. J. Miller, G. D. Samolyuk, S. L. Bud'ko, and P. C. Canfield, *Phys. Rev. B* **85**, 035135 (2012).
- [132] Y. Wu, L.-L. Wang, E. Mun, D. D. Johnson, D. Mou, L. Huang, Y. Lee, S. L. Bud'ko, P. C. Canfield, and A. Kaminski, en, *Nat. Phys.* **12**, 667 (2016).
- [133] Z. Yuan, H. Lu, Y. Liu, J. Wang, and S. Jia, *Phys. Rev. B* **93**, 184405 (2016).
- [134] C. Shekhar, A. K. Nayak, Y. Sun, M. Schmidt, M. Nicklas, I. Leermakers, U. Zeitler, Y. Skourski, J. Wosnitza, Z. Liu, Y. Chen, W. Schnelle, H. Borrmann, Y. Grin, C. Felser, and B. Yan, *Nat. Phys.* **11**, 645 (2015).
- [135] C.-L. Zhang, Z. Yuan, Q.-D. Jiang, B. Tong, C. Zhang, X. C. Xie, and S. Jia, *Phys. Rev. B* **95**, 085202 (2017).
- [136] Y. Luo, R. D. McDonald, P. F. S. Rosa, B. Scott, N. Wakeham, N. J. Ghimire, E. D. Bauer, J. D. Thompson, and F. Ronning, *Sci. Rep.* **6**, 27294 (2016).
- [137] C. Zhang, C. Guo, H. Lu, X. Zhang, Z. Yuan, Z. Lin, J. Wang, and S. Jia, *Phys. Rev. B* **92**, 041203 (2015).
- [138] A. A. Burkov, *Nat. Mater.* **15**, 1145 (2016).
- [139] Z. Ren, A. A. Taskin, S. Sasaki, K. Segawa, and Y. Ando, *Phys. Rev. B* **82**, 241306 (2010).
- [140] D. J. Kim, S. Thomas, T. Grant, J. Botimer, Z. Fisk, and J. Xia, *Sci. Rep.* **3**, 3150 (2013).
- [141] F. Hulliger and H. R. Ott, *J. Less Common Metals* **55**, 103 (1977).
- [142] I. Shirovani, K. Yamanashi, J. Hayashi, N. Ishimatsu, O. Shimomura, and T. Kikegawa, *Solid State Commun.* **127**, 573 (2003).
- [143] E. M. Krivoy, S. Rahimi, H. P. Nair, R. Salas, S. J. Maddox, D. J. Ironside, Y. Jiang, V. D. Dasika, D. A. Ferrer, G. Kelp, G. Shvets, D. Akinwande, and S. R. Bank, *Appl. Phys. Lett.* **101**, 221908 (2012).
- [144] J. J. Murray and J. B. Taylor, *J. Less Common Metals* **21**, 159 (1970).
- [145] I. L. Spain and R. O. Dillon, *Carbon* **14**, 23 (1976).
- [146] Y. L. Wang, L. R. Thoutam, Z. L. Xiao, J. Hu, S. Das, Z. Q. Mao, J. Wei, R. Divan, A. Luican-Mayer, G. W. Crabtree, and W. K. Kwok, *Phys. Rev. B* **92**, 180402 (2015).

- [147] X. Z. Yan, Y. M. Chen, X. Y. Kuang, and S. K. Xiang, *J. Appl. Phys.* **116**, 083707 (2014).
- [148] J. He, C. Zhang, N. J. Ghimire, T. Liang, C. Jia, J. Jiang, S. Tang, S. Chen, Y. He, S.-K. Mo, C. C. Hwang, M. Hashimoto, D. H. Lu, B. Moritz, T. P. Devereaux, Y. L. Chen, J. F. Mitchell, and Z.-X. Shen, *Phys. Rev. Lett.* **117**, 267201 (2016).
- [149] J. Xu, N. J. Ghimire, J. S. Jiang, Z. L. Xiao, A. S. Botana, Y. L. Wang, Y. Hao, J. E. Pearson, and W. K. Kwok, *Phys. Rev. B* **96**, 075159 (2017).
- [150] A. Hasegawa, *J. Phys. Soc. Jpn.* **54**, 677 (1985).
- [151] N. W. Ashcroft and N. D. Mermin, *Solid State Physics*, 1 edition (Brooks Cole, New York, 1976).
- [152] O. Pavlosiuk, P. Swatek, and P. Wiśniewski, *Sci. Rep.* **6**, 38691 (2016).
- [153] Q.-H. Yu, Y.-Y. Wang, R. Lou, P.-J. Guo, S. Xu, K. Liu, S. Wang, and T.-L. Xia, *Europhys. Lett.* **119**, 17002 (2017).
- [154] O. Pavlosiuk, P. Swatek, D. Kaczorowski, and P. Wiśniewski, *Phys. Rev. B* **97**, 235132 (2018).
- [155] T. J. Nummy, J. A. Waugh, S. P. Parham, Q. Liu, H.-Y. Yang, H. Li, X. Zhou, N. C. Plumb, F. F. Tafti, and D. S. Dessau, *npj Quantum Mater.* **3**, 24 (2018).
- [156] D. Li, Y. Haga, H. Shida, T. Suzuki, and Y. Kwon, *Phys. Rev. B* **54**, 10483 (1996).
- [157] J. J. Song, F. Tang, W. Zhou, Y. Fang, H. L. Yu, Z. D. Han, B. Qian, X. F. Jiang, D. H. Wang, and Y. W. Du, *J. Mater. Chem. C* **6**, 3026 (2018).
- [158] M. A. Ruderman and C. Kittel, *Phys. Rev.* **96**, 99 (1954).
- [159] T. Kasuya, *Prog. Theor. Phys.* **16**, 45 (1956).
- [160] G. Busch and O. Vogt, *Phys. Lett. A* **25**, 449 (1967).
- [161] J. Rossat-Mignod, P. Burlet, J. Villain, H. Bartholin, W. Tcheng-Si, D. Florence, and O. Vogt, *Phys. Rev. B* **16**, 440 (1977).
- [162] J. Rossat-Mignod, P. Burlet, H. Bartholin, O. Vogt, and R. Lagnier, *J. Phys. C* **13**, 6381 (1980).
- [163] T. Tsuchida and Y. Nakamura, *J. Phys. Soc. Jpn.* **22**, 942 (1967).
- [164] J. Rossat-Mignod, P. Burlet, S. Quezel, J. Effantin, D. Delacôte, H. Bartholin, O. Vogt, and D. Ravot, *J. Magn. Magn. Mater.* **31**, 398 (1983).
- [165] G. Busch, O. Marincek, A. Menth, and O. Vogt, *Phys. Lett.* **14**, 262 (1965).
- [166] D. Li, Y. Haga, H. Shida, T. Suzuki, Y. Kwon, and G. Kido, *J. Phys.: Condens. Matter* **9**, 10777 (1997).
- [167] F. Hulliger, H. R. Ott, and T. Siegrist, *J. Less Common Metals* **96**, 263 (1984).

- [168] A. Fente, H. Suderow, S. Vieira, N. M. Nemes, M. Garcia-Hernández, S. L. Bud'ko, and P. C. Canfield, *Solid State Commun.* **171**, 59 (2013).
- [169] P. Fischer, W. Hälg, and F. Hulliger, *Physica B+C* **130**, 551 (1985).
- [170] W. Witczak-Krempa, G. Chen, Y. B. Kim, and L. Balents, *Annu. Rev. Condens. Matter Phys.* **5**, 57 (2014).
- [171] K. Ueda, R. Kaneko, H. Ishizuka, J. Fujioka, N. Nagaosa, and Y. Tokura, *Nat. Commun.* **9**, 3032 (2018).
- [172] K. Manna, Y. Sun, L. Muechler, J. Kübler, and C. Felser, *Nat. Rev. Mater.* **3**, 244 (2018).
- [173] T. Suzuki, R. Chisnell, A. Devarakonda, Y.-T. Liu, W. Feng, D. Xiao, J. W. Lynn, and J. Checkelsky, *Nat. Phys.* **12**, 1119 (2016).
- [174] B. Meng, H. Wu, Y. Qiu, C. Wang, Y. Liu, Z. Xia, S. Yuan, H. Chang, and Z. Tian, *APL Mater.* **7**, 051110 (2019).
- [175] P. Puphal, C. Mielke, N. Kumar, Y. Soh, T. Shang, M. Medarde, J. S. White, and E. Pomjakushina, *Phys. Rev. Materials* **3**, 024204 (2019).
- [176] G. Kresse and J. Furthmüller, *Phys. Rev. B* **54**, 11169 (1996).
- [177] G. Kresse and D. Joubert, *Phys. Rev. B* **59**, 1758 (1999).
- [178] N. Marzari and D. Vanderbilt, *Phys. Rev. B* **56**, 12847 (1997).
- [179] B. Q. Lv, H. M. Weng, B. B. Fu, X. P. Wang, H. Miao, J. Ma, P. Richard, X. C. Huang, L. X. Zhao, G. F. Chen, Z. Fang, X. Dai, T. Qian, and H. Ding, *Phys. Rev. X* **5**, 031013 (2015).
- [180] L. X. Yang, Z. K. Liu, Y. Sun, H. Peng, H. F. Yang, T. Zhang, B. Zhou, Y. Zhang, Y. F. Guo, M. Rahn, D. Prabhakaran, Z. Hussain, S.-K. Mo, C. Felser, B. Yan, and Y. L. Chen, *Nat. Phys.* **11**, 728 (2015).
- [181] S.-Y. Xu, N. Alidoust, G. Chang, H. Lu, B. Singh, I. Belopolski, D. S. Sanchez, X. Zhang, G. Bian, H. Zheng, M.-A. Hsuanu, Y. Bian, S.-M. Huang, C.-H. Hsu, T.-R. Chang, H.-T. Jeng, A. Bansil, T. Neupert, V. N. Strocov, H. Lin, S. Jia, and M. Z. Hasan, *Sci, Adv.* **3**, e1603266 (2017).
- [182] T. Suzuki, L. Savary, J.-P. Liu, J. W. Lynn, L. Balents, and J. G. Checkelsky, *Science* **365**, 377 (2019).
- [183] L. Ye, Y. Tian, X. Jin, and D. Xiao, *Phys. Rev. B* **85**, 220403 (2012).
- [184] A. Bansil, H. Lin, and T. Das, *Rev. Mod. Phys.* **88**, 021004 (2016).
- [185] A. Neubauer, C. Pfleiderer, B. Binz, A. Rosch, R. Ritz, P. G. Niklowitz, and P. Böni, *Phys. Rev. Lett.* **102**, 186602 (2009).
- [186] N. Kanazawa, Y. Onose, T. Arima, D. Okuyama, K. Ohoyama, S. Wakimoto, K. Kakurai, S. Ishiwata, and Y. Tokura, *Phys. Rev. Lett.* **106**, 156603 (2011).
- [187] J. Matsuno, N. Ogawa, K. Yasuda, F. Kagawa, W. Koshihara, N. Nagaosa, Y. Tokura, and M. Kawasaki, *Sci, Adv.* **2**, e1600304 (2016).

- [188] S. Nakatsuji, N. Kiyohara, and T. Higo, *Nature* **527**, 212 (2015).
- [189] A. K. Nayak, J. E. Fischer, Y. Sun, B. Yan, J. Karel, A. C. Komarek, C. Shekhar, N. Kumar, W. Schnelle, J. Kübler, C. Felser, and S. S. P. Parkin, *Sci. Adv.* **2**, e1501870 (2016).
- [190] X. Li, C. Collignon, L. Xu, H. Zuo, A. Cavanna, U. Gennser, D. Maily, B. Fauqué, L. Balents, Z. Zhu, and K. Behnia, *Nat. Commun.* **10**, 3021 (2019).
- [191] D. Destraz, L. Das, S. S. Tsirkin, Y. Xu, T. Neupert, J. Chang, A. Schilling, A. G. Grushin, J. Kohlbrecher, L. Keller, P. Puphal, E. Pomjakushina, and J. S. White, *npj Quantum Mater.* **5**, 5 (2020).
- [192] H. Weng, C. Fang, Z. Fang, B. A. Bernevig, and X. Dai, *Phys. Rev. X* **5**, 011029 (2015).
- [193] Q. Wang, Y. Xu, R. Lou, Z. Liu, M. Li, Y. Huang, D. Shen, H. Weng, S. Wang, and H. Lei, *Nat. Commun.* **9**, 3681 (2018).
- [194] P. C. Canfield, T. Kong, U. S. Kaluarachchi, and N. H. Jo, *Philos. Mag.* **96**, 84 (2016).
- [195] A. J. Schultz, M. R. V. Jørgensen, X. Wang, R. L. Mikkelsen, D. J. Mikkelsen, V. E. Lynch, P. F. Peterson, M. L. Green, and C. M. Hoffmann, *J. Appl. Crystallogr.* **47**, 915 (2014).
- [196] B. H. Toby and R. B. Von Dreele, *J. Appl. Crystallogr.* **46**, 544 (2013).
- [197] B. Lu, J. D. Tran, and D. H. Torchinsky, *Rev. Sci. Instrum.* **90**, 053102 (2019).
- [198] I. Sochnikov, L. Maier, C. A. Watson, J. R. Kirtley, C. Gould, G. Tkachov, E. M. Hankiewicz, C. Brüne, H. Buhmann, L. W. Molenkamp, and K. A. Moler, *Phys. Rev. Lett.* **114**, 066801 (2015).
- [199] P. Puphal, V. Pomjakushin, N. Kanazawa, V. Ukleev, D. J. Gawryluk, J. Ma, M. Naamneh, N. C. Plumb, L. Keller, R. Cubitt, E. Pomjakushina, and J. S. White, *Phys. Rev. Lett.* **124**, 017202 (2020).
- [200] S. Bergfeld and W. Daum, *Phys. Rev. Lett.* **90**, 036801 (2003).
- [201] I. Sochnikov, A. J. Bestwick, J. R. Williams, T. M. Lippman, I. R. Fisher, D. Goldhaber-Gordon, J. R. Kirtley, and K. A. Moler, *Nano Lett.* **13**, 3086 (2013).
- [202] B. W. Gardner, J. C. Wynn, P. G. Björnsson, E. W. J. Straver, K. A. Moler, J. R. Kirtley, and M. B. Ketchen, *Rev. Sci. Instrum.* **72**, 2361 (2001).
- [203] Z. Wang, M. G. Vergniory, S. Kushwaha, M. Hirschberger, E. V. Chulkov, A. Ernst, N. P. Ong, R. J. Cava, and B. A. Bernevig, *Phys. Rev. Lett.* **117**, 236401 (2016).
- [204] K. S. Takahashi, H. Ishizuka, T. Murata, Q. Y. Wang, Y. Tokura, N. Nagaosa, and M. Kawasaki, *Sci. Adv.* **4**, eaar7880 (2018).

- [205] Y. Machida, S. Nakatsuji, Y. Maeno, T. Tayama, T. Sakakibara, and S. Onoda, *Phys. Rev. Lett.* **98**, 057203 (2007).
- [206] L. Balicas, S. Nakatsuji, Y. Machida, and S. Onoda, *Phys. Rev. Lett.* **106**, 217204 (2011).
- [207] K. Ueda, J. Fujioka, Y. Takahashi, T. Suzuki, S. Ishiwata, Y. Taguchi, M. Kawasaki, and Y. Tokura, *Phys. Rev. B* **89**, 075127 (2014).
- [208] S. M. Disseler, S. R. Giblin, C. Dhital, K. C. Lukas, S. D. Wilson, and M. J. Graf, *Phys. Rev. B* **87**, 060403 (2013).
- [209] W. Witczak-Krempa and Y. B. Kim, *Phys. Rev. B* **85**, 045124 (2012).
- [210] K. Ueda, J. Fujioka, Y. Takahashi, T. Suzuki, S. Ishiwata, Y. Taguchi, and Y. Tokura, *Phys. Rev. Lett.* **109**, 136402 (2012).
- [211] Y. Yamaji and M. Imada, *Phys. Rev. X* **4**, 021035 (2014).
- [212] E. Y. Ma, Y.-T. Cui, K. Ueda, S. Tang, K. Chen, N. Tamura, P. M. Wu, J. Fujioka, Y. Tokura, and Z.-X. Shen, *Science* **350**, 538 (2015).
- [213] R. Ilan, A. G. Grushin, and D. I. Pikulin, *Nat. Rev. Phys.* **2**, 29 (2020).
- [214] A. S. Wills, *Physica B: Condensed Matter* **276-278**, 680 (2000).
- [215] M. J. Cooper and R. Nathans, *Acta Crystallographica* **23**, 357 (1967).
- [216] M. Lee, Y. Onose, Y. Tokura, and N. P. Ong, *Phys. Rev. B* **75**, 172403 (2007).